3-2022

Testbed Creation to Study Noise Radar Network Weighting Models and Data Fusion with Radio Tomographic Imaging

Ryan M. Jans

TESTBED CREATION TO STUDY NOISE RADAR NETWORK WEIGHTING MODELS AND DATA FUSION WITH RADIO TOMOGRAPHIC IMAGING

THESIS

Ryan M Jans, 2d Lt, USAF

AFIT-ENG-MS-22-M-035

DEPARTMENT OF THE AIR FORCE
AIR UNIVERSITY

AIR FORCE INSTITUTE OF TECHNOLOGY

Wright-Patterson Air Force Base, Ohio

AFIT-ENG-MS-22-M-035

TESTBED CREATION TO STUDY NOISE RADAR NETWORK WEIGHTING MODELS AND DATA FUSION WITH RADIO TOMOGRAPHIC IMAGING

THESIS

Presented to the Faculty

Department of Electrical and Computer Engineering

Graduate School of Engineering and Management

Air Force Institute of Technology

Air University

Air Education and Training Command

in Partial Fulfillment of the Requirements for the

Degree of Master of Science in Electrical Engineering

Ryan M Jans, B.S.E.E.

2d Lt, USAF

March 24, 2022

AFIT-ENG-MS-22-M-035

TESTBED CREATION TO STUDY NOISE RADAR NETWORK WEIGHTING MODELS AND DATA FUSION WITH RADIO TOMOGRAPHIC IMAGING

THESIS

Ryan M Jans, B.S.E.E.
2d Lt, USAF

Committee Membership:

Richard K. Martin, Ph.D
Chair

Julie A. Jackson, Ph.D
Member

Robert F. Mills, Ph.D
Member

AFIT-ENG-MS-22-M-035

Abstract

Significant research has been conducted on Radio Tomographic Imaging (RTI) weighting models; however, very little comparative research has been conducted for Noise Radar Network (NRN) weighting methods. In order to create comparative weighting methods for NRN, it is necessary to create a testbed which allows for RTI and NRN research to be conducted simultaneously and allow for data fusion methods to also be researched. After creating the testbed and analyzing results, the newly proposed weighting method provides an up to 33% performance increase in target localization accuracy when compared to the previous weighting model used for NRN. The attenuation image resolution improvements resulted in a 79% performance increase in target localization accuracy for the MAP estimate. In addition to the performance increase, the newly proposed weighting method has the capability to provide a foundation for future research into NRN weighting methods. The testbed created allows for seamless interchanging of data sets, weighting models, and experimental conditions.

Acknowledgements

This thesis was made possible by the help and support of many individuals. I would like to thank my advisor, Dr. Richard Martin, for his support and guidance throughout this process. His feedback and expertise provided a great foundation for me to build from. I would also like to thank my wife for her continuous love and support. Finally, I would like to thank my parents for instilling the desire to challenge myself every day.

Ryan M Jans

Table of Contents

Page

List of Figures

Figure Page

List of Tables

TESTBED CREATION TO STUDY NOISE RADAR NETWORK WEIGHTING MODELS AND DATA FUSION WITH RADIO TOMOGRAPHIC IMAGING

I. Introduction

This chapter provides relevant background information on the topics this thesis addresses to resolve. Specific research objectives which this thesis is aimed at accomplishing are also outlined in this chapter. This chapter is concluded with an overview of the document.

1.1 Problem Statement

Radio Tomographic Imaging (RTI) research has seen significant research advancements in weighting models and reconstruction methods. Equivalent research for Noise Radar Network (NRN) has not been conducted to the same degree, and currently there is only a single weighting method for NRN [1]. In order to conduct equivalent research, it will be necessary to setup a testbed which can study both RTI and NRN. A prior research approach has applied algorithms and models to RTI and NRN individually, but it required a separate testbed for each separate model and algorithm selected in order to process data from input to image reconstruction [1]. RTI system research primarily focuses on techniques and algorithms for image weighting and reconstruction, which could be extended to NRN [1, 2, 3]. Data fusion between RTI and NRN has been conducted but only at a functional level. Currently there is not a testbed which allows for various types of data to be inputted with ability to select desired models and algorithms from input to output to quickly compare approaches. Additionally, without a centralized testbed it is difficult to gather accurate

performance metrics for the desired models and algorithms with ease.

1.2 Research Objectives

Prior research approaches have applied algorithms and models to NRN and RTI but have required separate testbed simulations to process data from input to image reconstruction. The separate testbeds are often rigid and situationally dependent on desired data inputs. There is currently no universal testbed which allows for accurate model and algorithm comparison between disparate data from RTI and NRN. Additionally, extensive research into methods of reconstruction of RTI data into images has been conducted [2, 3, 4]. NRN image reconstruction is focused primarily on back projection; however, RTI reconstruction method concepts have the potential to be translated from RTI to NRN [1]. Therefore, the research objectives of this thesis will be to create a universal testbed which allows for streamlined analysis of RTI and NRN images from data input to target detection, and through the new testbed, determine new ways of NRN weighting methods. Analysis of the data fusion between RTI and NRN, both in image and data format, will be conducted to determine feasibility of disparate data types for additional accuracy in device-free localization (DFL).

Analysis will be conducted qualitatively and quantitatively. The testbed is primarily utilized for data processing since in most cases data will have been previously collected. The data for RTI and NRN is collected from the respective sensing systems and loaded into the testbed. The hardware characteristics are inputted and selected within the testbed. The universal testbed will operate in four stages: data input, image reconstruction, target detection, and performance metrics. The performance metric stage will contain four images where targets are detected. The four images will be RTI image, NRN image, fused images of RTI and NRN, and the image as a result of fused data between RTI and NRN. Target localization will be conducted on

the produced attenuation images which were created with various models and algorithms in order to compare legacy methods to new methods. Performance metrics will be utilized to classify the target localization errors present within each method. Research will be successful upon the creation and usage of a testbed which allows for user desired data input, model, and algorithm selection. Upon completion of the testbed, it will be used to create new algorithm comparisons to extend existing RTI approaches to NRN and provide new insight on NRN weighting methods.

1.3 Document Overview

This thesis document contains five chapters. Chapter I discusses the problem overview, research objectives, and an overview of the document. Chapter II discusses the background and literature review conducted on RTI, NRN, and data fusion methods. Chapter III discusses the methodology which is used to to execute the research objectives. Chapter IV discusses the results and analysis from the methodology. Chapter V discusses final performance results from the testbed and the new weighting methods for NRN as well as future work.

II. Background and Literature Review

This chapter provides background and current literature pertaining to previous work on Radio Tomographic Imaging (RTI) and Noise Radar Network (NRN). Fundamental theory on how each of these systems operate, models used, and methods of image reconstruction are included. This chapter also provides relevant information on current data fusion techniques relevant to RTI and NRN.

2.1 Radio Tomographic Imaging

RTI systems utilize radio shadowing to detect targets within a desired area through device-free localization (DFL). DFL is achieved in RTI by using a Wireless Sensor Network (WSN) which creates node links from each wireless sensor that do not require sensors on the target or that the target position is previously known. While user-attached devices can improve target localization, this adds an increased level of complexity [5]. The WSN is created using radio frequency (RF) transceivers which network with each other to create a network of node links that attenuate based on physical objects within the target area. Received signal strength (RSS) measurements from each node link are collected and images are reconstructed based on attenuation of the physical objects. Common commercial solutions can be utilized to track personnel and items in warehouse, as well as industrial facilities [6]. Target detection can occur in a wide variety of scenarios and environments, such as through walls, foliage, roadside surveillance, and in low visibility conditions [6, 7, 8]. As such, applications for RTI systems range from security to studying behavior of individuals with post-traumatic stress disorder (PTSD). A key benefit of using an RTI system for this is that no wearable devices are required to sense targets or individuals within the desired environment.

2.1.1 Theory

The WSN can be modified to fit the user's requirements and capabilities, with regards to number of RF transceivers and the geometric configuration which is utilized. The number of RF transceivers affects the number of two-way links,

$$M = \frac{n^2 - n}{2} \tag{1}$$

where n is the total nodes and M is the number of unique two-way links. In a symmetric and equal node spacing configuration, the increase in nodes provides an increase in coverage of the node links across the detection area. The nodes in the WSN communicate via a token passing protocol. Each node transmits a signal to the base station as well as to all of the other nodes [2, 9, 10, 11]. This allows the RSS measurements to be recorded. After the first node transmits a signal, the token is passed to the next sequential node. If the next sequential node does not transmit within the allotted time, the base station passes the token to the next node and the process continues until all of the nodes have had the opportunity to transmit [2, 9, 10, 11].

Figure 2.1 shows a wireless sensor network with its respective nodes and links. RTI systems utilize RSS to determine which node links have been affected by the target. Targets within the WSN absorb, reflect, diffract, or scatter a portion of the transmitted signal power and the signal becomes shadowed. The shadowing results in a reduction of signal amplitude at the respective node link receiver. Each node link covers N pixels of the network region, allowing for the weighting of each to result in an image which contains potential target locations [7, 12]. The equation for RSS determination is

$$y_i(t) = P_i - L_i - S_i(t) - F_i(t) - v_i(t) \tag{2}$$

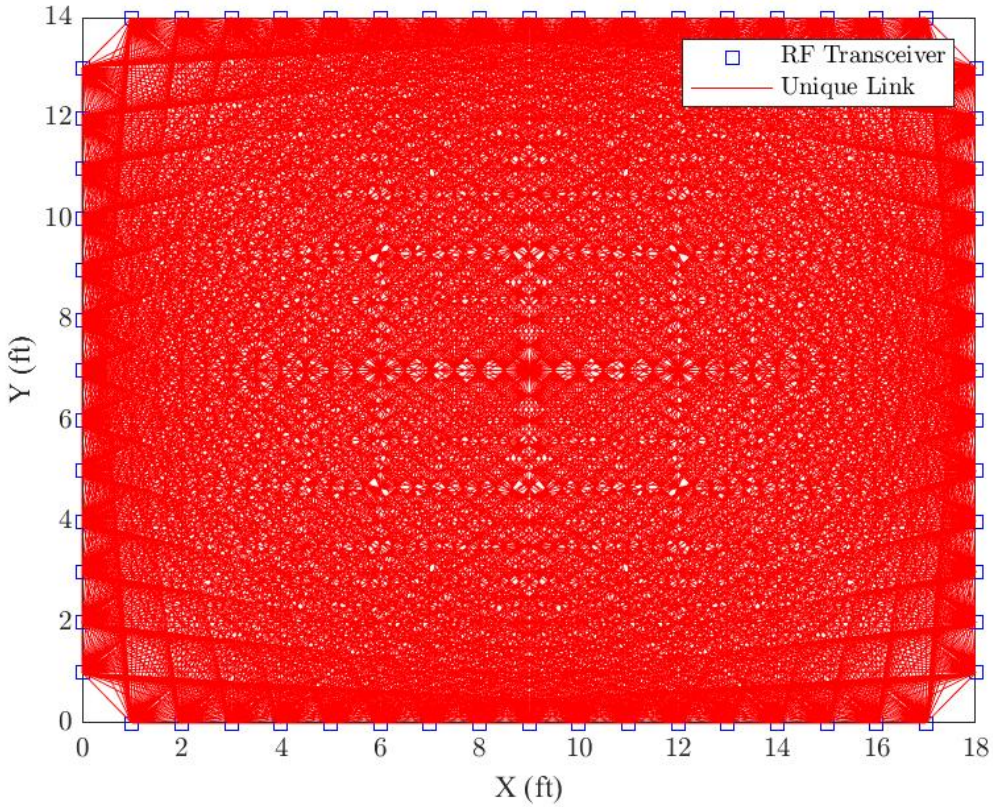

Figure 2.1: Wireless sensor network.

at a node where $y_i(t)$ is the received signal, P_i is the transmitted power, L_i are static losses in decibels (dB), $S_i(t)$ is the shadowing loss in dB due to target attenuation, $F_i(t)$ is fading loss due to multipath environment, and $v_i(t)$ is the measurement noise.

All of the above variables are measured in decibels [7]. Shadowing loss variable $S_i(t)$ is approximately equal to the sum of attenuation in each pixel along a link. For each link, the pixels affect the amount of attenuation differently and therefore a weighting is applied. For a specific link, the shadowing loss is represented by

$$S_i(t) = \sum_{j=1}^{N} w_{ij} x_j(t) \tag{3}$$

where w_{ij} is the weight of pixel j on link i and $x_j(t)$ is the attenuation in pixel j at

time t [7].

Calibration is required to prevent a mismatch between the model and the measurements [13]. The calibration is performed at time t to create a baseline of RSS measurements where no targets are present so that the change in RSS, Δy_i, can be determined. The calibration step is performed by first recording the RSS measurements when there are no targets obstructing the links in the WSN [14]. The calibration RSS measurements $y_i(t_c)$ are then subtracted from the RSS measurements recorded when there are targets obstructing the links $y_i(t)$ [4, 7, 15]. Under the assumption that static losses become negligible over time, the change in RSS is

$$\begin{aligned} \Delta y_i &= y_i(t) - y_i(t_c) \\ &= S_i(t) - S_i(t_c) + F_i(t) - F_i(t_c) + v_i(t) - v_i(t_c). \end{aligned} \tag{4}$$

The fading loss $F_i(t)$ and measurement noise $v_i(t)$ can be combined into the noise term n_i given by [7]

$$n_i = F_i(t) - F_i(t_c) + v_i(t) - v_i(t_c). \tag{5}$$

Equation (3) and Equation (5) can then be substituted into Equation (4) to generate the change in RSS,

$$\Delta y_i = \sum_{j=1}^{N} w_{ij} \Delta x_j + n_i \tag{6}$$

where Δx_j is the change in attenuation for pixel j from times t_c to t [7]. When all of the links are considered at once, Equation (6) can be written in matrix form as

$$\Delta \mathbf{y} = \mathbf{W} \Delta \mathbf{x} + \mathbf{n} \tag{7}$$

where $\Delta \mathbf{y}$ is the length M change in RSS vector, $\mathbf{W}$ is the $M \times N$ weight matrix whose rows contain the weights of the pixels for the node links and whose columns represent

the individual pixels, $\Delta\mathbf{x}$ is the length N attenuation image vector to be estimated, and $\mathbf{n}$ is the length M noise vector [7]. To shorten the notation in Equation (7), the terms $\mathbf{x}$ and $\mathbf{y}$ will replace $\Delta\mathbf{x}$ and $\Delta\mathbf{y}$.

According to [7], the noise vector in Equation (7) is attributed to RSS time variation when no targets are obstructing the LOS paths. In the absence of any target, the RSS measurements should be constant over time, but this is not the case due to residual noise in the system. Also, multipath interference contributes to the noise in the RTI system because it affects the NLOS paths [16].

Wilson and Patwari [7] collected experimental noise samples by implementing the RTI system and recording the RSS measurements of links when no targets were present in the environment. For a given link, the results showed periods of heavy fading and low fading which corresponded to a combination of high variance and low variance Gaussian distributions. The mean data from each link was extracted and fitted with a Gaussian mixture distribution that provided a sufficient approximation [7]. Most commonly in RTI research, the noise is modeled as a zero-mean Gaussian distribution known as additive white Gaussian noise (AWGN) [3, 16, 17, 18]. The AWGN model and Gaussian mixture model both fit the data in a similar fashion [7].

2.1.2 Models

RTI models determine how an RTI system reacts to changes within the sensing area based on RSS measurements collected. Within the RSS measurements, multipath components are present that degrade system performance, such as electronic noise, reflection, refraction, and shadowing [2]. Models are intended to characterize RSS attenuation and multipath interference in order to produce attenuation images that contain the least amount of artifacts [2, 4]. RTI models are useful when there is prior knowledge of the environment or if the environment can be estimated [7].

2.1.2.1 Network Shadowing Model

Wilson and Patwari introduced the network shadowing (NeSh) model as part of the RTI method for model-based DFL [19, 20]. The weight matrix $\mathbf{W}$ is used in the NeSh model to determine the pixel weights necessary to calculate the change in RSS $\mathbf{y}$. According to [3], the weight matrix can be represented as

$$\mathbf{W} = \mathbf{S} \odot \mathbf{\Omega} \tag{8}$$

where $\mathbf{S}$ is the binary selection matrix, $\mathbf{\Omega}$ is a matrix that contains the real-valued weight magnitudes, and $\odot$ signifies element-wise multiplication.

The NeSh model utilizes an ellipse with foci at each node to determine the weighting of each pixel for a particular link [7]. The pixel weight is calculated by

$$w_{ij} = \frac{1}{\sqrt{d_i}} \begin{cases} 1, & \text{if } d_{ij}(1) + d_{ij}(2) < d_i + \lambda \\ 0, & \text{otherwise} \end{cases} \tag{9}$$

where d_i is the distance between the two nodes that make up link i, $d_{ij}(1)$ is the first node and $d_{ij}(2)$ is the second node and they are the distances from the center of pixel j to the nodes of link i, and λ is the width of the ellipse [3, 7]. The width of the ellipse is generally set low to simulate the LOS path; however, it is ultimately tuned based on user specification [7].

Figure 2.2 demonstrates the weighting conducted for a single weighted link for the NeSh model. The high intensity pixels of the weighting image would lead to the data within those image pixels being weighted as one while the low intensity pixels result in a zero weighting. The length of the node link has an impact on the change in RSS. Longer links that are obstructed by targets have less change in RSS because the signals have a longer distance to travel and can reflect around the targets, whereas the

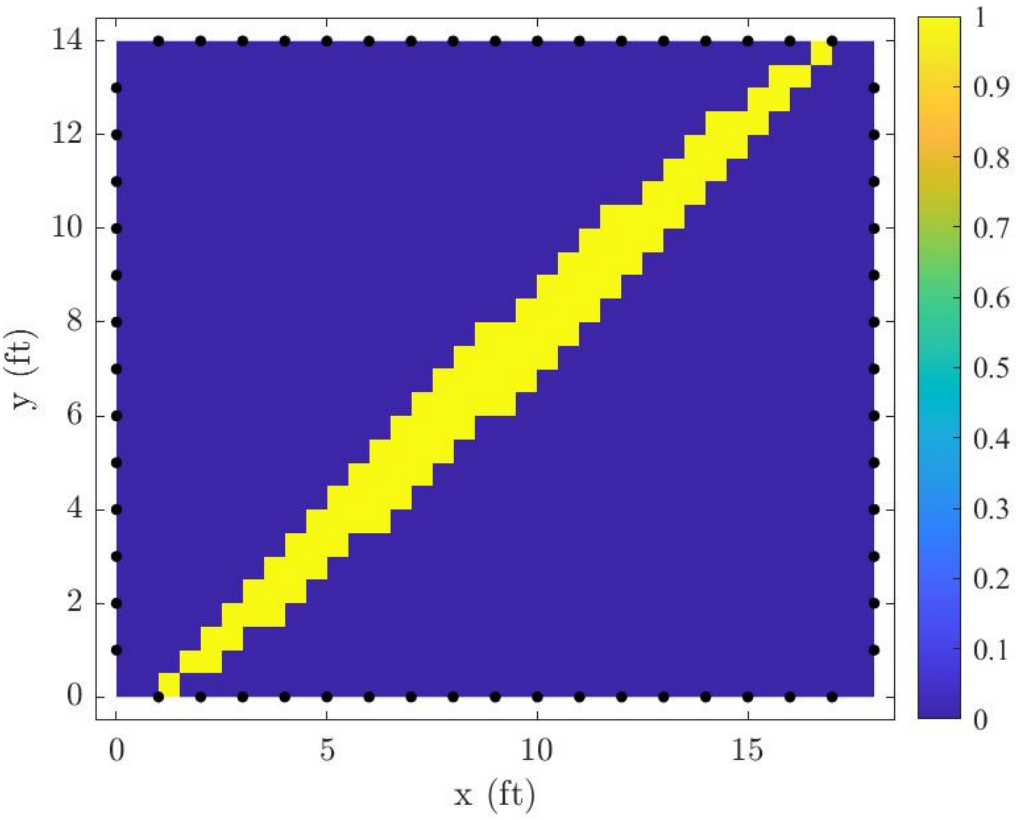

Figure 2.2: Single weighted link NeSh model from node at (1,0) to node at (17,14).

shorter obstructed links exhibit substantial change in RSS due to the abrupt target interference [7]. Equation (9) demonstrates the weights of the pixels that fall within the ellipse are equal to the inverse square root of the distance of link i. This holds with the change in RSS being inversely proportional to the length of the node link [15]. Although the NeSh model considers the length of the links, it does not consider the distance between the targets and links. The model also gives equal weights to all of the pixels that fall within the ellipse, however this is inconsistent with the fact that the targets affect pixel locations differently. Research has shown that targets have a greater influence on nodes when they are located closer to them [20]. The NeSh model is not practical for operational applications [2].

2.1.2.2 Inverse Area Elliptical Model

The goal of the inverse area elliptical model (IAEM) is to relate signal shadowing to attenuation occurring at specific locations in the WSN. Similar to Section 2.1.2.1, an ellipse is utilized with foci at each node to determine the weighting of each pixel for a particular link [3, 7]. IAEM relates signal shadowing to attenuation at specific locations by accounting for the fact that some areas of the ellipse contribute more to the change in RSS than others. To demonstrate the contributions, the weight matrix is set equal to the inverse area of the smallest ellipse contained within a particular link [3, 18]. The area of the ellipse is given by

$$A(d_i, \lambda_{ij}) \approx \frac{\pi}{4} d_i \sqrt{2 d_i \lambda_{ij}} \tag{10}$$

where d_i is the distance between the two nodes that make up link i and λ_{ij} is the width of the ellipse that is either a set tunable parameter or given by

$$\lambda_{ij} = d_{ij}(1) + d_{ij}(2) - d_i \tag{11}$$

where $d_{ij}(1)$ and $d_{ij}(2)$ are the distances from the center of pixel j to the nodes of link i [3]. Equations (10) and (11) are used to calculate the IAEM given by

$$\mathbf{W} = \begin{cases} A^{-1}(d_i, \lambda_{min}), & \text{if } \lambda_{ij} < \lambda_{min} \\ A^{-1}(d_i, \lambda_{ij}), & \text{if } \lambda_{ij} \geq \lambda_{min} \end{cases} \tag{12}$$

where λ_{min} is a tunable parameter [3]. The weights are bounded by the semi-minor axis lengths determined by λ_{min} and λ_{ij} [18].

Figure 2.3 shows a single weighted link for the IAEM. The IAEM utilizes the ellipse because the Fresnel zone is known to have an ellipsoidal shape [2, 18]. Although the

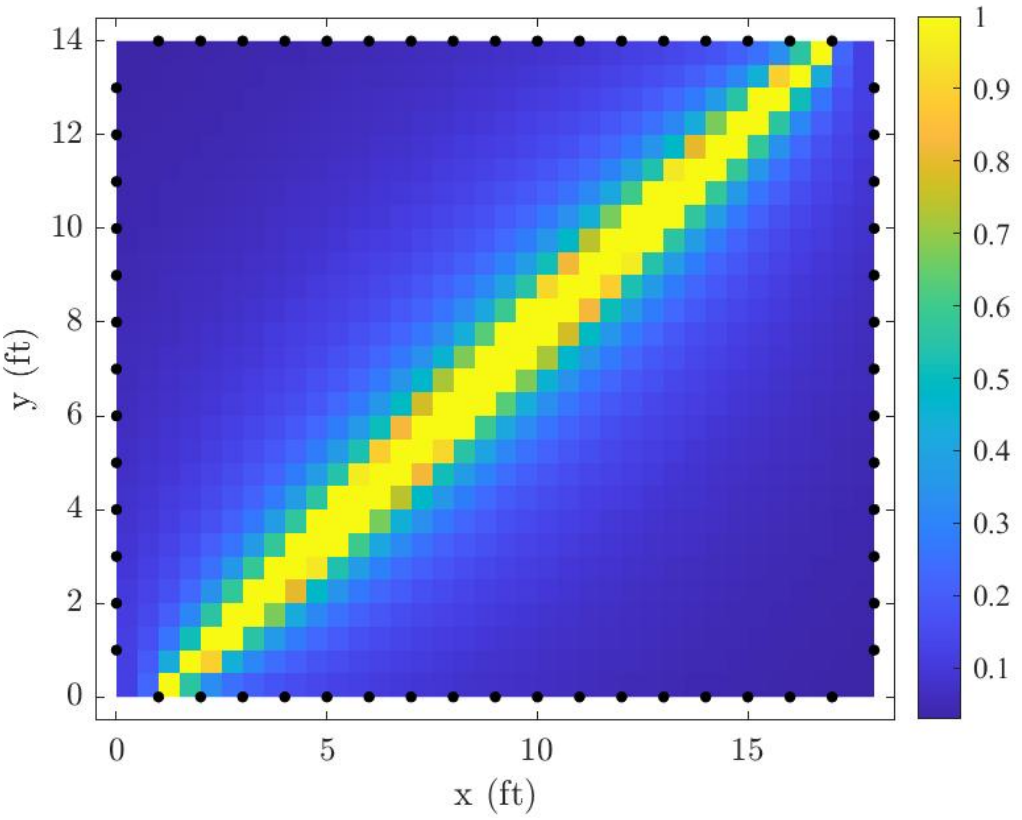

Figure 2.3: Single IAEM weighted link from node at (1,0) to node at (17,14).

NeSh model also utilizes the ellipse, the IAEM considers the fact that the change in RSS is different for signals that travel close to the edge of the ellipse as opposed to those traveling near the LOS path. The signals traveling along the edge of the ellipse have a farther distance to travel and therefore have less impact on change in RSS. For this reason, the IAEM weights pixels farther from the LOS path less than that those closer to the LOS path [2, 18]. This is a substantial improvement, however the contributions of the individual pixels within an ellipse cannot be distinguished [15, 20].

2.1.2.3 Exponential-Rayleigh Model

The Exponential-Rayleigh (ER) model characterizes the change in RSS while also addressing multipath interference which degrades DFL accuracy. The ER model consists of a large-scale exponential component that represents the link shadowing and a Rayleigh component that represents the multipath interference introduced by targets obstructing the links [17]. The ER attenuation model for a single target is

$$y_i(\mathbf{k}) = \beta_a e^{\frac{-\lambda_i(\mathbf{k})}{\sigma_a}} - \beta_b \lambda_i(\mathbf{k}) e^{\frac{-\lambda_i^2(\mathbf{k})}{\sigma_b}} \tag{13}$$

where i is the particular link, $\mathbf{k}$ is the state, β_a and σ_a are the attenuation parameters, β_b and σ_b are the model parameters, and λ_i is the excess path length which is the difference between the major axis length of the ellipse and the intra-focal distance as in Equation (11) [3, 17]. The pixel intensities greater than zero indicate target-induced attenuation and the pixel intensities less than zero imply RSS enhancement [17, 3]. For multiple targets, the ER attenuation model is expressed by

$$y_i(\mathbf{K}) = \sum_{g=1}^{G} y_i(\mathbf{k}_g) \tag{14}$$

where G is the total number of targets and $y_i(\mathbf{k}, g)$ is the ER component of target g [17].

Figure 2.4 shows a single weighted link for the ER weighting method. For Equation (14), the expectation maximization (EM) algorithm is used to determine the attenuation parameters (β_a and σ_a) and the model parameters (β_b and σ_b). Although the ER model enhances the multipath components to account for their effect on the change in RSS, this requires the use of the EM algorithm which adds computational complexity [17]. Conversely, the NeSh model and IAEM more simply rely on the weight matrix calculations to characterize the changes in attenuation [2].

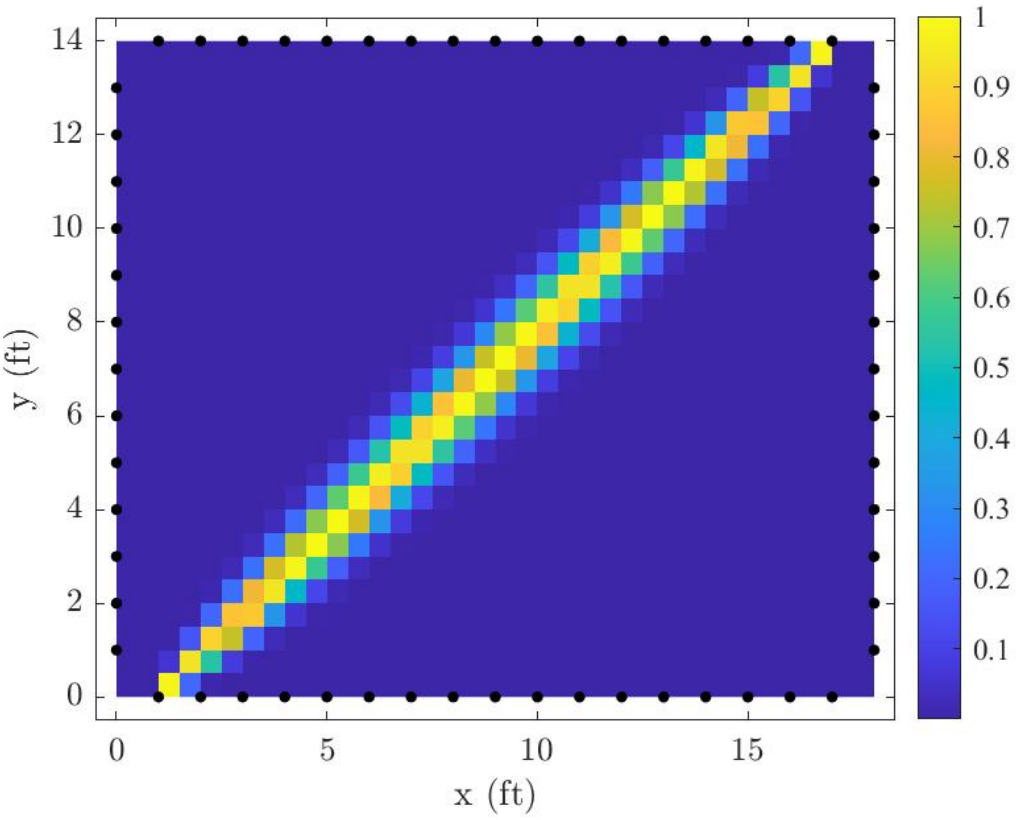

Figure 2.4: Single weighted link ER model from node at (1,0) to node at (17,14).

The ER model is not used to create images of the attenuation. Equation (13) and Equation (14) are used in conjunction with particle filtering to estimate the target location vector k [17].

2.1.2.4 Weighting-g Model

The weighting-g model is an elliptical model that determines the weight matrix based on the distance of the pixels in the ellipse and their proximity to the LOS path [15]. The model introduces a distance attenuation factor that improves target

localization performance. The weighting-g model is represented by

$$w_{ij} = \begin{cases} e^{-h}, & \text{if } d_{ij}(1)+d_{ij}(2) < d_i + \lambda \\ 0, & \text{otherwise} \end{cases} \tag{15}$$

where h is the distance between pixel j inside the ellipse and LOS path i, $d_{ij}(1)$ and $d_{ij}(2)$ are the distances from the center of pixel j to the nodes of link i, d_i is the distance between the two nodes that make up link i, and λ is the tunable width of the ellipse [15].

Figure 2.5 shows a single weighted link for the weighting-g model. The signal

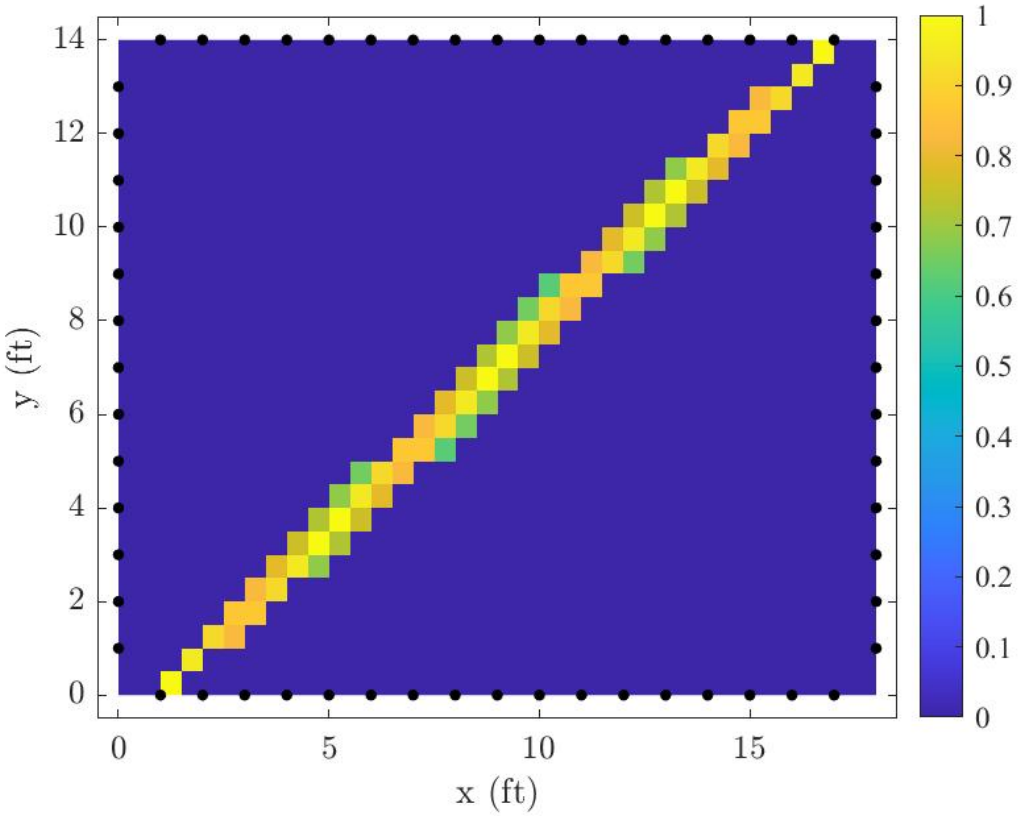

Figure 2.5: Single weighted link weighting-g model from node at (1,0) to node at (17,14).

shadowing along LOS paths is greater than the shadowing along NLOS paths [15]. The weighting-g model addresses this difference in shadowing by assigning different weights to the pixels within the ellipse that reside along the LOS path or NLOS path. In Equation (15), pixels that fall within the ellipse are given a magnitude equal to the distance attenuation factor e^{-h}. The factor ensures the pixels that contain the LOS paths have greater weights than the pixels that contain the NLOS paths. This is consistent with the shadowing behavior that occurs in a real world environment [2, 15].

The weighting-g model differs from the previously described RTI models. Unlike the NeSh model, the weighting-g model considers the distance relationship between the pixels and LOS path and attributes different weights to the pixels. This is done to provide a closer analogy to the shadowing found in RTI networks. The IAEM model demonstrates actual shadowing behavior; however, the individual pixels are not all uniquely distinguished [2, 15]. The weighting-g model reduces multipath interference by utilizing the distance attenuation factor to condense the number of pixels that have significant attenuation and reduce the appearance of pseudo targets in the attenuation image [2, 15]. The ER model also addresses multipath interference, but it is more computationally complex because it implements the EM algorithm [2, 17].

2.1.3 Reconstruction

RTI reconstruction methods are responsible for generating the estimated attenuation images used to approximate the locations of targets in the WSN environment. These methods rely on the change in RSS data characterized by the RTI models in section Section 2.1.2 [4]. RTI reconstruction is an ill-posed inverse problem meaning that a small amount of noise can be substantially amplified [2]. This noise amplification can then degrade the attenuation image quality and render inaccurate target

localization. For these reasons, the reconstruction methods must account for the presence of noise which introduces artifacts into the attenuation images [2, 4].

2.1.3.1 Tikhonov Regularization

To implement Tikhonov regularization, a derivative energy term is added to the least squares solution. The least squares solution minimizes the fit error in Equation (7) by manipulating the least-squared error given by

$$\mathbf{x}_{LS} = \arg\min_{x} ||\mathbf{W}\mathbf{x} - \mathbf{y}||^2 \tag{16}$$

where $\mathbf{W}$ is the length $M \times N$ weight matrix, $\mathbf{x}$ is the length N attenuation image vector, and $\mathbf{y}$ is the length M change in RSS vector [7]. The least squares solution takes the gradient of Equation (16) and sets it equal to zero to yield

$$\mathbf{x}_{LS} = (\mathbf{W}^T\mathbf{W})^{-1}\mathbf{W}^T\mathbf{y}. \tag{17}$$

This solution is only valid if $\mathbf{W}$ is full rank, and this is not true in RTI systems due to the ill-posed inverse problem. Therefore, regularization is used to introduce information into the model that will tackle the ill-posed issue [2, 7, 21].

Tikhonov regularization is represented by

$$f(x) = \frac{1}{2}||\mathbf{W}\mathbf{x} - \mathbf{y}||^2 + \alpha||\mathbf{Q}\mathbf{x}||^2 \tag{18}$$

where α is an adjustable regularization parameter and $\mathbf{Q}$ is the Tikhonov matrix that approximates the derivative operator [7]. By substituting in the difference matrices

for $\mathbf{Q}$, Equation (18) becomes

$$f(x) = \frac{1}{2}||\mathbf{W}\mathbf{x} - \mathbf{y}||^2 + \alpha(||\mathbf{D}_x\mathbf{x}||^2 + ||\mathbf{D}_y\mathbf{y}||^2) \tag{19}$$

where $\mathbf{D}_x$ and $\mathbf{D}_y$ are the difference operators in the horizontal and vertical directions respectively [7]. After taking the gradient of Equation (19) and setting it equal to zero, the estimated attenuation becomes

$$\hat{\mathbf{x}} = (\mathbf{W}^T\mathbf{W} + \alpha(\mathbf{D}_x^T\mathbf{D}_x + \mathbf{D}_y^T\mathbf{D}_y))^{-1}\mathbf{W}^T\mathbf{y}. \tag{20}$$

The estimated attenuation can now be represented as a linear transformation of the change in RSS data given by

$$\hat{\mathbf{x}} = \Pi\mathbf{y} \tag{21}$$

where Π is given by

$$\Pi = (\mathbf{W}^T\mathbf{W} + \alpha(\mathbf{D}_x^T\mathbf{D}_x + \mathbf{D}_y^T\mathbf{D}_y))^{-1}\mathbf{W}^T. \tag{22}$$

The computational simplicity of the linear transformation is one of the main benefits of Tikhonov regularization. Also, the linear transformation allows for faster reconstruction because it does not rely on instantaneous measurements and Π can be precalculated [2, 7, 21]. Tikhonov regularization successfully minimizes noise energy and generates smooth attenuation images; however, some of the target-induced attenuation may be eliminated throughout the process [2, 4].

2.1.3.2 Low-Rank and Sparse Decomposition

Low-rank and sparse decomposition (LRSD) separates the environmental background image from the target-induced foreground image to improve attenuation im-

age quality and target localization accuracy [2, 4]. The image artifacts are reduced by restricting the background environment using a low-rank condition. After constraining the background, the sparse target-induced foreground is enhanced [2, 4]. The sparsity algorithm is then used to obtain a solution for $\mathbf{x}$.

The attenuation image $\mathbf{x}$ can be represented as the combination of the environmental background image $\mathbf{l}$ and the target-induced foreground image $\mathbf{s}$ [4, 22]. The combination is given by

$$\mathbf{x} = \mathbf{l} + \mathbf{s}. \tag{23}$$

Equation (23) can also be expressed in matrix form by reshaping the $\mathbf{l}$ and $\mathbf{s}$ vectors so they have the same dimensions as the true image. The matrix form is given by

$$\mathbf{X} = \mathbf{L} + \mathbf{S}. \tag{24}$$

In other sparisty-regularized methods such as BCS and HBCS, the imaging artifacts caused by multipath interference may be mistaken as the target-induced attenuation [2, 4]. To mitigate this mistake, the LRSD method uses a sufficient constraint to suppress the artifacts in $\mathbf{L}$. LRSD then implements a sparsity-regularized algorithm to recognize the target-induced attenuation in $\mathbf{S}$ [2, 4].

The LRSD optimization problem is used to solve for the attenuation image. The optimization problem is given by

$$\mathbf{x} = \arg \min_{l,s} ||\mathbf{y} - \mathbf{W}(\mathbf{l} + \mathbf{s})||_2^2 + ||\mathbf{L}||_* + \alpha||\mathbf{S}||_1 \tag{25}$$

where $\mathbf{y}$ is the change in RSS vector, $\mathbf{W}$ is the weight matrix, $||\mathbf{L}||_* = \Sigma_i \sigma_i(\mathbf{L})$ is the nuclear norm for the minimized rank, $\sigma_i(\mathbf{L})$ is the i^{th} singular value of $\mathbf{L}$, and α is the regularization constant [4]. The background image vector $\mathbf{l}$ is solved for by using

partial singular value decomposition (SVD) by

$$\begin{aligned}[\mathbf{U}^{[c]}, \mathbf{\Sigma}^{[c]}, \mathbf{V}^{[c]}] &= \text{SVD}(\mathbf{Y}^* - \mathbf{S}^{[c]}) \\ \hat{\mathbf{L}}^{[c+1]} &= \mathbf{U}^{[c]}_{:,1:r}\ \mathbf{\Sigma}^{[c]}_{1:r,1:r}\ \mathbf{V}^{[c]T}_{:,1:r} \\ \hat{\mathbf{l}}^{[c+1]} &= \text{Vec}(\hat{\mathbf{L}}^{[c]})\end{aligned} \tag{26}$$

where c is the iteration count, r is the rank constraint, $\mathbf{U}$ is a $M \times M$ matrix whose columns form orthonormal vectors, $\mathbf{V}$ is a $N \times N$ matrix whose columns form orthonormal vectors, $\mathbf{Y}^*$ is the matrix form of the reshaped vector $\mathbf{y}^* = \mathbf{W}^*\mathbf{y}$ according to the notation in [2, 4], $\mathbf{S}$ is the matrix form of the reshaped vector $\mathbf{s}$, $\mathbf{\Sigma}$ is a $M \times N$ matrix whose diagonal entries are the singular values of $(\mathbf{Y}^* - \mathbf{S}^{[c]})$, and Vec is the vectorization of matrix $\mathbf{L}$ [4]. The foreground image $\mathbf{s}$ is estimated by

$$\hat{\mathbf{s}}^{[c+1]} = \arg\min_{s} ||\mathbf{y} - \mathbf{W}(\hat{\mathbf{l}}^{[c+1]} + \mathbf{s})||_2^2 + \alpha||\mathbf{s}||_1. \tag{27}$$

To solve (27), the iterative shrinkage-thresholding algorithms from Beck [2, 23] are used. The foreground image is then given by

$$\hat{\mathbf{s}}^{[c+1]} = \mathbf{S}_{\alpha\tau}\{\hat{\mathbf{s}}^{[c]} - 2\tau[\mathbf{\Psi}(\hat{\mathbf{l}}^{[c+1]} + \hat{\mathbf{s}}^{[c]}) - \mathbf{y}^*]\} \tag{28}$$

where $\mathbf{\Psi} = \mathbf{W}^*\mathbf{W}$, $\boldsymbol{y}^* = \mathbf{W}^*\boldsymbol{y}$ according to the notation in [4], τ is the step size, and $\mathbf{S}_{\alpha\tau}$ is the soft thresholding operator given by

$$\mathbf{S}_{\alpha\tau}(\mathbf{z})_i = \text{sign}(z_i)\max(0, |z_i| - \alpha\tau) \tag{29}$$

where sign is the signum function [4]. After $\hat{\mathbf{l}}$ and $\hat{\mathbf{s}}$ converge, the attenuation image $\hat{\mathbf{x}}$ is obtained by adding $\hat{\mathbf{l}}$ and $\hat{\mathbf{s}}$ [2, 4].

2.1.4 RTI Hardware Considerations

The RTI system referenced in this thesis operates in an Air Force Institute of Technology (AFIT) laboratory. It utilizes 70 nodes which consist of TelosB TPR2400CA transceivers manufactured by MEMSIC. The transceivers communicated using the Spin protocol and operated on the 2.4 GHz band [2, 14]. The RTI network connects to a computer via universal serial bus (USB) in order to collect data and operate the RTI network. The RF transceivers are mounted at a height of 3'4" on polyvinyl chloride (PVC) pipes [2]. The laboratory environment surrounding the RTI network consists of cinder block walls with various desks, computers, and metal storage cabinets.

2.2 Noise Radar Network

Noise Radar Networks utilize an active target detection method. Utilizing radar reflection, target detection occurs when a signal is transmitted, reflected from a target, then received and processed. NRN is unique because the transmission signal is a randomly generated Ultra-wideband (UWB) pseudo-noise signal, intended to be embedded within a noisy environment and returned to the receiver [24]. At the receiver, the transmitted signal is correlated with the return signal to determine the range the target is located at. This active method of target detection can be used in situations where the transmitted signal is known at the receiver and not desired to be known by others.

Key advantages of a NRN system include effective target detection in noisy environment as well as a low detection threshold of the transmitted signal. Transmitted and received signals are effectively disguised as noise, allowing for a degree of security without the use of encryption [25]. The combination of Low Probability of Intercept (LPI) and Low Probability of Exploitation (LPE) makes it very desirable in situations

where covert target detection is desired. The system can be set up with relative ease due to a low number of necessary systems that are required to support it. Disadvantages of the system are that the targets may be lost due to range ambiguities and target shadowing due to interference from other systems operating within the same frequency range and target environment.

NRN operates utilizing radio reflection in a monostatic or bistatic radar configuration. A pseudo-random signal is used as the transmitted waveform. The transmitted signal must be known at the receiver. If the transmitted signal is unknown, it is difficult to accurately determine the proper waveform outside of noise. To an independent observer, the transmitted waveform appears as noise. Once the transmitted signal is received, the transmitted signal is correlated with the return signal to find the time lag. From the time lag, the range will be determined by

$$R = \frac{\Delta T c}{2} \tag{30}$$

where ΔT is the round-trip time and c is the speed of light. The NRN is based on utilizing an UWB waveform, ranging from 500 MHz to 1000 MHz, for NRN signal transmission. The range resolution is determined by

$$\Delta R = \gamma \frac{c}{2B} \tag{31}$$

where c being the speed of light, γ a factor in the range $1 \leq \gamma \leq 2$ that represents degradation in range resolution from system errors and B being the bandwidth of the signal [24]. From 31, the theoretical range resolution of the UWB noise radar ranges from 0.6 meters to 0.3 meters, respectively [24, 26].

NRN characteristics for this thesis are based on the AFIT Noise Network (NoNET) created by Schmitt [27]. Simulation and experimental setups include the usage of

three digital noise radars in a monostatic configuration to triangulate the location of a target within the desired testing area. Triangulation of target location provided optimal target locating ability [27]. Limitations of the AFIT NoNET are primarily contained in the number of noise radars required and the radar resolution they provide. For traditional target detection of a human target, resolution does not prove to be a problem in accurate positioning. Limited research was conducted on error/accuracy analysis outside of stating the sampling frequency is a limitation to range accuracy [24]. Work by Nelms [26] demonstrated the capability of the AFIT NoNET to operate in a multistatic configuration. To use trilateration to create images for a NRN system to be fused with RTI, it is necessary to linearize each NRN radar node into

$$\begin{aligned} \mathbf{y}_{NRz} &= \mathbf{W}_{NRz}\mathbf{x}_{NRz} + \mathbf{n}_{NRz} \\ \mathbf{n}_{NRz} &\sim \mathcal{N}(0, C_{NRz}) \end{aligned} \tag{32}$$

where $\mathbf{x}_{NRz}$ is the $N\times1$ pixelated representation of the true scene occupancy, which can be thought of as a reflection image to be estimated with N pixels from the zth NRN node, $\mathbf{y}_{NRz}$ is the $I\times1$ vector of magnitudes in the impulse response/cross correlation magnitudes at I calibrated ranges from the zth NRN node. $\mathbf{W}_{NRz}$ is the weighting matrix with each column representing a single pixel and each row describing the weighting of each pixel for a particular range, and $\mathbf{n}_{NRz}$ is the noise vector of the zth NRN node [24]. When utilizing the traditional three AFIT NoNET monostatic nodes, the equation becomes

$$\begin{bmatrix} \mathbf{y}_{NR1} \\ \mathbf{y}_{NR2} \\ \mathbf{y}_{NR3} \end{bmatrix} = \begin{bmatrix} \mathbf{W}_{NR1} \\ \mathbf{W}_{NR2} \\ \mathbf{W}_{NR3} \end{bmatrix} \mathbf{x}_{NRN} + \begin{bmatrix} \mathbf{n}_{NR1} \\ \mathbf{n}_{NR2} \\ \mathbf{n}_{NR3} \end{bmatrix} \tag{33}$$

$$\mathbf{y}_{NRN} = \mathbf{W}_{NRN}\mathbf{x}_{NRN} + \mathbf{n}_{NRN}$$

$$\mathbf{n}_{NRN} \sim \mathcal{N}\left(\begin{bmatrix}0\\0\\0\end{bmatrix}, \mathbf{C}_{NRN} = \begin{bmatrix}C_{NR1} & 0 & 0\\ 0 & C_{NR2} & 0\\ 0 & 0 & C_{NR3}\end{bmatrix}\right)$$

Trilateration is used in the AFIT NoNET to determine target location. Three NRN nodes are setup in known locations and are assumed to operate in an omnidirectional nature. This concept allows for the formation of range rings to be utilized in image reconstruction [24]. The corresponding weight model for trilateration is

$$w_{i,j}^{Trilateration} = \begin{cases} 1, & \text{if } \mathrm{r}_{\mathrm{inner,i}}^2 \leq (\mathrm{x_j} - \mathrm{h})^2 + (\mathrm{y_j} - \mathrm{k})^2 \leq \mathrm{r}_{\mathrm{outer,i}}^2 \\ 0, & \text{otherwise} \end{cases} \tag{34}$$

where x_j is the x coordinate of the jth pixel, y_j is the y coordinate of the jth pixel, h is the x coordinate of the AFIT NoNET, k is the y coordinate of the AFIT NoNET, $r_{inner,i}$ is the inner radius of the range ring which equals

$$r_{inner,i} = r_i - \frac{R_{res}}{2} \tag{35}$$

where r_i is the ith range and R_{res} is the range resolution. $r_{outer,i}$ is the outer radius of the range ring which equals

$$r_{outer,i} = r_i + \frac{R_{res}}{2} \tag{36}$$

Equation (34) reveals that the trilateration weight model operates similar to a binary selection matrix. Trilateration uses a ring-shaped pattern, centered at the AFIT NoNET node's known coordinates (h, k) whose region is bounded by the sensor's empirical range resolution [24].

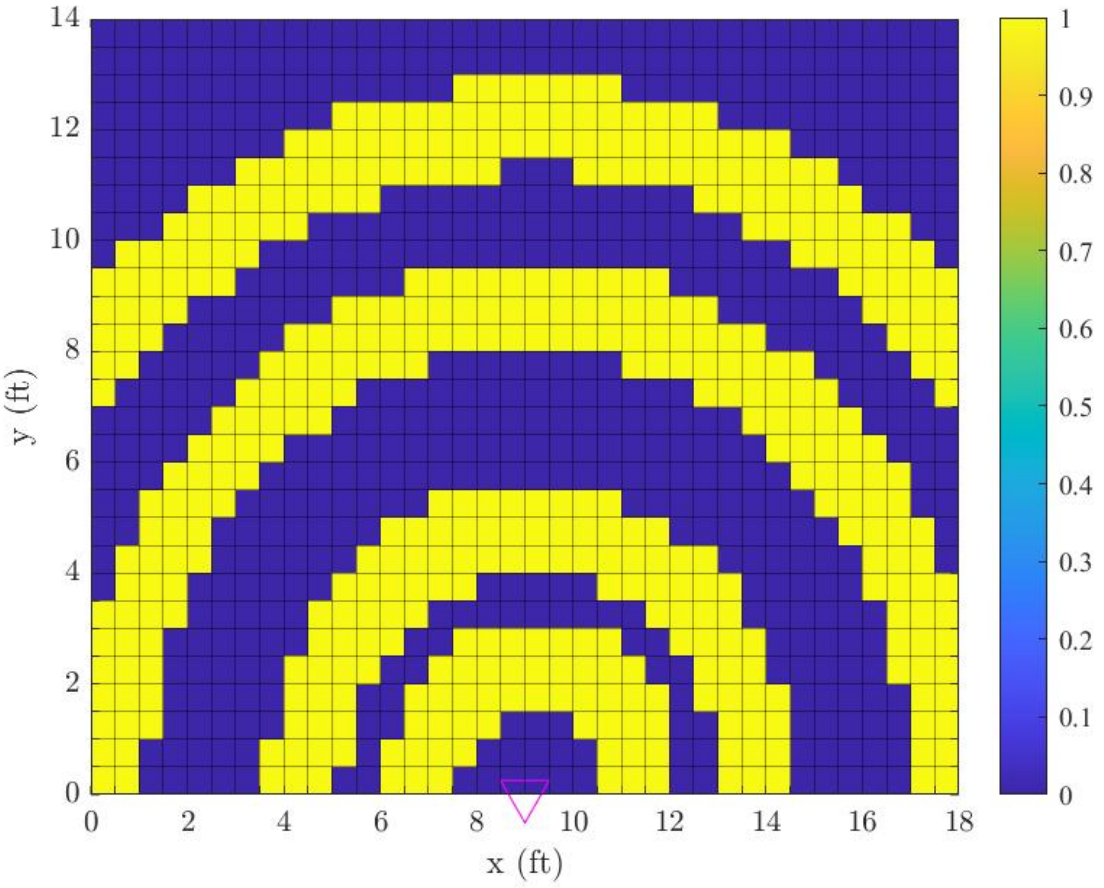

Figure 2.6: Previous NRN weight matrix for binary selection matrix with four respective range rings at noise radar node at (9,0).

Figure 2.6 demonstrates the true attenuation image for four respective range rings with the previous NRN weighting method. These range rings represent four arbitrarily chosen range rings from a single noise radar to demonstrate the operation of the noise radars. Each range ring is weighted by Equation (34) which utilizes the image pixels for trilateration in the form of a binary selection matrix. Currently there are a wide range of RTI weighting models, with four primary models discussed in Section 2.1.2; however, there is only a single NRN model. The limitation of NRN weighting models severely limits the research which can be conducted on NRN topics. Without additional weighting models, research must be shifted to areas which involve

modifying experimental conditions instead of data and image processing methods.

2.3 Data Fusion

Data fusion is a highly researched topic today. It involves the utilization of multiple sensor streams of data and combining that into something more beneficial than a single stream of sensor data. To properly fuse disparate data, various mathematical methods and technical tools are used in order to obtain information which is of higher quality [28]. Fused data can provide additional resolution, accuracy, and situational awareness as opposed to single stream data. The advantages of data fusion can be directly applied to RTI and NRN systems. Due to the disparate nature and system designs, their data cannot be directly applied to each other. RTI and NRN share the same goal of providing target detection and tracking in robust environments. These goals are accomplished through different means, namely radio shadowing for RTI and radio reflection for NRN. A preliminary data fusion model proposed by Vergara [24] is shown as

$$\begin{bmatrix} \mathbf{y}_{RTI} \\ \mathbf{y}_{NRN} \end{bmatrix} = \begin{bmatrix} \mathbf{W}_{RTI} \\ \mathbf{W}_{NRN} \end{bmatrix} \mathbf{x}_{FUS} + \begin{bmatrix} \mathbf{n}_{RTI} \\ \mathbf{n}_{NRN} \end{bmatrix} \tag{37}$$

which simplifies into

$$\mathbf{y}_{FUS} = \mathbf{W}_{FUS}\mathbf{x}_{FUS} + \mathbf{n}_{FUS} \tag{38}$$

$$\mathbf{n}_{FUS} \sim \mathcal{N}\left(\begin{bmatrix} 0 \\ 0 \end{bmatrix}, \mathbf{C}_{FUS} = \begin{bmatrix} \mathbf{C}_{RTI} & 0 \\ 0 & \mathbf{C}_{NRN} \end{bmatrix} \right)$$

where $\mathbf{y}_{RTI}$ is the calibrated RSS values from M links in the RTI network, $\mathbf{y}_{NRN}$ is the stacked, calibrated impulse response/cross-correlation magnitudes from each NRN node, and $\mathbf{x}_{FUS}$ is the fusion image of the RTI and NRN sensors. In order to reconstruct a fused image based on Equation (38), it is necessary to take the

maximum likelihood (ML) derivation. Similar to 2.1.3.1, the derivation from Vergara [24] will follow the format of

$$\begin{aligned}\hat{\mathbf{x}}_{FUS,ML(y)} &= \underset{\hat{\mathbf{x}}_{FUS}}{argmax} \ln \varphi \left(\mathbf{y}_{FUS} | \mathbf{x}_{FUS} \right) \\ &= \underset{\hat{\mathbf{x}}_{FUS}}{argmax} \mathcal{L}\end{aligned} \tag{39}$$

where $\mathcal{L}$ is the log likelihood function, where the noise vector is assumed to be $\mathbf{n_{FUS}} \sim \mathcal{N}(0, C_{FUS})$. This results in $\mathbf{y} \sim \mathcal{N}(\mathbf{W}_{FUS}\mathbf{x}_{FUS}, \mathbf{C}_{FUS})$ and therefore Vergara [24] simplifies as

$$\mathcal{L} = -N \ln \sqrt{2\pi} - \ln |\mathbf{C_{FUS}}| + f(\mathbf{x}_{FUS}) \tag{40}$$

Setting up to solve for $\mathbf{x}_{FUS}$ in order to get the argmax

$$\nabla_x \mathcal{L} \equiv 0 \tag{41}$$

where $\underset{\hat{\mathbf{x}}}{argmax}$ is the solution to Equation (41). Therefore, $f(\mathbf{x}_{FUS})$ becomes

$$\hat{\mathbf{x}}_{FUS} = \left(\mathbf{W}_{FUS}^T \mathbf{C}_{FUS}^{-1} \mathbf{W}_{FUS} \right)^{-1} \mathbf{W}_{FUS}^T \mathbf{C}_{FUS}^{-1} \mathbf{y}_{FUS} \tag{42}$$

Since $\hat{\mathbf{x}}_{FUS} = \left(\mathbf{W}_{FUS}^T \mathbf{C}_{FUS}^{-1} \mathbf{W}_{FUS} \right)^{-1}$ is not invertible, Tikhonov regularization is applied by inputting $\alpha_{FUS}||\mathbf{Q}\mathbf{x}_{FUS}||^2$ into $f(\mathbf{x}_{FUS})$ in Equation (40) [24]. By inputting $\alpha_{FUS}||\mathbf{Q}\mathbf{x}_{FUS}||^2$ into $f(\mathbf{x}_{FUS})$, certain desired properties can be enforced by utilizing the tunable parameter α_{FUS} which has the capability of smoothing the data where small values lead to solutions that fit the data and large values favor prior information

[24]. After simplifying, Vergara's [24] result is shown as

$$\hat{\mathbf{x}}_{FUS} = \underbrace{\left(\mathbf{W}_{FUS}^T \mathbf{C}_{FUS}^{-1} \mathbf{W}_{FUS} + \alpha_{FUS}\mathbf{Q}\right)^{-1} \mathbf{W}_{FUS}^T \mathbf{C}_{FUS}^{-1}}_{\Pi_{FUS}} \mathbf{y}_{FUS} \tag{43}$$

Simplified, Equation (43) becomes

$$\hat{\mathbf{x}}_{FUS} = \Pi \mathbf{y}_{FUS} \tag{44}$$

where Π is given by

$$\Pi = \left(\mathbf{W}_{FUS}^T \mathbf{C}_{FUS}^{-1} \mathbf{W}_{FUS} + \alpha_{FUS}\mathbf{Q}\right)^{-1} \mathbf{W}_{FUS}^T \mathbf{C}_{FUS}^{-1} \tag{45}$$

This provides the ability to reconstruct images based on Tikhonov regularization for both RTI and NRN. Based on user needs, the tunable parameter, α_{FUS}, could be adjusted for each separate image, discussed in Section 2.3.1 or the fusion of images with disparate data. Vergara [24] introduces a method which includes a tunable parameter, β. This parameter increases the scaling of the weight matrix for one of the desired sensor's data. The intention of the β parameter is to account for the disparities between the two types of sensor systems. While the tunable parameter could be applied to one or both of the respective weight matrices, it was applied to the RTI weight matrix [24]. The new system model proposed is

$$\begin{bmatrix} \mathbf{y}_{RTI} \\ \mathbf{y}_{NRN} \end{bmatrix} = \begin{bmatrix} \beta_{RTI}\mathbf{W}_{RTI} \\ \mathbf{W}_{NRN} \end{bmatrix} \mathbf{x}_{FUS} + \begin{bmatrix} \mathbf{n}_{RTI} \\ \mathbf{n}_{NRN} \end{bmatrix}, \ \beta_{RTI} > 0 \tag{46}$$

Vergara [24] optimizes the β_{RTI} parameter for his hardware setup and experimental conditions to equal 26.31, providing optimal RTI and fused image performance

increases.

Another method which was used by Vergara [24] was a Kalman filter. A Kalman filter is an optimal estimation algorithm which can predict a parameter of interest. For purpose of this thesis, target position is the estimated parameter based on the RTI and NRN data. Kalman filtering involves following the Kalman filter dynamic system model format given by

$$\hat{\mathbf{x}}_{KAL,k} = \mathbf{F}_k \hat{\mathbf{x}}_{KAL,k-1} + \mathbf{B}_k \mathbf{u}_k + \mathbf{w}_k \tag{47}$$

where $\mathbf{F}_k$ is the state transition model applied to the previous state $\mathbf{x}_{k-1}$, $\mathbf{B}_k$ is the control input model applied to the control vector $\mathbf{u}_k$, $\mathbf{w}_k$ is the process noice assumed to be drawn from a zero mean multivariate normal distribution with covariance $\mathbf{Q}_k$, and $\hat{\mathbf{x}}_{KAL}$ is the Kalman filter solution for the estimated target position from the RTI attenuation and NRN reflection/backscatter images generated using the ML estimate with Tikhonov regularization [24]. For state reference, $\mathbf{z}_k$ needs to be an observation of the true state vector $\mathbf{x}_k$, shown as

$$\mathbf{z}_\mathrm{k} = \mathbf{H}_\mathrm{k} \mathbf{x}_\mathrm{k} + \mathbf{v}_\mathrm{k} \tag{48}$$

where $\mathbf{H}_k$ is the observation model mapping the true state space into the observed space, and $\mathbf{v}_k$ is the observation noise assumed to be zero mean Gaussian white noise with covariance $\mathbf{R}_k$ [26]. The prediction equation uses the previous time step's state estimate, $\hat{\mathbf{x}}_{KAL,k-1}$, to estimate the state of the current time step

$$\hat{\mathbf{X}}_{KAL,k} = \mathbf{F}_k \hat{\mathbf{x}}_{KAL,k-1} + \mathbf{B}_k \mathbf{u}_k \tag{49}$$

with the predicted error covariance given by

$$\hat{\mathbf{P}}_{KAL,k} = \mathbf{F}_k \hat{\mathbf{P}}_{KAL,k-1} \mathbf{F}_k{}^T + \mathbf{Q}_k \tag{50}$$

Equation (49) and Equation (50) are references as the *a priori* state estimate and error covariance due to not containing observation information from the current time step [24]. In order to update information, the update equation utilizes *a priori* prediction state estimate in Equation (49) with the current observation information in Equation (48) to update the state estimate, $\hat{\mathbf{x}}_{KAL,k}$

$$\hat{\mathbf{x}}_{KAL,k} = \hat{\mathbf{X}}_{KAL,k} + \mathbf{K}_k(\mathbf{z}_k - \mathbf{H}_k \hat{\mathbf{X}}_{KAL,k}) \tag{51}$$

where $\mathbf{K}_k$ is the Kalman gain, given by

$$\mathbf{K}_k = \mathbf{P}_k \mathbf{H}_k{}^T (\mathbf{R}_k + \mathbf{H}_k \bar{\mathbf{P}}_k \mathbf{H}_k{}^T) \tag{52}$$

The updated error covariance matrix, $\mathbf{P}_k$ is

$$\mathbf{P}_k = (\mathbf{I} - \mathbf{K_k}\mathbf{H})\bar{\mathbf{P}}_k \tag{53}$$

Equation (51) and Equation (53) are respectively known as the *a posteriori* state estimate and the *a posteriori* error covariance matrix to differentiate them from the prediction equations shown as Equation (49) and Equation (50) [24, 26].

For data fusion between RTI and NRN, the Kalman filter solution becomes

$$\begin{bmatrix} \hat{\mathbf{x}}_{\mathrm{RTI}} \\ \hat{\mathbf{x}}_{\mathrm{NRN}} \end{bmatrix}_k = \begin{bmatrix} 1 & 0 \\ 0 & 1 \end{bmatrix} \mathbf{x_k} + \mathbf{v_k} \tag{54}$$

$$\mathbf{v_k} \sim \mathcal{N}(0, \mathbf{R})$$

Equation (54) is an observation of the estimated target location of the RTI and NRN regularized images $\hat{\mathbf{x}}_{\text{RTI}}$ and $\hat{\mathbf{x}}_{\text{NRN}}$, with inherent and individualized pixel noise $\mathbf{v}_k$. The observation model, $\mathbf{H}_k$, is represented by an identity matrix, which means that the contribution of the pixels from the RTI and NRN Tikhonov regularized images are only subject to their respective noise in $\mathbf{v}_k$ [24]. While Vergara [24] only explored Tikhonov regularization for image reconstruction, Battle [2] proposed and implemented additional reconstruction models in Section 2.1.3 for RTI image reconstruction.

2.3.1 Separate Image Fusion

Separate image fusion is beneficial because it does not rely on scaling disparate data streams. Vergara [24] proposed two methods of separate image fusion: Averaging and Kalman filtering. Averaging involves normalizing the RTI and NRN images separately, then averaging the images to form a fused image. This method can be conducted easily since images have already been formed, and they match the proper image dimension and resolution for RTI and NRN data inputs. This method is rigid and does not allow for modifications to be made to the raw data. If one of the sensor systems performances is degraded in a certain target scenario, the fused image will reflect this directly.

III. Methodology

The initial decisions made were which Radio Tomographic Imaging (RTI) models and algorithms would be utilized within the created testbed. The primary selection decision involves performance and ability to relate the respective RTI model to Noise Radar Network (NRN). It will also be necessary to select various parameters for RTI in certain situations based on model and algorithm utilized. The testbed will allow for full user customization of required parameters.

This thesis involved a multi-step approach to effectively apply RTI research to NRN with a testbed. The first step involved the creation of a testbed with the capability of utilizing experimental and simulated data with various desired models and algorithms to compare their performance with ease. No universal testbed approach had been previously constructed so it would be necessary to create one. Proof of concept that a testbed could be utilized to improve device-free localization (DFL) capabilities of through-wall sensing was demonstrated by Vergara [24]. Battle [2] utilized a model switching approach to their RTI research which can be directly applied to this thesis.

Following the testbed creation, it can be utilized to study and compare the effects of models and algorithms for both fusion and separate images of RTI and NRN. By creating a common framework to accurately assess and apply proven RTI methods to NRN, new methods to improve and expand NRN can be found. For example, based on RTI research, it is necessary to propose a new weighting method for NRN. The new NRN weighting matrix will allow for a more direct representation of RTI research to be conducted with NRN research. The testbed has the ability to use insights in a proven research area and notionally apply them in a similar way.

3.1 RTI Considerations

Prior to the creation of the testbed, some RTI considerations must be declared. Numerous RTI weight models are available; however, for the purpose of this thesis the NeSh and weighting-g models were chosen. The weight models not included in this thesis are present within the testbed but were not analyzed within this iteration of the testbed. Weight models are important because they affect the received signal strength (RSS) measurements from the sensors and how the RTI links are used. These weight models were chosen for their ability to relate to the new NRN weight matrix which is proposed in Section 3.6. The NeSh model is the most common RTI model and it employs an ellipse to simplify determining which pixels lie along the LOS path [2, 7]. The multipath interference is mitigated by setting the width of the ellipse low, and setting contributions from pixels outside of the LOS path to zero. The weighting-g model was chosen because it contains the same basic employment of an ellipse used by the NeSh model, however, with an additional pixel weighting within each respective ellipse node link. The additional pixel weighting within the ellipse provides additional accuracy due to the assignment of values based on the distance between each pixel inside the ellipse and the LOS path [2, 15]. The foundational concepts of these models were utilized in developing a new weight matrix for NRN in Section 3.6.

For RTI image reconstruction, Tikhonov regularization was chosen. It is the most widely used reconstruction method and was utilized by Vergara [24] in the proof of concept research of fusing RTI and NRN data.

The regularization parameter, α_{RTI}, is utilized in image reconstruction for RTI. The regularization parameter allows for smoothing of the reconstructed attenuation image. Smoothing an image provides less background interference when compared to the target but decreases true target localization accuracy. It is important to find

a balanced value which decreases unwanted image artifacts while provide accurate target localization. The regularization parameter α_{RTI} is affected by image resolution and reconstruction method, therefore it will be necessary to have baseline values for each scenario chosen.

Figure 3.1 and Figure 3.2 show the effect which the smoothing term, α, has on the reconstruction of RTI images using different weighting models. The optimal smoothing term is dependent on many factors, to include image resolution, target

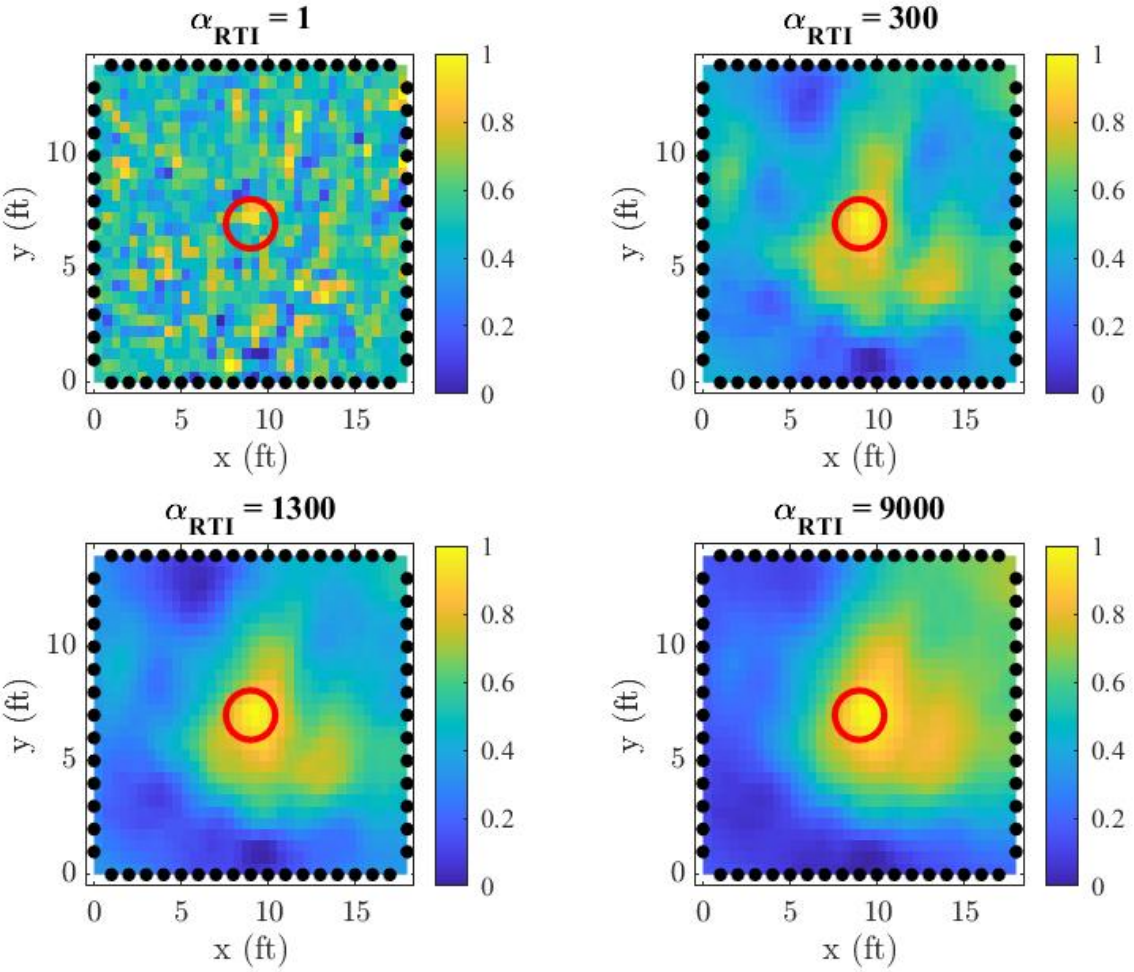

Figure 3.1: Effects of alpha on RTI attenuation image using NeSh weight model and Tikhonov reconstruction for the true target location (9,7) at the red circle.

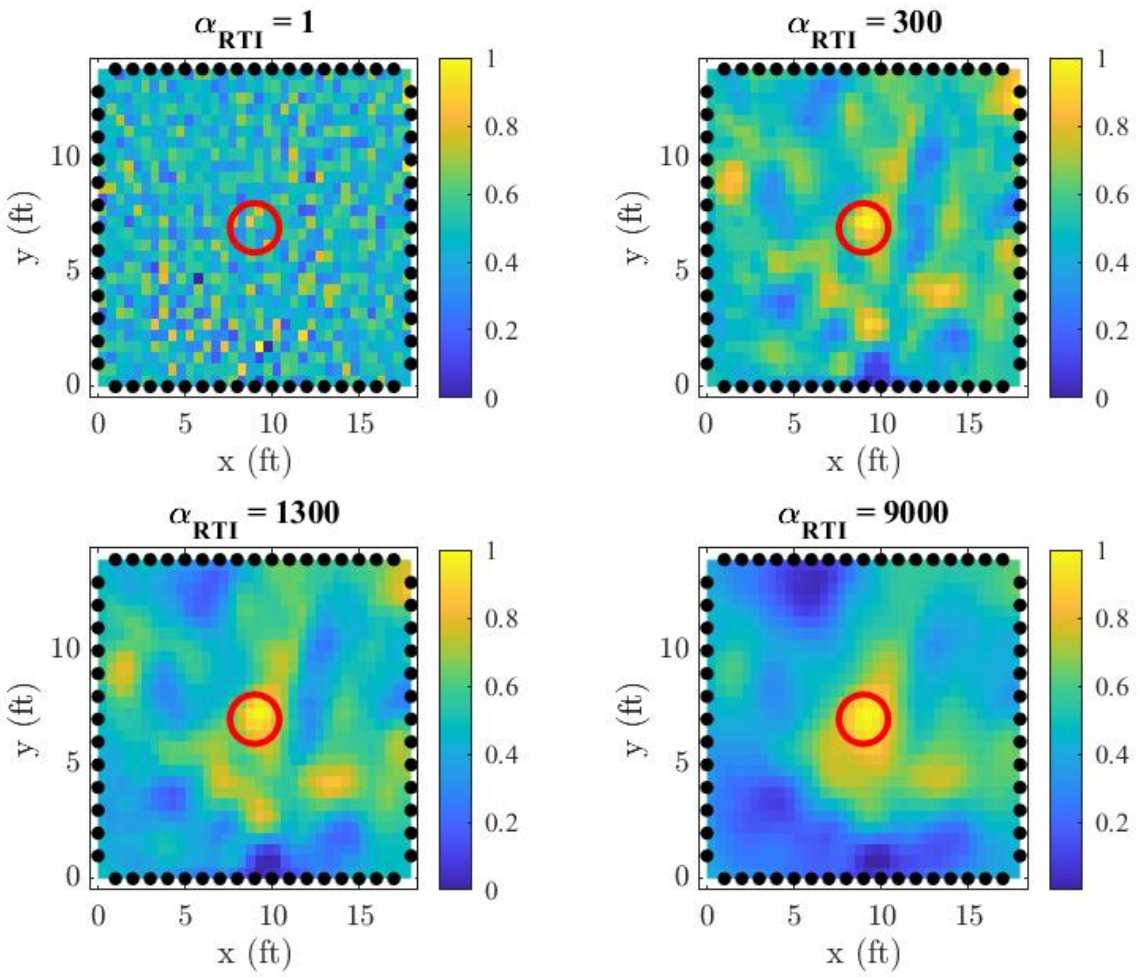

Figure 3.2: Effects of alpha on RTI attenuation image using weighting-g model and Tikhonov reconstruction for the true target location (9,7) at the red circle.

environment, and weighting model. In order to find the optimal value, a wide range of α values are used, and the performance metrics discussed in Section 3.5 are utilized for each target scenario to determine the α value which localizes the target with the lowest average error. The minimum and maximum values should encompass regions where target localization is inaccurate, therefore bounding values which improve target localization within them. These empirically determined optimal α values for each weighting model and reconstruction method pair are averaged across the three target scenarios. The target scenarios are single targets within a test environment, with

locations of (9,7), (4,10), and (14,4) respectively. After running optimization tests for each RTI weighting model across each target scenario, the average results were calculated. Based on the optimization test for the current image resolution of 0.5 ft,, the NeSh model smoothing term is $\alpha = 432.8$ and the weighting-g model smoothing term is $\alpha = 2990.8$. Each additional weight model and reconstruction method would need to undergo this optimization test in order to find the optimal smoothing term for the respective pair.

Each of the RTI weighting models requires determination of a λ value, which is the width of the ellipse in the node link. Each model commonly sets varying values of λ to optimize detection and minimize interference which may differ from other models. The width of the ellipse is important in the pixel weighting when the user desires the mitigation of multipath effects along with accurate target localization.

Figure 3.3 and Figure 3.4 show the effect which the ellipse width, λ, has on the reconstruction of RTI images using different weighting models. The optimal ellipse width is dependent on many factors, to include image resolution and weighting model. In order to find the empirically optimal value, a wide range of λ values are used, and the performance metrics discussed in Section 3.5 are utilized for each target scenario to determine the λ value which localizes the target with the lowest average error. The optimal λ, values for each weighting model and reconstruction method pair are averaged across the three target scenarios. After running optimization tests for each RTI weighting model across each target scenario, the average results were calculated. Based on the optimization test for the current resolution, the NeSh model ellipse width is $\lambda = 0.0542$ ft and the weighting-g model ellipse width is $\lambda = 0.0248$ ft. Each additional weight model would need to undergo this optimization test in order to find the optimal ellipse width.

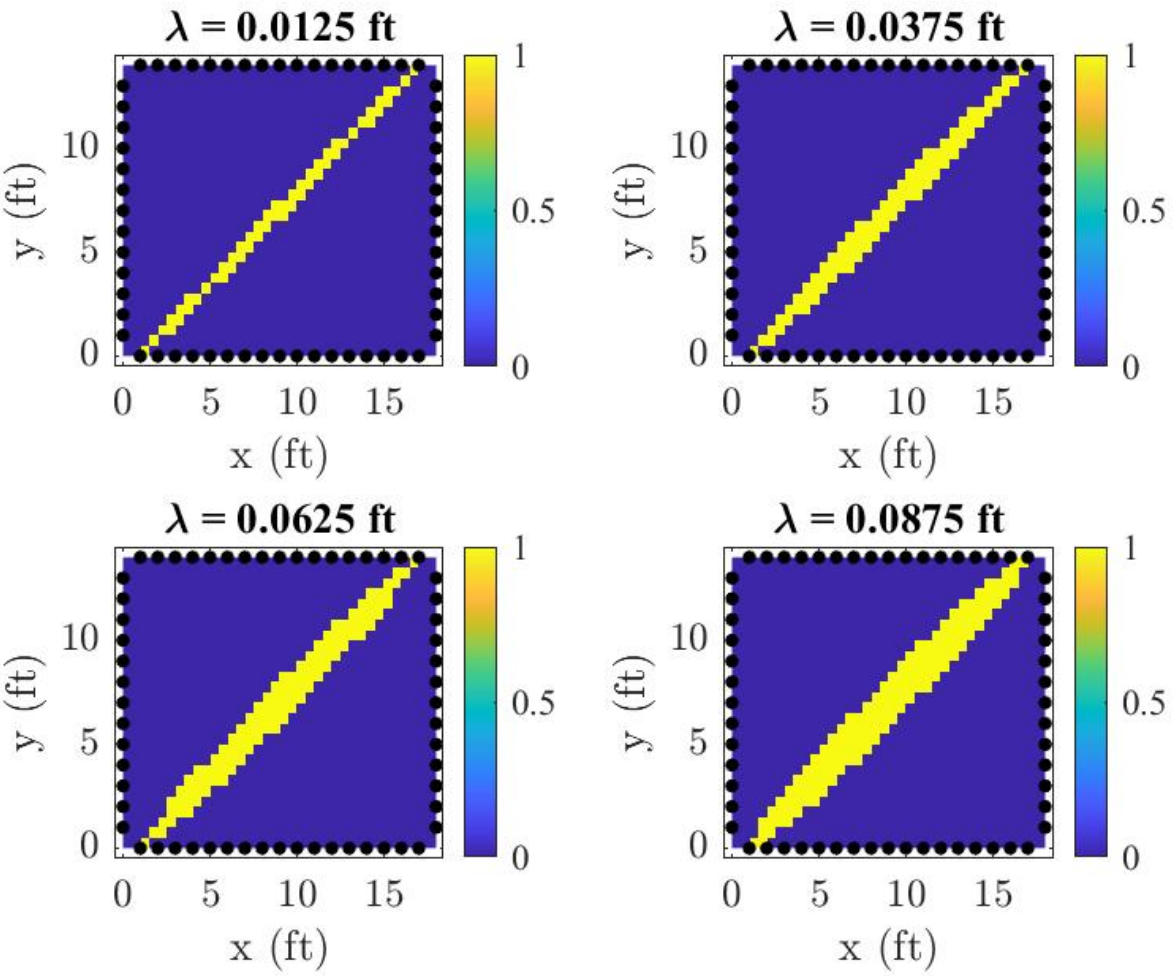

Figure 3.3: Single weight link with ellipse width variation for NeSh weighting and Tikhonov reconstruction.

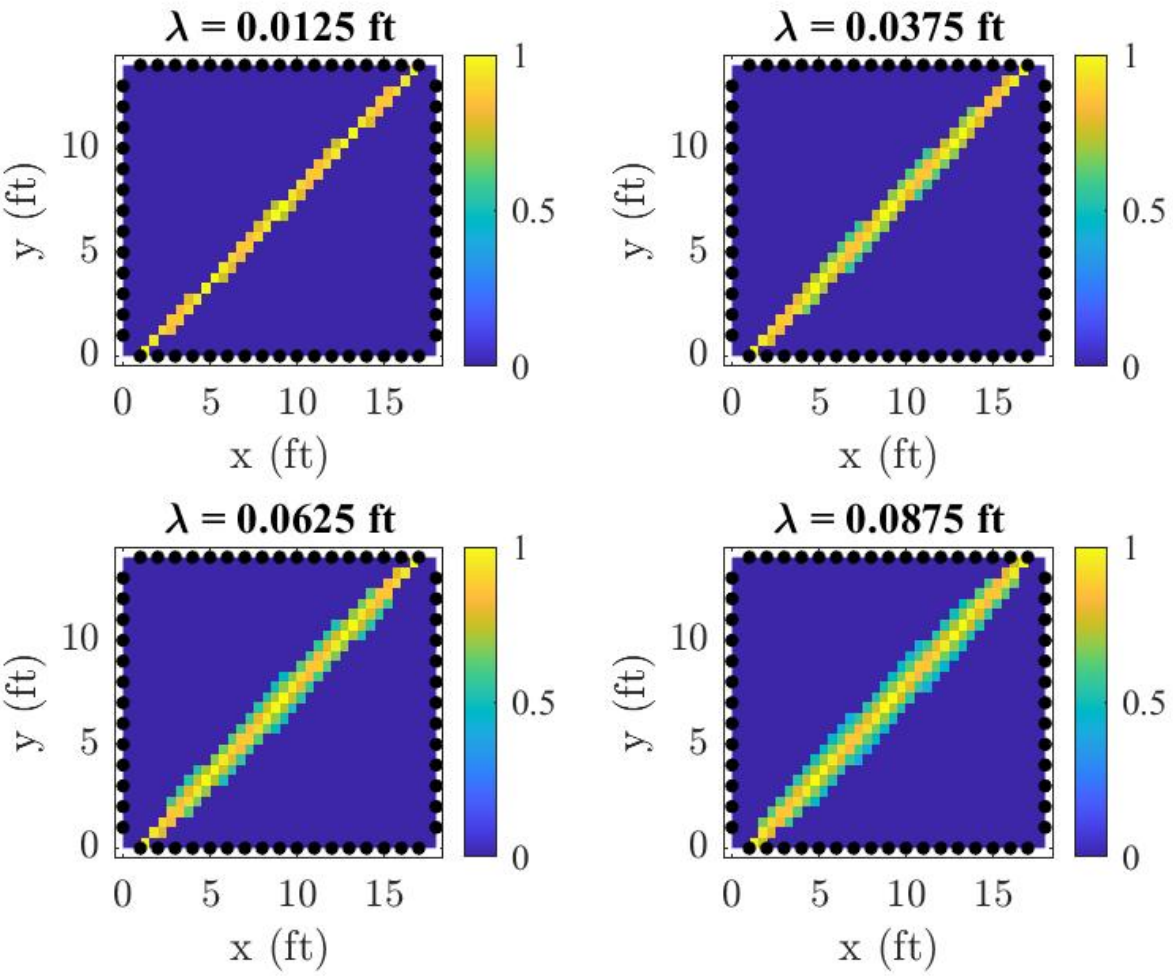

Figure 3.4: Single weight link with ellipse width variation for weighting-g and Tikhonov reconstruction.

3.2 NRN Considerations

Previous research and research conducted in this thesis utilized three noise radar nodes within data gathering and analysis. NRN data collected by Vergara [24] was completed with access to only a single noise radar node. Results were gathered by moving the noise radar node to each respective position while keeping the target environment the same. Additional noise radar nodes would be preferable for data collection, reducing data collection time for the user. Similar to Section 3.1, NRN includes a smoothing term, α_{NRN}, which must be optimized for proper usage. The purpose of this smoothing term is to provide a higher degree of accuracy to the resulting NRN image. Smoothing refers to reducing overall image intensity variations in order to reduce noise and other unwanted image artifacts. If there is too much smoothing present, target localization becomes difficult due to peaks being reduced and spread out.

Figure 3.5 and Figure 3.6 show the effect which the smoothing term, α, has on the formation of NRN images utilizing two different weighting methods. The optimal smoothing term is dependent on many factors, to include image resolution and weighting model. After running optimization tests for each NRN weighting method across each target scenario, the average results were calculated. The optimization test for the NRN α is the same as the RTI except the only consideration is weighting method since there is no additional reconstruction methods. The new weighting methods are defined and discussed in Section 3.6. Based on the optimization test for the current image resolution of 0.5 ft, the binary selection matrix weighting smoothing term is $\alpha = 609.47$, the Jans Weighting Method (JWM) smoothing term is $\alpha = 361.33$, the JWM with linear weighting smoothing term is $\alpha = 1557.6$, the JWM with exponential weighting smoothing term is $\alpha = 2062.4$, and the JWM with focused weighting smoothing term is $\alpha = 216.73$. The additional methods of NRN weighting are dis-

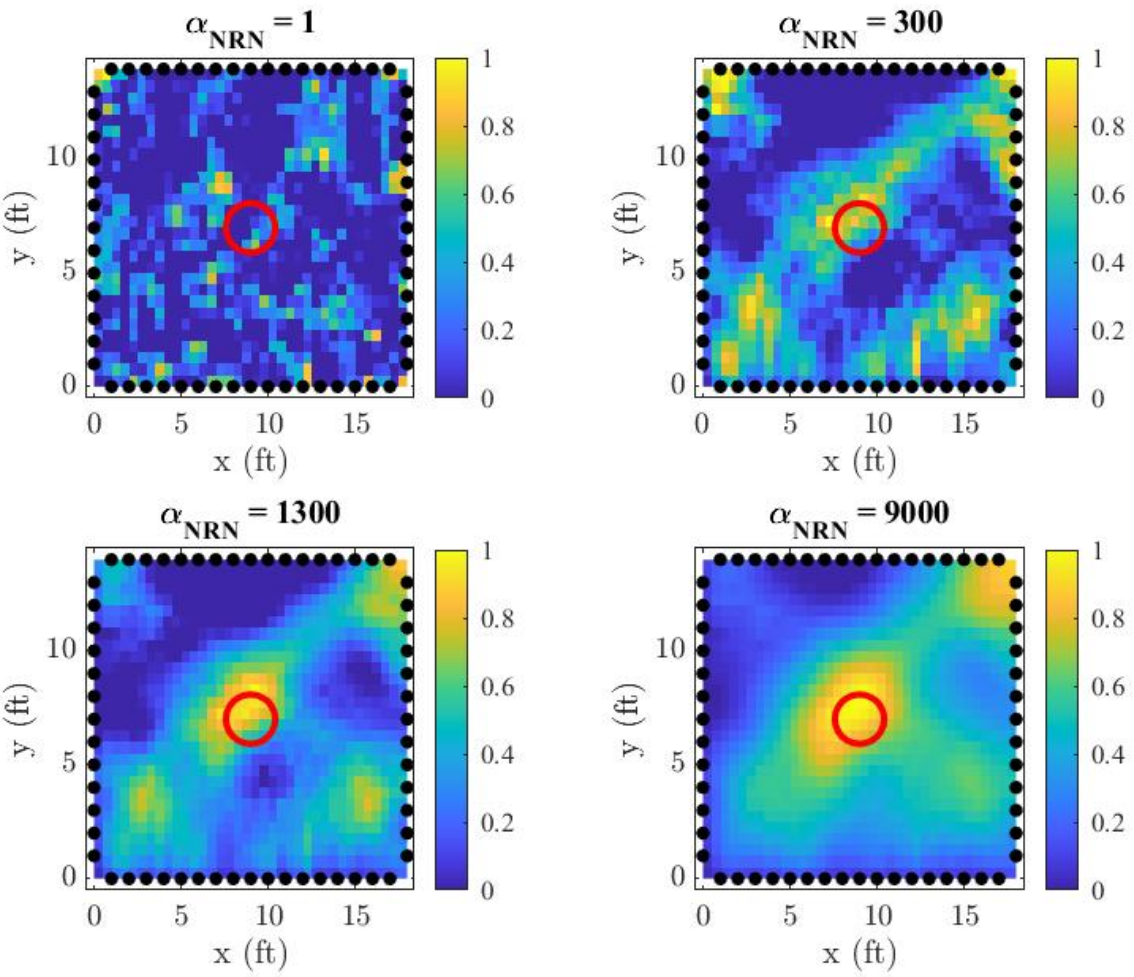

Figure 3.5: Alpha smoothing terms for NRN binary selection matrix with target at (9,7).

cussed in Section 3.6. In previous NRN research, the α values were arbitrarily chosen based on aesthetics instead of target localization accuracy. Additionally, each individual target scenario has its own smoothing term which is optimal only for that target scenario. For purpose of this thesis, smoothing terms for weighting methods are averaged across the three target scenarios.

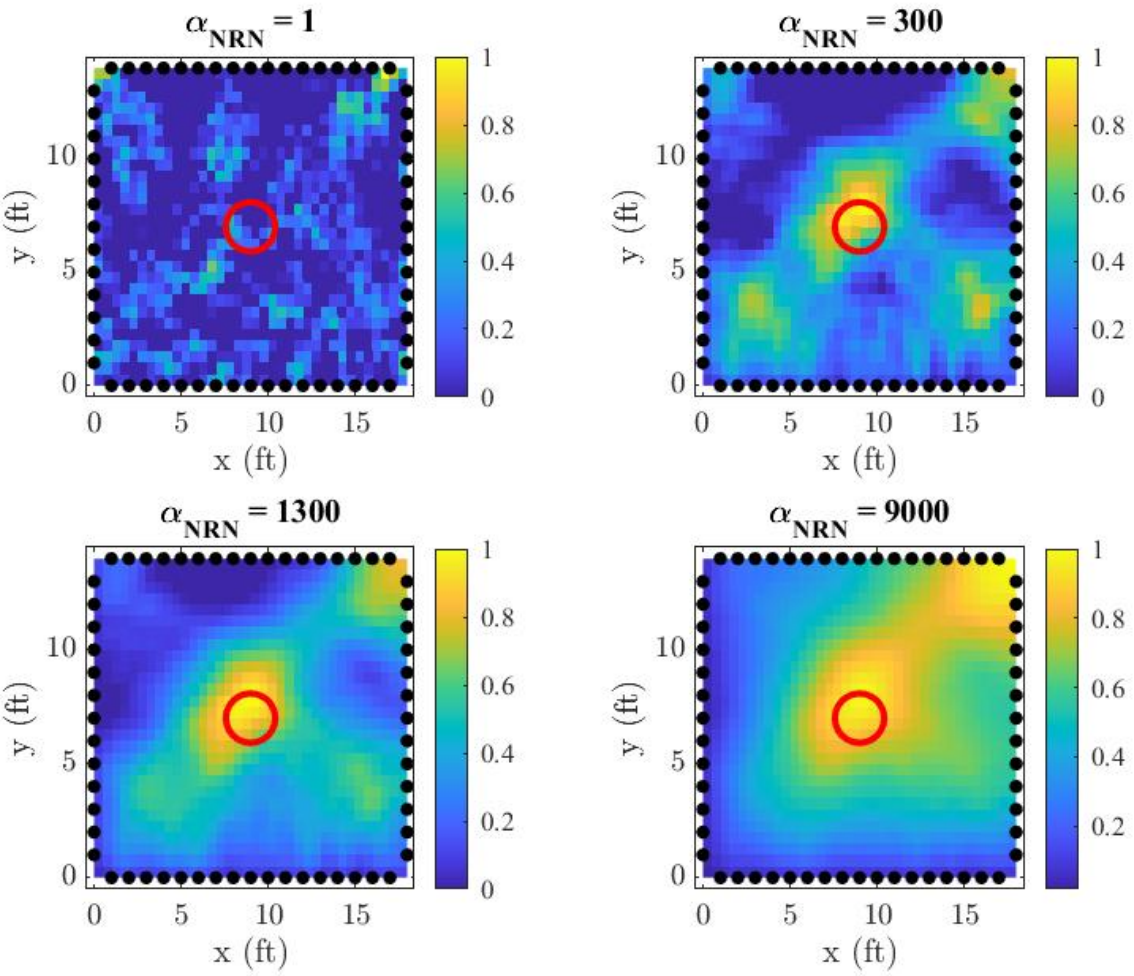

Figure 3.6: Alpha smoothing terms for NRN proposed weight matrix with focused weighting for target at (9,7).

3.3 Target Model Selection

A target model is required to model and represent the approximate attenuation field that is being estimated. This model can be selected and switched dependent on use case desired by the user. For purpose of this thesis, the human cylindrical model is chosen to represent the attenuation caused by potential target(s) [7]. This target model was chosen as it represents the primary use case of research in RTI and NRN. This model represents a human target by modeling it as a uniformly attenuating cylinder where

$$\mathbf{x}_{cj} = \begin{cases} 1, & \text{if } ||\mathbf{x}_j - \mathbf{c}_H|| < R_H \\ 0, & \text{otherwise} \end{cases} \tag{55}$$

where $\mathbf{x}_{cj}$ is the center of the image pixel j, $\mathbf{x}_j$ is the location of pixel j, $\mathbf{c}_H$ is the true target or human location, and R_H is the human radius [2, 4, 7]. The radius selected by Wilson and Patwari [7] utilizes 1.3 meters to model the attenuation field caused by a human in the target area.

Figure 3.7 demonstrates the true attenuation image for the human cylindrical model. It is necessary to create a true image to accurately determine performance of the respective models and reconstruction methods utilized within the testbed. Without reference, the desired performance metrics cannot be accurately determined. The same process is utilized for multi-target scenarios.

Figure 3.8 demonstrates a multi target true attenuation image. If targets overlap within the 1.3 meter radius, target localization accuracy will be affected. Mitigation of overlap is dependent on target localization method, network configuration, and RTI weighting and reconstruction method utilized.

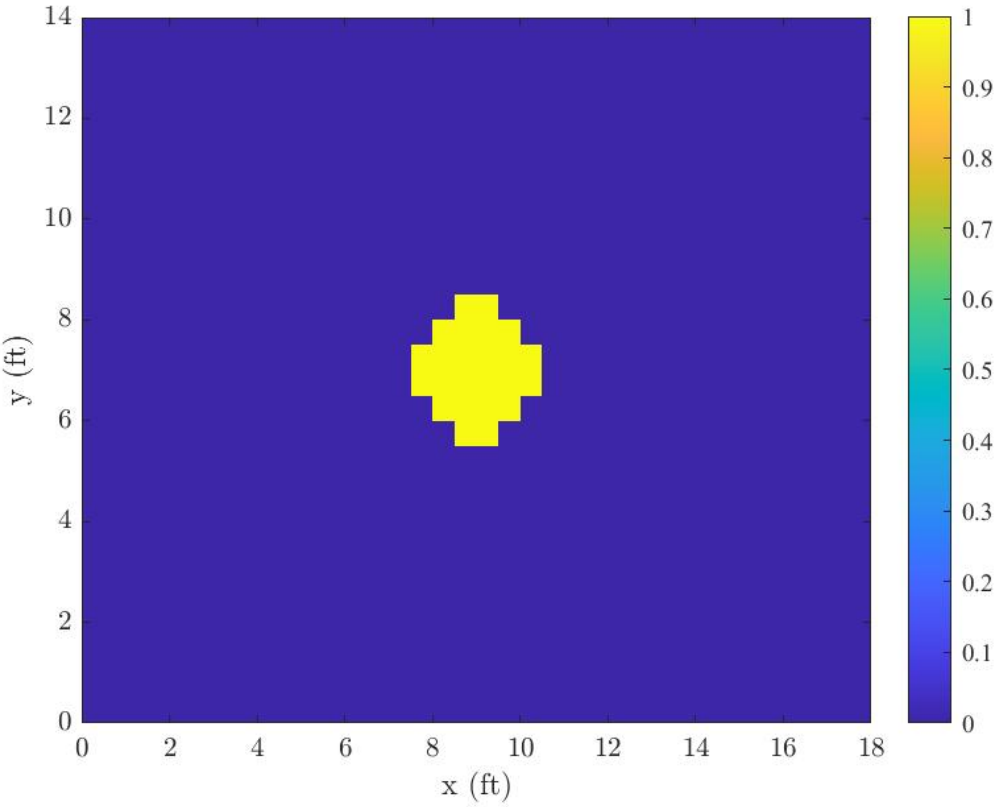

Figure 3.7: Ideal attenuation image for human cylindrical model at (9,7).

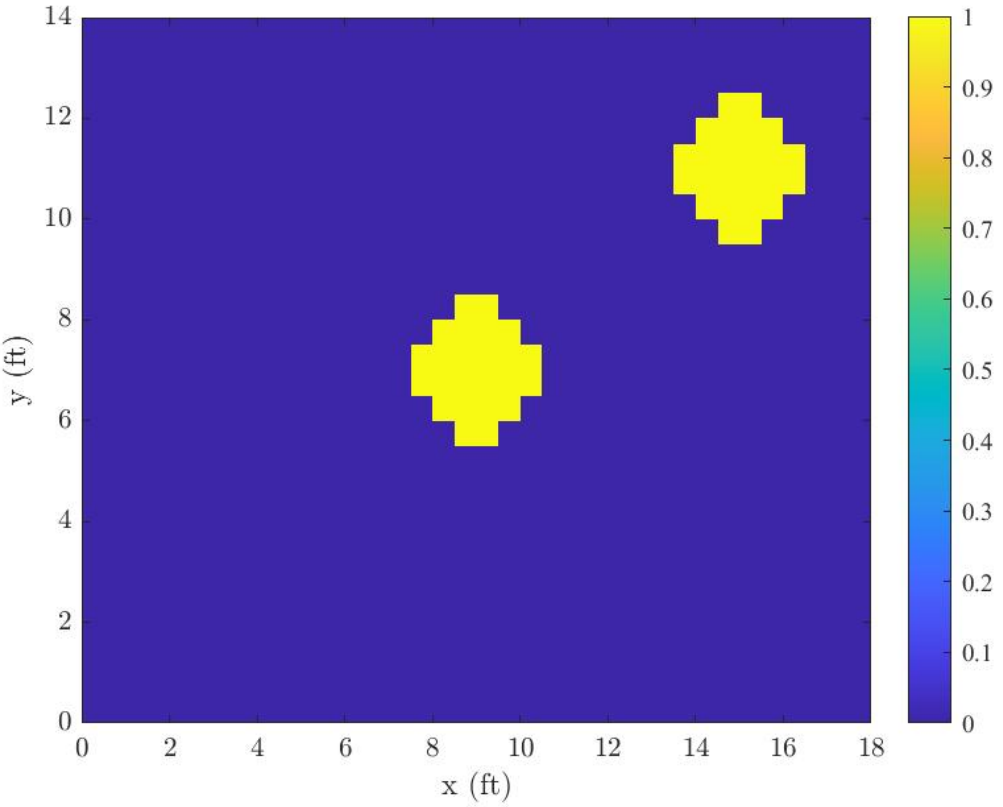

Figure 3.8: Ideal attenuation image for human cylindrical model with multiple targets at (9,7) and (15,11).

3.4 Target Localization

Target localization is conducted after formation of attenuation images. The images could range from separate RTI or NRN, or their respective fused images. Target localization algorithms must be chosen with respect to the number of potential targets within the area tested. Algorithms that provide the ability to localize multiple targets are preferable if the number of targets in the area being tested is unknown. Single target localization is relatively ineffective due to the number of true targets being unknown. While it may provide information on the strongest target return or location within the testing environment, it cannot be primarily relied upon due to the number of true targets being unknown.

3.4.1 Single Target Localization

A simple method for single target localization utilizes the center of the highest intensity pixel. This method is referred to as a maximum a posteriori estimator (MAP). The center of the image pixel location becomes the estimated target location [2, 15, 16]. This simple determination becomes

$$\hat{\mathbf{z}} = [x_k, y_k] \tag{56}$$

where $k = \arg\max(\mathbf{x})$, x_k is the x-coordinate of the highest intensity pixel, and y_k is the y-coordinate of the highest intensity pixel [2, 16, 29]. This method is vulnerable due to lack of multi-target localization capability as well as the inability to reduce potential image artifacts due to noise and multipath effects. Additionally, the accuracy of the target localization is heavily limited to the image resolution chosen by the user. The weight model and reconstruction algorithm require parameters to be tuned to values at or near their empirically optimal values to provide accurate target

localization. Potential pseudo targets and artifacts are detrimental otherwise [15].

3.4.2 Multi-Target Localization

Multi-target localization provides wider use cases, and therefore, their algorithms provide more value. Multi-target localization is especially useful when the number of targets is unknown. The pixel(s) with the highest intensity are still used to determine the location of the target(s); however, additional algorithms ensure a higher degree of accuracy is achieved.

3.4.2.1 Clustering Algorithm

Clustering algorithms are important due to their ability to efficiently and effectively detect targets. Research involving RTI commonly uses a clustering algorithm to provide accuracy in target localization for this purpose. The k-means algorithm was chosen due to its popularity amongst clustering algorithms used for a wide range of applications [30]. The k-means algorithm utilizes a local search approach to minimize the average squared distance between points that form a cluster [2, 30]. The algorithm is given a set of data points and determines k number of clusters. Over-estimation of clusters ensures that the true number of targets within the test environment is detected. Battle [2] demonstrated the effectiveness over over-estimating and the downsides to under-estimating the number of targets. The centers of the clusters are known as centroids, and this positional information is considered the estimated target locations [2, 30]. A threshold is set in order to reduce the number of pixels that are analyzed as possible target locations [2, 10, 30, 31].

3.5 Performance Metrics

Performance metrics are utilized to properly compare quantitative results for each test scenario. The true image, discussed in Section 3.3 is compared with the attenuation image results utilizing various performance metrics. Each test scenario studies the combinations of target location, weight model, reconstruction method, and fusion method to determine the best method for each scenario. Iterations of tests can be conducted to gather higher level performance data to compare additional functionality across user desired scenarios.

3.5.1 Mean-Squared Error of the Image

The first performance metric used was mean-squared error (MSE). MSE determines quality of attenuation image with respect to true image. MSE is defined as

$$MSE = \frac{||\mathbf{x}_c - \hat{\mathbf{x}}_{Norm}||^2}{N} \tag{57}$$

where $\mathbf{x_c}$ is the peak normalized true image with subscript c referring to the human cylindrical model to be discussed in Section 3.3, $\hat{\mathbf{x}}_{Norm}$ is the normalized estimated image, and N is the total number of image pixels [2, 7, 21]. As the computation grid resolution is increased, the MSE is reduced, thus reflecting the importance of a proper attenuation image resolution.

3.5.2 Root-Mean-Squared Error of the Position

The root-mean-squared error (RMSE) was used to measure the error between the true target location(s) and estimated target location(s). The RMSE is given by

$$RMSE = \sqrt{\frac{\Sigma_{m=1}^{M}(||\hat{\mathbf{z}}_m - \mathbf{z}_m||)^2}{M}} \tag{58}$$

where $\hat{\mathbf{z}}_m$ is the m^{th} estimated target location, $\mathbf{z}_m$ is m^{th} true target location, and M is the total number of true and estimated target locations [2, 11]. For this thesis, this metric was utilized along with MSE in Section 3.5.1 because RMSE provides the ability to detect outlier errors within an attenuation image.

3.5.3 Dispersion

In the proof of concept of data fusion between RTI and NRN, [24] utilized the dispersion metric. Battle [2] utilized dispersion to measure the spread of pixels that represent each target in the attenuation image. The pixel intensities are thresholded, with the higher intensity pixels assumed to represent approximate target location. The pixel locations with pixel intensities greater than or equal to the threshold retain their normalized value and signify the target pixels. The pixel locations with intensities that fail to meet the threshold are eliminated [2, 24]. The dispersion $\sigma_{Centroid}$ is estimated as

$$\hat{\sigma}_{Centroid} = \sqrt{\frac{\Sigma_{j=1}^{N_{th}} ||P_j - v||^2 \cdot \hat{x}_j}{\Sigma_{j=1}^{N_{th}} \hat{x_j}}} \tag{59}$$

where P_j is the coordinate of the j^{th} pixel, v is the centroid coordinate location, $\hat{x}_j$ is the magnitude of the j^{th} pixel in the normalized estimated attenuation image after thresholding, and N_{th} is the total number of pixels selected via thresholding [2, 24]. The dispersion of each estimated target in $\hat{\mathbf{x}}_{Norm}$ was calculated and compared to the dispersion of each true target in $\mathbf{x}_{Norm}$. The dispersion error was calculated using

$$\epsilon_{Dispersion} = |\sigma_{Centroid} - \hat{\sigma}_{Centroid}| \tag{60}$$

where $\sigma_{Centroid}$ is the dispersion of the true target (given by the standard deviation of the positions of the pixels within the ideal human cylinder model) in $\mathbf{x}_{Norm}$ and $\hat{\sigma}_{Centroid}$ is the dispersion of the estimated target in $\hat{\mathbf{x}}_{Norm}$ [2, 24].

3.6 NRN Proposed Weight Matrix

The primary focus of this thesis was to apply RTI research to NRN to provide insight and capabilities previously unknown. In order to mimic RTI weight models discussed in Section 2.1.2, it was necessary to create a weighting system which resembled a Wireless Sensor Network (WSN) node link. The node links in an RTI network provide the ability to applying weighting values to collected or simulated data in two facets. The first weighting facet is the ability to adjust the weighting within each respective sensor node link, without having to rely on only weighting based on the dimensions of image pixels. Setting a binary weighting with a desired ellipse width is a viable option, but performance increases when the same ellipse has a higher weight in the ellipse center than the outer sides of the respective ellipse. This discovery, based on RTI research comparison of the NeSh model versus the Weighting-g model, can be applied to NRN research. The second facet, explored in RTI research, is weighting various node links at variable weights. If certain links within a WSN contain sensors which provide more accurate data, it would be preferential to weight the data provided via those sensors at a higher level than other sensors. This RTI research was explored by Nafziger [11] and demonstrated improved performance of the overall RTI network.

The Air Force Institute of Technology (AFIT) Noise Network (NoNET) utilizes three noise radar nodes to conduct trilateration to localize a target, discussed in Section 2.2. Each noise radar node creates range rings, with each range ring distance from its monostatic noise radar node dependent on the measured return time. The range resolution was calculated using Equation (30), creating overlapping range rings of detection area. Vergara [24] utilized Equation (34) to determine image pixel weighting using a binary selection matrix. The calculation was conducted by determining if the center of the respective image pixel was within the respective range ring, based on

the noise radar's characteristics. This method provided basic weighting capabilities, however, new weighting methods would be limited directly by image resolution. Fundamentally, RTI weighting models are reliant on the node links for weighting within their WSN as opposed to the image resolution selected by the user. In previous NRN weighting, there was no intermediate step to determine weighting of the data because trilateration was used in conjunction with the image pixels. This small distinction greatly limited the potential of NRN research. The limitation of only being able to weight images with a binary selection matrix severely limited the additional research which could be conducted with the previous weighting method.

A new NRN weight matrix is proposed to create new weighting methods for this thesis and for future research. The new weight matrix will be a foundational system providing the ability to weight NRN data as well as being able to accept and apply new methods of weighting NRN data. The new proposed NRN weight matrix will be referred to as the JWM.

The JWM consists of an artificial grid within the bounds of the area of interest. The artificial grid has a finer resolution than the image pixels, and therefore allows for a more precise weighting scheme. The artificial grid's resolution for this thesis will be twice as fine per dimension as the image resolution. Previous work by Vergara [24] only utilized the center of image pixels for trilateration. The JWM has the capability to be utilized with equal image pixel resolution or at a finer user specified resolution. This flexibility provides additional resolution for weighting that is not directly reliant on image resolution. The JWM has dimensions which are based on the total number of range indices for the noise radar node and the total number of image pixels.

In order to make this modification while continuing to utilize trilateration, a few modifications were made to Equation (34). The primary modification is the addition of a grid with a finer resolution than the image pixel grid. The secondary modification

is the removal of the binary aspect of the weighting matrix. First, the JWM is initialized based on the sum of the total number of range indices for the noise radar node and the total number of image pixels. For example, if there are 377 range indices for a noise radar node and a total of 1008 image pixels, each JWM weighting matrix index is initialized to zero for the dimensions of 377 by 1008. The dimensions can be modified if a coarser or finer resolution is desired. Additionally, the range indices can be modified by increasing or decreasing the size of the test environment, as well as modifying the sampling interval of the noise radar node when data collection is being conducted. The following equations for JWM are applied independently to each noise radar node.

Once the JWM weight matrix is initialized, there are two stages until the final JWM weight matrix is produced. First, the range rings must reflect the artificial pixel grid instead of the image pixel grid. The artificial pixels which are contained within each respective range ring are determined by the range resolution of the noise radar. The new range rings will contain artificial pixels indexed by m, for each range index. The artificial pixel locations within the test environment are tracked using Cartesian coordinates. Each range ring will have a variable amount of artificial pixels based on the distance from the noise radar, dimensions of the artificial pixel grid, and the range resolution of the noise radar.

The final JWM weighting is created by initializing $w_{i,j}^{JWM}$ to zero, then looping over the artificial pixel index m while computing

$$w_{i,j}^{\mathrm{JWM}} = \begin{cases} w_{i,j}^{\mathrm{JWM}} + w_{i,m}, & \text{if } (\mathrm{x_j} - \mathrm{d} \leq \mathrm{RR_{m,i}^{x}} < \mathrm{x_j} + \mathrm{d}) \quad \& \quad (\mathrm{y_j} - \mathrm{d} \leq \mathrm{RR_{m,i}^{y}} < \mathrm{y_j} + \mathrm{d}) \\ w_{i,j}^{\mathrm{JWM}}, & \text{otherwise} \end{cases} \tag{61}$$

where x_j is the x coordinate of the jth image pixel, y_j is the y coordinate of the jth image pixel, d is the image pixel size, $RR_{m,i}^{x}$ contains the range ring x-coordinates

for each artificial pixel m in each range index i, $RR^{y}_{m,i}$ contains the range ring y-coordinates for each artificial pixel m in each range index i. Index m loops from one to the number of artificial pixels for each pixel jth pixel. The artificial pixel weighting matrix is

$$w_{m,i} = \begin{cases} 1, & \text{if } r^2_{\text{inner},i} \leq (x_m - h)^2 + (y_m - k)^2 < r^2_{\text{outer},i} \\ 0, & \text{otherwise} \end{cases} \tag{62}$$

where x_m is the x coordinate of the mth artificial pixel, y_m is the y coordinate of the mth artificial pixel, h is the x coordinate of the AFIT NoNET, k is the y coordinate of the AFIT NoNET. The inner radius, $r_{\text{inner},i}$, is calculated by

$$r_{\text{inner},i} = r_i - \frac{R_{\text{res}}}{2} \tag{63}$$

where r_i is the ith range and R_{res} is the range resolution. The outer radius, $r_{outer,i}$, equals

$$r_{\text{outer},i} = r_i + \frac{R_{\text{res}}}{2} \tag{64}$$

Equation (61) demonstrates the change in notation from Equation (34) which provides the distinction between the image pixel and the artificial pixel grid. Each artificial pixel is checked to determine if it falls within the image pixel and the respective range ring. Each image pixel is variably set, which means that if there are more artificial pixels within a certain image pixel, that image pixel will be weighted at a higher level to reflect a higher confidence in the data at that location. Equation (61) represents the default weighting of the JWM. Once all of the noise radar nodes have been weighted, they are vertically concatenated.

Figure 3.9 demonstrates the advantages provided by the JWM when compared to the image grid pixels. The black dots represent the center of the image pixels within the grid lines, which are representative of the image resolution that would be

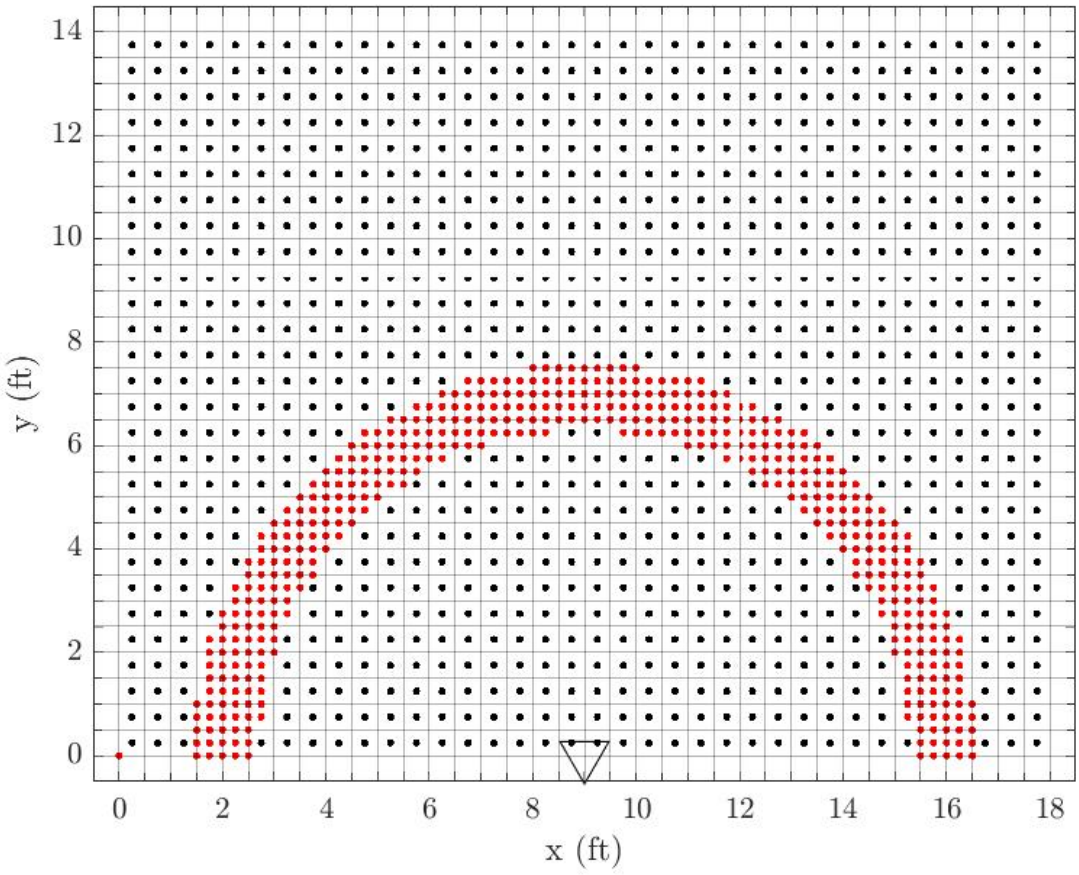

Figure 3.9: Center of image pixels with a single range ring within the JWM from the noise radar node at (9,0).

produced. The red dots signify a single range ring which can be weighted based on the JWM. The single red dot at (0,0) is a result of the noise radar node not utilizing artificial pixels which fall below $y = 0$ axis for each respective range ring. The finer resolution of the JWM allows for a more precise weighting when compared to the center of the image pixels. The range rings are able to form a more accurate ring shape than they would be able to if the centers of the image pixels were utilized. The increased artificial pixels within each image pixel are summed and then the weight matrix is normalized.

Figure 3.10 demonstrates the image weighting from a single noise radar for the

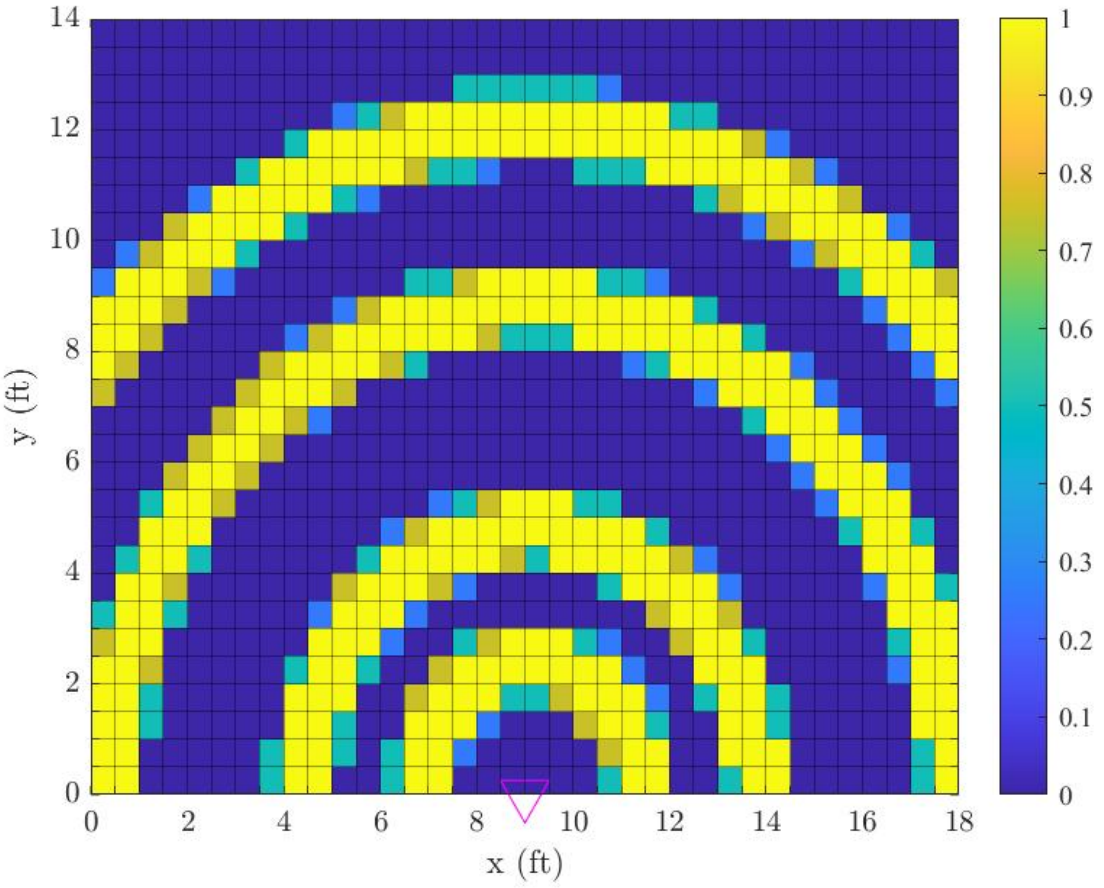

Figure 3.10: JWM showcasing four respective range rings with noise radar node at (9,0).

JWM with four arbitrary range rings selected to demonstrate the image weighting at four range indices. There are additional range rings covering 100% of the area of interest, but only four are shown here so that they can be distinguished in this visual example. The key observation is the variable weighting of the respective range rings. The higher intensity areas of the image are due to additional coverage of the artificial grid pixels, therefore increasing dependence of the radar return at the given range on these locations. The JWM can be utilized to emphasize desired characteristics and minimize noise and multipath interference. Custom weighting can be conducted in multiple facets with the JWM. Each NRN node's range rings can be selectively

weighted based on a multitude of desired effects such as distance from that node, in addition to selective weighting within the range ring. The JWM allows for additional weighting to be added to the respective range rings if desired, in addition to the default weighting of the range ring.

A modification of the JWM range ring weighting involves increasing the weight in the center of each respective range ring. Similar to calculating the ellipse width within RTI, if a range ring is too large it will bias unwanted data; however, if it is too small, it misses useful data. With this in mind, an addition is made to JWM to include focused weighting. Similar to Equation (61), an additional weighting is added to provide a focused weighting capability. With the modifications to the Equation (61), the new weighting becomes

$$w_{i,j}^{\mathrm{JWM,focus}} = \begin{cases} w_{i,j}^{\mathrm{JWM,focus}} + w_{i,m} + w_{i,m}^{\mathrm{focus}}, & \text{if } (\mathrm{x_j} - \mathrm{d} \leq \mathrm{RR_{m,i}^{x}} < \mathrm{x_j} + \mathrm{d}) \\ w_{i,j}^{\mathrm{JWM,focus}}, & \text{otherwise} \end{cases} \tag{65}$$

Index m loops from one to the number of artificial pixels for each pixel jth pixel. The focused artificial pixel weighting matrix is

$$w_{m,i}^{\mathrm{focus}} = \begin{cases} 1, & \text{if } r_{\mathrm{focus,inner},i}^2 \leq (x_m - h)^2 + (y_m - k)^2 < r_{\mathrm{focus,outer},i}^2 \\ 0, & \text{otherwise} \end{cases} \tag{66}$$

where

$$r_{\mathrm{focus,inner},i} = r_i - \frac{R_{\mathrm{res}}}{4} \tag{67}$$

where r_i is the ith range and R_{res} is the range resolution. The outer radius, $r_{outer,i}$, equals

$$r_{\mathrm{focus,outer},i} = r_i + \frac{R_{\mathrm{res}}}{4} \tag{68}$$

Equation (65) demonstrates the addition to the JWM notation which leads to additional weighting within the center of the range rings for the JWM focused weighting method. The value of the denominator for the inner and outer radius for this thesis was chosen to be four; however, within the code it can be selected by the user. With a smaller range ring created within the larger range ring, additional methods of weighting could be conducted.

Figure 3.11 demonstrates the result of increasing the interior of each respective range ring. The additional bias can provide increased attenuation image clarity due to mitigating the degree of overlap by each respective range ring.

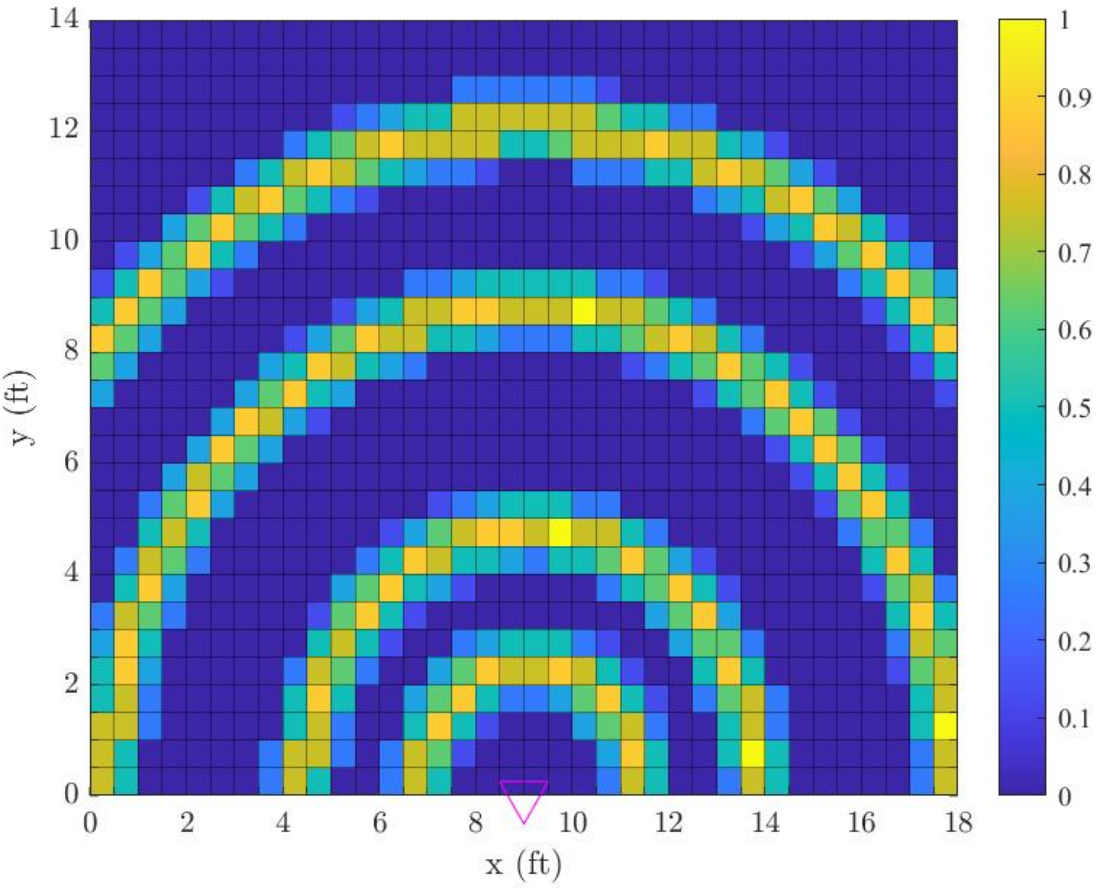

Figure 3.11: JWM with enhanced weighting of four respective range rings with the noise radar node at (9,0).

An additional method of weighting for the JWM is distance based weighting. Distance based weighting involves weighting the data based on its distance from the noise radar node. This weighting can be utilized to focus on targets which are closer to the noise radar node as well as targets that are farther away. This thesis focused on weighting closer targets higher than farther targets. Based on potential target scenarios, this could easily be modified. The first distance based weighting method is linear based weighting.

$$w_{i,j}^{\text{linear}} = \begin{cases} r_{max} - r_i, & \text{if } (\mathrm{x_j} - \mathrm{d} \leq \mathrm{RR_{m,i}^{x}} < \mathrm{x_j} + \mathrm{d}) \quad \& \quad (\mathrm{y_j} - \mathrm{d} \leq \mathrm{RR_{m,i}^{y}} < \mathrm{y_j} + \mathrm{d}) \\ w_{i,j}^{\text{linear}}, & \text{otherwise} \end{cases} \tag{69}$$

where r_i is the ith range, r_{max} is the maximum range index for the noise radar node. Index m loops from one to the number of artificial pixels for each pixel jth pixel. Equation (69) modifies the JWM by linearly weighting pixels. As distance from the noise radar increases, the overall weight is decreased. This method should be used when targets are anticipated to have a relative proximity to the noise radar node.

Figure 3.12 demonstrates the linear weighting decrease of the respective range rings as distance from the noise radar increases.

The second distance based weighting method utilized was exponential distance weighting. The exponential distance weighting heavily weights targets which are closer to the noise radar node.

$$w_{i,j}^{\text{exp}} = \begin{cases} e^{(-\frac{r_i}{2})}, & \text{if } (\mathrm{x_j} - \mathrm{d} \leq \mathrm{RR_{m,i}^{x}} < \mathrm{x_j} + \mathrm{d}) \quad \& \quad (\mathrm{y_j} - \mathrm{d} \leq \mathrm{RR_{m,i}^{y}} < \mathrm{y_j} + \mathrm{d}) \\ w_{i,m}^{\text{exp}}, & \text{otherwise} \end{cases} \tag{70}$$

Index m loops from one to the number of artificial pixels for each pixel jth pixel.

Figure 3.13 demonstrates the exponential weighting decrease of the respective

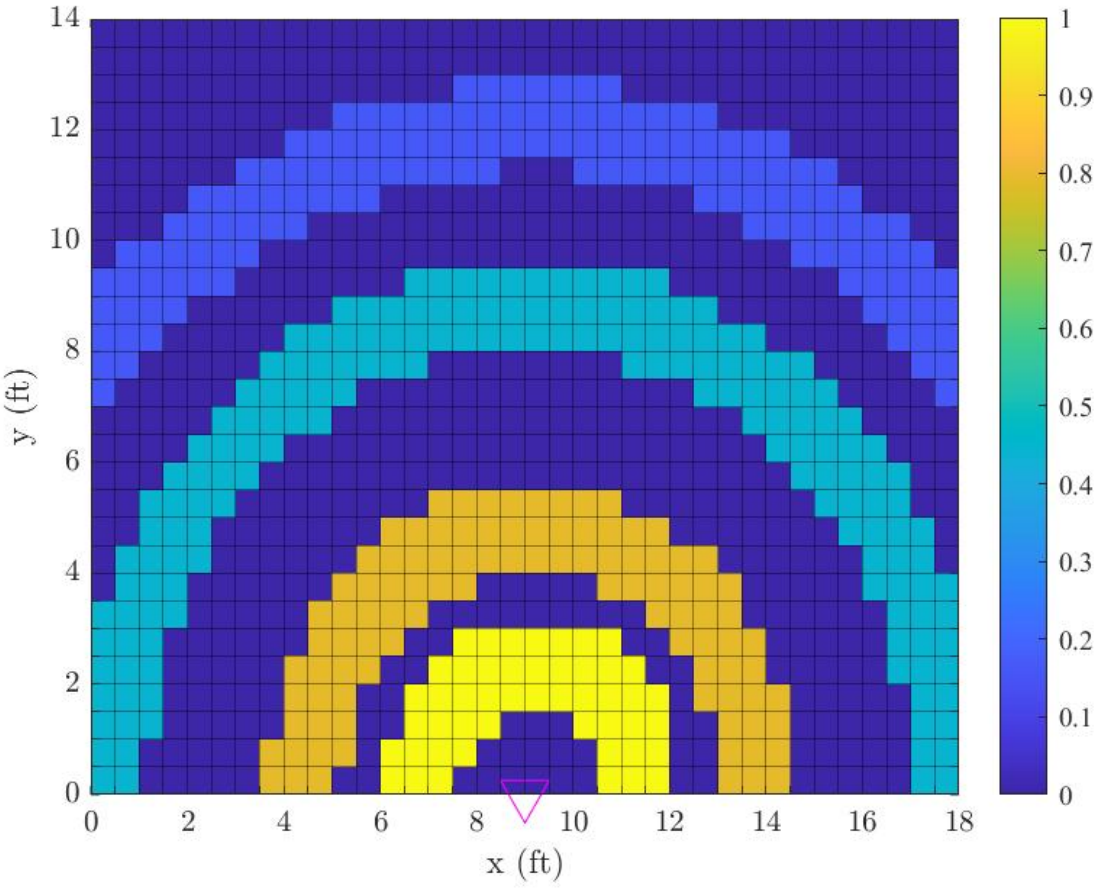

Figure 3.12: JWM with linear distance weighting showcasing four respective range rings with noise radar node at (9,0).

range rings as distance from the noise radar increases. This method would be most beneficial for targets which are within close proximity to the radar node.

Table 3.1 illustrates a summary of the primary options for NRN weighting which will be analyzed in this thesis. With the JWM, each of these weighting methods can be conducted with ease.

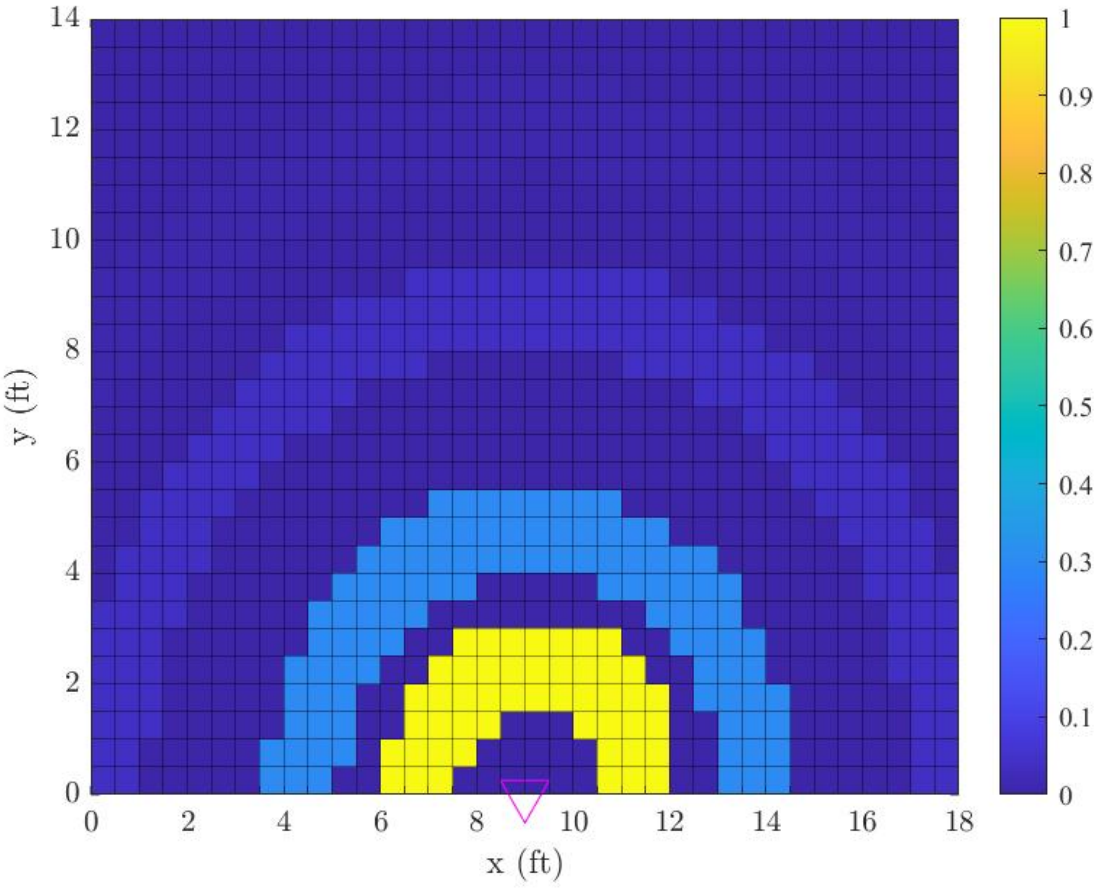

Figure 3.13: JWM with exponential distance weighting showcasing four respective range rings with noise radar node at (9,0).

Mode Number	Mode	Description
1	Original Weight Method	Trilateration with the center of the image pixels, weighted as a binary selection matrix
2	JWM	Artificial grid created to mimic weighting found in the RTI NeSh Model
3	JWM with Linear Distance Weighting	JWM with each respective range ring weighted at linearly decreasing rate based on distance
4	JWM with Exponential Distance Weighting	JWM with each respective range ring weighted at exponentially decreasing rate based on distance
5	JWM with $\frac{1}{4}$ Center Weighting	JWM with $\frac{1}{4}$ of the center of each range ring additionally weighted to mimic weighting found in the RTI Weighting-g model

Table 3.1: NRN weighting options.

3.7 Multi-Sensor Data Fusion

Disparate data sources provide sensing capabilities to certain situations where a single sensing source may struggle independently. Utilizing disparate data sources provides an additional level of information than can be found with a single source [32]. A challenge of utilizing disparate data sources is fusing the disparate data together. There are two forms of data fusion within the testbed created for this thesis: direct fusion of disparate data to create a single image, and creation of two images followed by fusion of the two images into one.

Vergara [24] utilized a few foundational methods of data fusion to create images composed of RTI and NRN data. Direct fusion of data allows for additional models and algorithms to be directly applied to the data, prior to formation of an image using desired reconstruction algorithms. The direct fusion of data is more challenging due to the disparate sensing systems utilized. To counter this, Vergara [24] proposed a tunable parameter, β, which is injected into the system model definition and shown in Equation (46). This method improves the combination of raw data in an attempt to mitigate the difference in the disparate units of RTI and NRN. Additionally, a Kalman filter was proposed and notionally utilized. These disparate fusion techniques improved performance with respect to separate image fusion utilized by Vergara [24]. To more quickly equate RTI research to NRN research, it was decided that each sensing system would be optimized and use separate image formation to fuse the data.

The second form of fusion is the fusion of separate images of RTI and NRN. This is the simplest form of data fusion between RTI and NRN. Forming separate images, then combining the respective images together negates the need to offset disparate units and sensing characteristics. This provides a simple solution; however, if a certain sensor system (RTI or NRN) struggled with detecting targets or mitigating

interference, the final formed image will directly contain these elements if additional fusion techniques are not applied. Four new methods are proposed to determine new methods of simple image fusion. These methods will be able to determine and adjust image fusion based on the target localization accuracy of RTI and NRN. This is beneficial if one of the sensing systems is creating more accurate attenuation images. The first form of fusion allows for an increased target localization accuracy when compared to the second form of fusion; however, the first form of fusion has an increased mathematical and processing complexity when compared to the second form of fusion due to the disparate units between RTI and NRN. The advantage of separate image fusion is that it doesn't require equating disparate units and separate processes for RTI and NRN can be independently applied. The options for separate image fusion are listed and summarized in Table 3.2.

Fusion Number	Mode	Description
1	Original Fusion Method	Separate images are added together and averaged
2	RTI Favored Fusion	The NRN image is weighted by a factor of $\frac{1}{2}$ compared to the RTI image
3	NRN Favored Fusion	The RTI image is weighted by a factor of $\frac{1}{2}$ compared to the NRN image
4	Grid Focused Image Fusion	The interior of the RTI image is weighted by a factor of $\frac{1}{2}$ and the exterior of the NRN image is weighted by a factor of $\frac{1}{2}$ creating a focus on the NRN data in the center and the RTI data in the exterior of the testing area
5	Grid Focused Image Fusion	The interior of the NRN image is weighted by a factor of $\frac{1}{2}$ and the exterior of the RTI image is weighted by a factor of $\frac{1}{2}$ creating a focus on the RTI data in the center and the NRN data in the exterior of the testing area

Table 3.2: Separate image fusion options.

3.8 Testbed Creation

To accomplish this thesis, it was necessary to create a simulation testbed to more accurately apply RTI research to NRN research. Without a universal testbed, gathering performance data on various weighting models, reconstruction algorithms, and target localization algorithms would be challenging.

Figure 3.14 demonstrates the system configuration of the RTI radio frequency (RF) transceivers and NRN nodes. The basis of the testbed is to take the system configuration shown and provide additional analysis and functionality for those to sensing systems. A testbed allows for previous and future research to be conducted

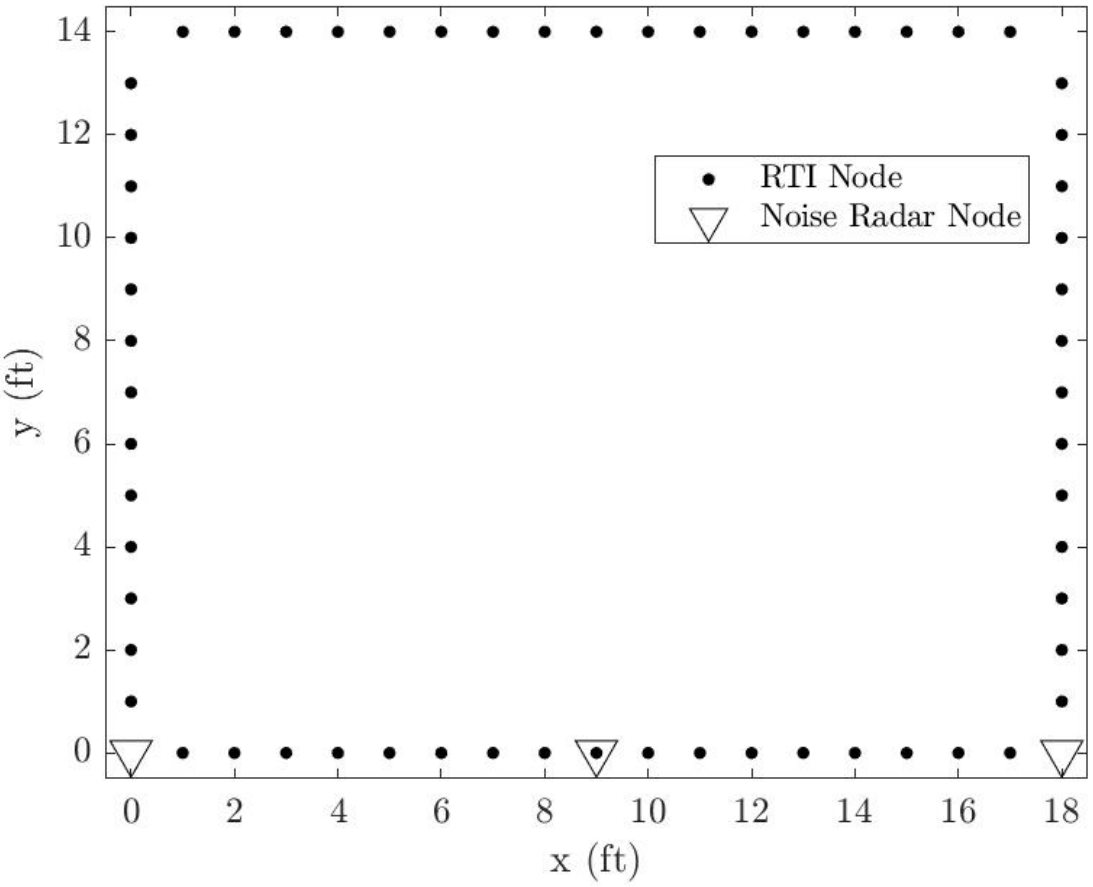

Figure 3.14: RTI and NRN node locations within the test environment.

and analyzed in a single location. Following previous research, simulations and results will be conducted within the testbed in MATLAB. Experimental data can be inputted into the testbed for either RTI or NRN. It is preferable to have experimental data for both sensing systems for a more equivalent comparison; however, that is not required. The experimental data utilized within this thesis was previously collected by Vergara [24]. Previous work by Battle [2] yielded a wide range of RTI data for single and multi-target scenarios. The data used by Battle [2] was utilized to test the ability of the testbed to accept different data sets; however, could not be utilized due to no matching NRN data sets available. The data sets primarily used for this thesis were a result of Vergara [24] since matching RTI and NRN target scenarios were used.

3.8.1 Previous Code Contributions

Vergara [24] created a proof of concept that a testbed could be created. This proof of concept notionally fused RTI and NRN data to improve DFL capabilities of two disparate sensing technologies. The theoretical derivation to experimental testing provided strong interest in creating a testbed to study additional methods of utilizing NRN. Vergara [24] utilized the AFIT NoNET and RTI network to gather experimental data sets within the same environment and with the same target locations. The provided experimental data is used to verify the testbed is operational and that improvements to weight models and data fusion are produced. Based on experimental data, the NRN portion of the testbed has a simulated data capability in order to utilize experimental RTI data when equivalent NRN is not available.

Battle [2] focused on RTI weight model research. The fundamentals of this research are applied to NRN in this thesis. The ability of switching weight models and reconstruction methods within RTI was highly desired in creation of the testbed. There were a number of weight models and reconstruction methods which had been

optimized that were also beneficial to ensuring the proper operation of the testbed. RTI datasets with various target positions and numbers improved on RTI datasets provided by Vergara [24]. The improved RTI data allowed for increased resolution of fused attenuation images when NRN weighting improvements were made.

Previous code did not provide a few main capabilities which the testbed aims at achieving. The first deficiency is the lack of a universal data input. Previous data was hard coded and various points of the simulation would have to be readjusted based on data length and data specifications. In order to conduct additional experimental results, it was necessary to utilize the same experimental setup, to include network dimensions. The rigidity doesn't allow to easily change the dimensions of the area of interest or the image resolution. A second deficiency is the lack of customizable options in adjustment of various parameters for both the RTI and NRN sides. There are variables which were hard coded and unable to change, limiting the resulting scenarios which could be tested. For both RTI and NRN, it is necessary to have a wide range of easily changed variables to be operational, to include image resolution. Image resolution errors would occur due to hard coding and inability to change tuning variables with ease.

A key parameter, the smoothing term α, was arbitrarily chosen by Vergara [24] based on aesthetics for the proof of concept testbed. Battle [2] created individualized tests based on target scenario and data sets. In order to have a fully optimized testbed, it will be necessary to have the ability to quickly optimize α in order to produce optimal results with ease.

3.8.2 Proposed Simulation Testbed

The testbed for research and data fusion between RTI and NRN is proposed in order to build from prior research in RTI and NRN and provide a platform for further

research to be conducted. The primary goal of the testbed is to create a universal tool that can provide flexible additions of weight models, reconstruction algorithms, and target localization. The testbed will operate in four stages to accomplish this goal.

The first stage will involve data input and selection of parameters. The primary choice will be if the user wants to leverage experimental data or simulated data. The current proposed testbed can utilize experimental RTI and NRN data, as well as simulate NRN data. The ability to simulate RTI data can be built in with ease but is not currently available. Simulated data for NRN is able to be utilized when experimental data is not present. Experimental RTI data can be combined with simulated NRN data or vice versa. Once the data source is chosen, various parameters are adjusted based on input data. Parameters such as test environment dimensions, sensor nodes, noise radar nodes, and radar characteristics are the primary changes. From here, the user has the ability to change or modify these parameters if desired. As long as the user is inputting data which contains the same target environment, a multitude of various sensing systems data streams can be analyzed. The limiting factor currently is the RTI network setup, due to it having fixed dimensions for its WSN RF transceivers.

The second stage involves data processing and image reconstruction. This stage is where the primary weighting and image reconstruction is conducted. The user has the ability to select the desired weighting models for RTI and NRN. For RTI, the ability to select a method for image reconstruction is also available. The testbed allows for a simplified inclusion and method of selection for weighting and reconstruction methods. With relative ease, a new method can be inputted and tested with the testbed, alongside previously researched methods. Data fusion directly conducted on the raw data and data fusion conducted with separate images is also conducted here.

The output of this stage is a set of images with the user selected parameters for RTI, NRN, and a fused image.

The third stage involves target detection and localization based on the formed images from the second stage. Based on the images formed in stage two, the images are analyzed to detect locations of potential targets.

The fourth stage involves measuring performance metrics on the various methods utilized within the testbed. The current setup includes the ability to track individual RTI and NRN performance, as well as images which have utilized data fusion or image fusion between them. Performance metrics are utilized to compare various parameter selections, weight models, and data fusion techniques.

The testbed provides current and future research capabilities. An additional capability the testbed provides is the ability to optimize certain parameters, such as smoothing terms for RTI, NRN, and fusion images. This allows for an increase in target localization accuracy and overall performance. The testbed has been set up to allow the inclusion of additional sources of sensor data. This includes additional noise radar nodes, additional WSN configurations separate from the current system, and additional sensors not previously utilized in RTI and NRN research.

IV. Results and Analysis

The simulation testbed provides a wide range of capabilities; the primary benefit is the ability to gather a wide range of results with ease. This thesis was focused on the creation of the simulation testbed in order to further research with NRN. This chapter will discuss and analyze attenuation images of RTI, NRN, and fusion images to demonstrate testbed operation and research conducted within NRN.

4.1 Noise Radar Weight Matrix Results

The testbed provides the ability to focus on RTI, NRN, or fusion images. This section will focus on the research conducted within NRN. From the RTI and NRN data provided by Vergara [24], there are three target scenarios. Each target scenario contains a single target in one of three respective locations. Attenuation images for each of the target locations are provided for each of the respective weighting methods utilized. Additionally, the true target attenuation image based on the target model is provided for reference. The five weighting methods are listed below:

- NRN Method 1: Binary Selection Matrix
- NRN Method 2: Jans Weighting Method
- NRN Method 3: Jans Weighting Method with Linear Distance Weighting
- NRN Method 4: Jans Weighting Method with Exponential Distance Weighting
- NRN Method 5: Jans Weighting Method with Focused Weighting

These five NRN weighting methods were chosen to analyze and highlight various aspects and capabilities of the JWM. The various weight models can be used based

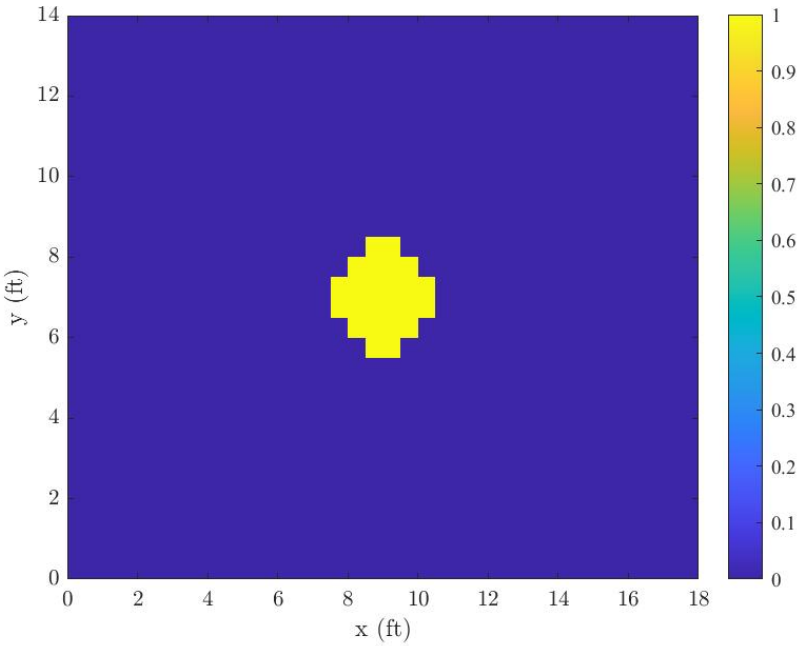

Figure 4.1: Ideal attenuation image for target location (9,7).

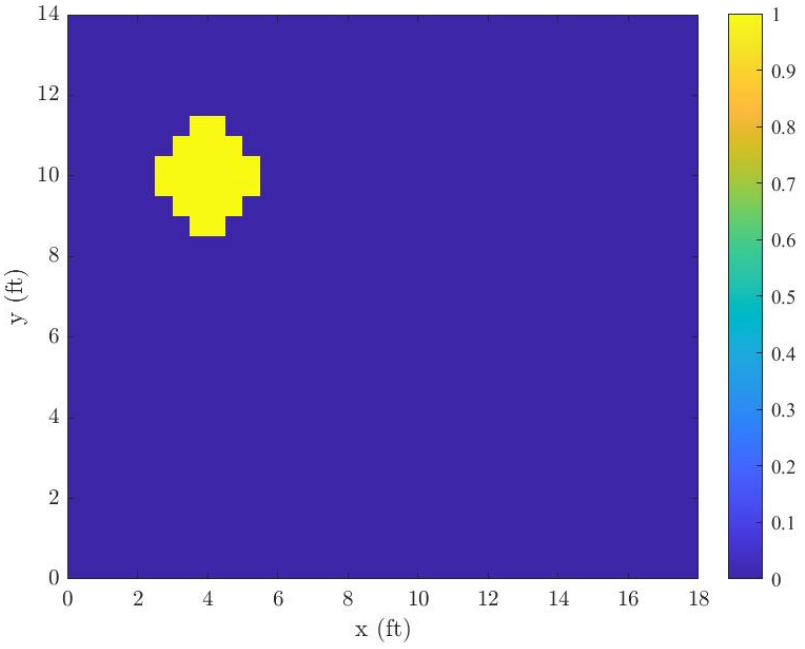

Figure 4.2: Ideal attenuation image for target location (4,10).

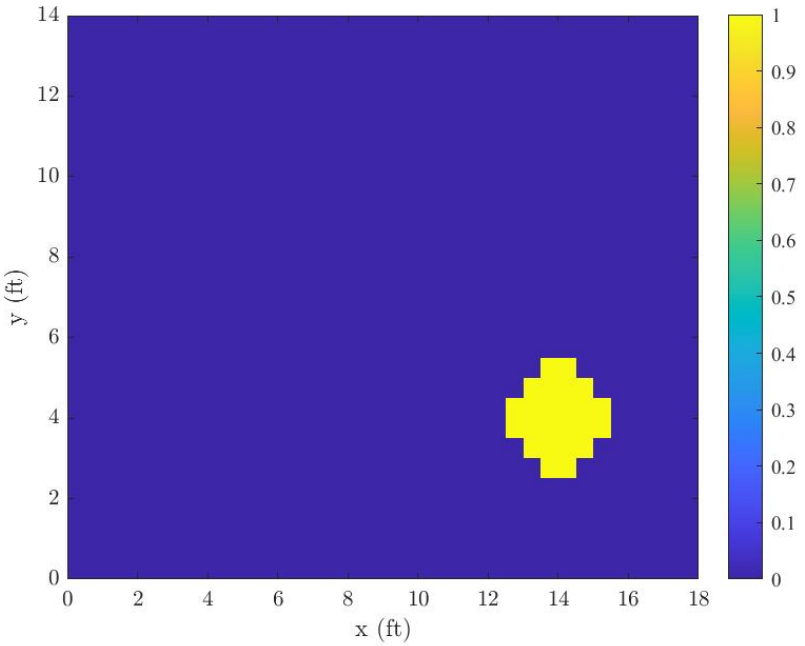

Figure 4.3: Ideal attenuation image for target location (14,4).

on the user's desired target scenario and environment. Various target models can be utilized and modeled within the testbed.

Figure 4.1, Figure 4.2, and Figure 4.3 show the ideal attenuation images for the three target scenarios. The ideal reference attenuation images based on the target model and target locations are provided for reference. The true target attenuation images provide a basis for determining the accuracy of the weighting models and image fusion methods within the testbed. The center of the true attenuation image is considered the true target location. When comparing estimated images to the ideal images, the Tikhonov reconstruction method will be used unless stated otherwise.

4.1.1 NRN Method 1: Binary Selection Matrix

The binary selection matrix is the NRN weighting method previously used in research due to its simple application and ease of use. The center of the image pixels are weighted if they fall within the respective range ring of the noise radar node. Pixels which fall outside of the respective range ring are weighted zero. Three target scenarios are tested to gather a baseline performance. The attenuation images are shown with the true target location, the K-means clustering centroid, and the MAP estimate. These metrics provide the ability to visually inspect the performance of the weighting method, as well as calculate the difference in true target location versus estimated target location.

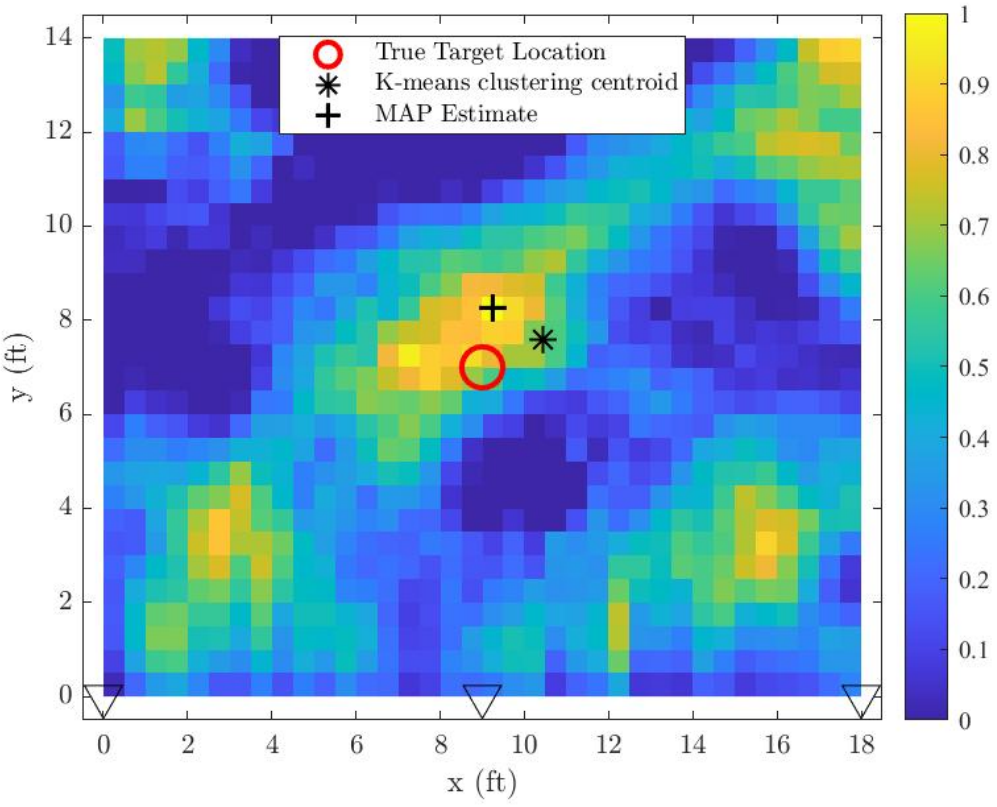

Figure 4.4: Method 1 attenuation image for target location (9,7).

Figure 4.4 displays the first target scenario where the target is located at (9,7). Noise and artifacts are present within the attenuation image; however, both target estimates are localized around the true target location.

Figure 4.5 displays the second target scenario where the target is located at (4,10). The overall intensity of the attenuation image is low, which results in both target estimates not localizing around the true target location. The expectation is that targets would be more prominent when the image contains low levels of noise. The highest intensity pixel with the image is located in the top right corner, therefore, the binary selection matrix performance is poor for this target scenario because the pixel with the highest intensity is not localized around the target location.

Figure 4.6 displays the third target scenario where the target is located at (14,4).

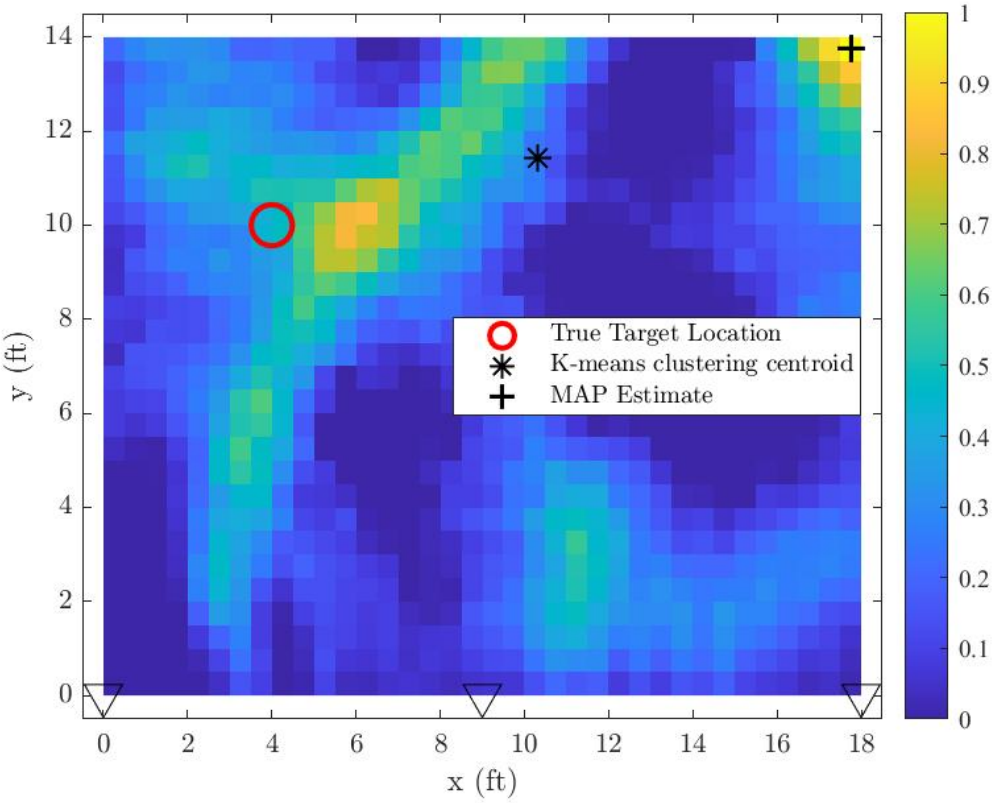

Figure 4.5: Method 1 attenuation image for target location (4,10).

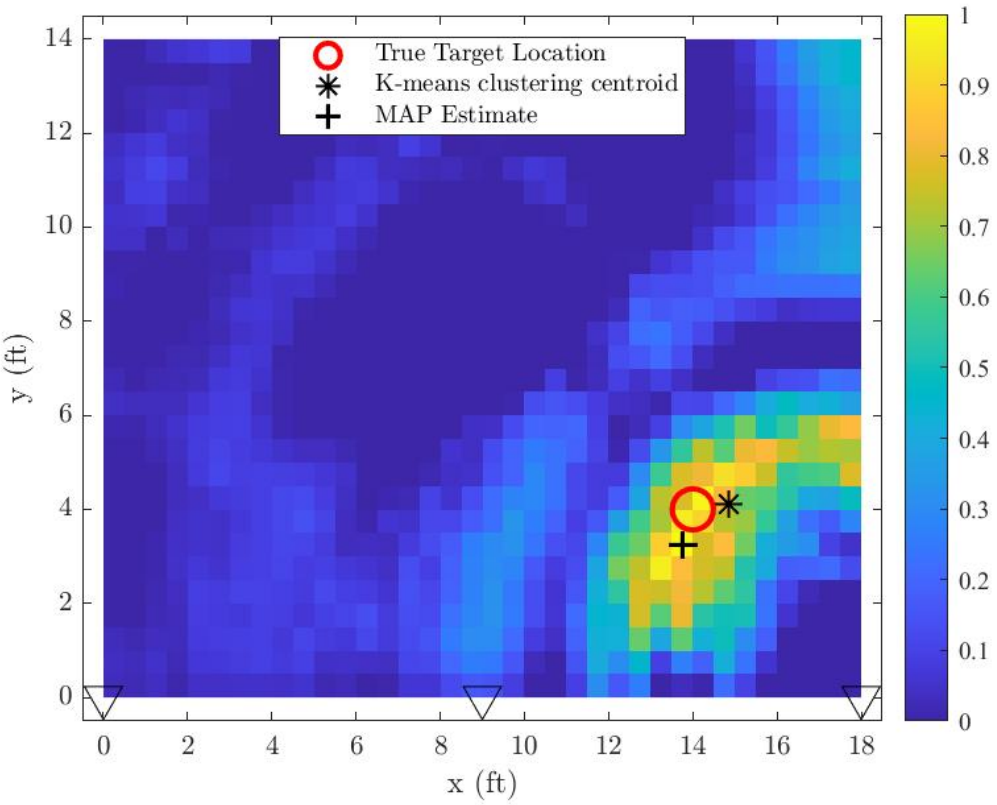

Figure 4.6: Method 1 attenuation image for target location (14,4).

Noise and artifacts are contained around the true target location, however, the target estimates are also localized withing this area. Due to the noise radar nodes being setup along the $y = 0$ axis, the target is resolved more clearly due to proximity to the nodes. The attenuation image also demonstrates that the data from the third noise radar node, located at (18,0), provided a higher share of the true data for trilateration. This observation is noted due to the appearance of slight range rings originating from the noise radar node located at (18,0), and appearing within the attenuation image.

Table 4.1 shows the performance metric results for NRN weighting method one. The binary selection matrix weighting performed well in two of the three target scenarios. The (4,10) target scenario suffered drastically, with the MAP estimate localizing the target to the top right corner of the image. The binary selection matrix is a viable

Table 4.1: Performance metrics for NRN weight method 1 for targets at (9,7), (4,10), and (14,4).

Target Location	**Performance Metric**	**Description**	**Result**
(9,7)	K-means clustering	Coordinates of the centroid	(10.20,7.35) $\epsilon_{Centroid} = 1.25$ ft
	MAP Estimate	Coordinates of the highest intensity pixel	(9.25,8.25) $\epsilon_{MAP} = 1.2748$ ft
	MSE	mean square error between the true target image and the attenuation image	$MSE = 0.0895$
	RMSE	root mean square error between true target location and centroid location	$RMSE = 0.8867$
	Dispersion Error	Pixel spread about the centroid	$\epsilon_{Dispersion} = 5.178$ ft
(4,10)	K-means clustering	Coordinates of the centroid	(10.07,11.19) $\epsilon_{Centroid} = 6.19$ ft
	MAP Estimate	Coordinates of the highest intensity pixel	(17.75,13.75) $\epsilon_{MAP} = 14.25$ ft
	MSE	mean square error between the true target image and the attenuation image	$MSE = 0.0398$
	RMSE	root mean square error between true target location and centroid location	$RMSE = 4.3765$
	Dispersion Error	Pixel spread about the centroid	$\epsilon_{Dispersion} = 4.8186$ ft
(14,4)	K-means clustering	Coordinates of the centroid	(14.60,3.86) $\epsilon_{Centroid} = 0.6179$ ft
	MAP Estimate	Coordinates of the highest intensity pixel	(13.75,3.25) $\epsilon_{MAP} = 0.7906$ ft
	MSE	mean square error between the true target image and the attenuation image	$MSE = 0.0212$
	RMSE	root mean square error between true target location and centroid location	$RMSE = 0.4369$
	Dispersion Error	Pixel spread about the centroid	$\epsilon_{Dispersion} = 0.8416$ ft

option for NRN weighting, however, it suffers when one or more of the noise radar node's target data suffers from increased attenuation and noise from the environment.

4.1.2 NRN Method 2: Jans Weighting Method

The JWM is utilized for NRN weighting method two. The JWM utilizes an artificial pixel grid at a finer resolution than the image to apply a more accurate weighting to the respective range rings of each noise radar. The attenuation images are shown with the true target location, the K-means clustering centroid, and the MAP estimate. These metrics provide the ability to visually inspect the performance of the weighting method, as well as calculate the difference in true target location versus estimated target location.

Figure 4.7 displays the first target scenario where the target is located at (9,7). Noise and artifacts are present within the image, however both target estimates are

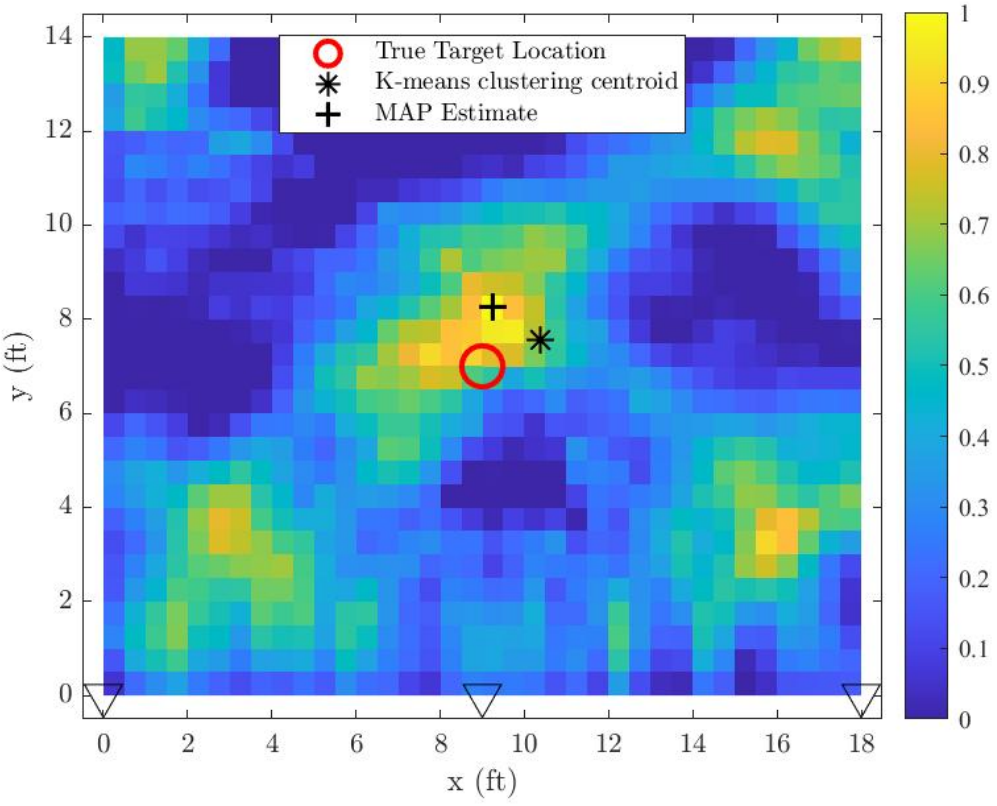

Figure 4.7: Method 2 attenuation image for target location (9,7).

localized around the true target location in the center of the image. The noise present is a constructive combination of noise resulting from the trilateration nature of the NRN. The constructive noise commonly occurs when a target is located centrally within the test environment.

Figure 4.8 displays the second target scenario where the target is located at (4,10). The k-means centroid has a farther proximity to the true target than the MAP estimate. A local intensity peak in the top right corner has the potential to become a global peak, which would drastically reduce overall detection accuracy.

Figure 4.9 displays the third target scenario where the target is located at (14,4). Noise and artifacts are present within the image, however both target estimates are localized effectively around the true target location. This attenuation image has

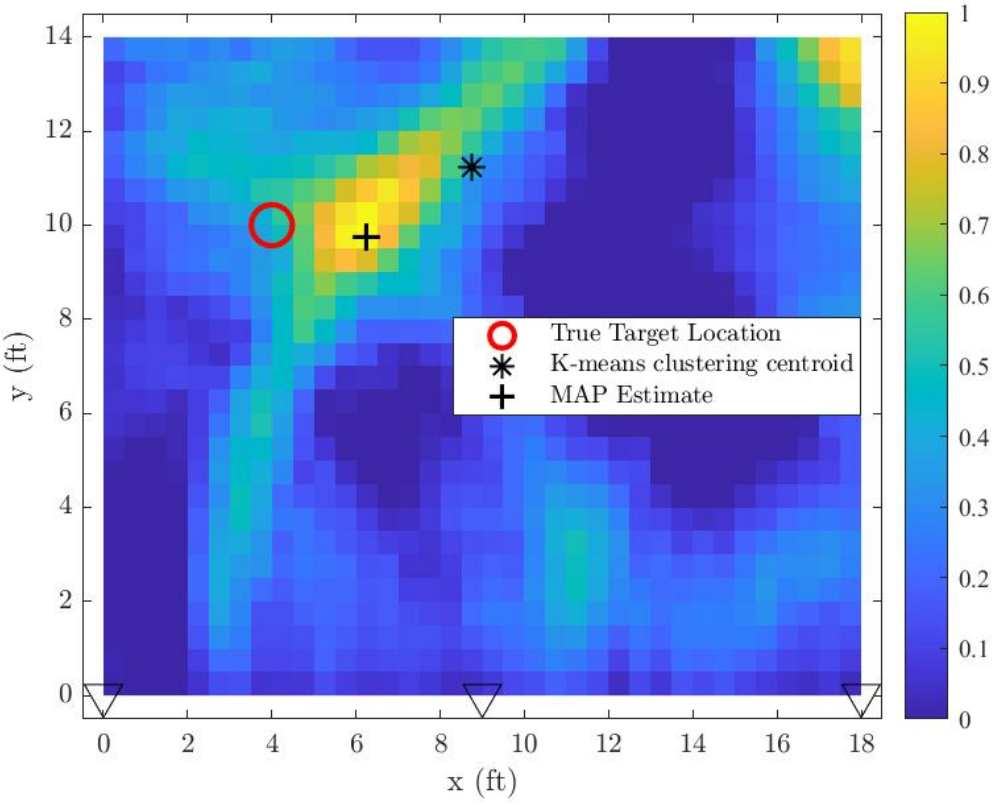

Figure 4.8: Method 2 attenuation image for target location (4,10).

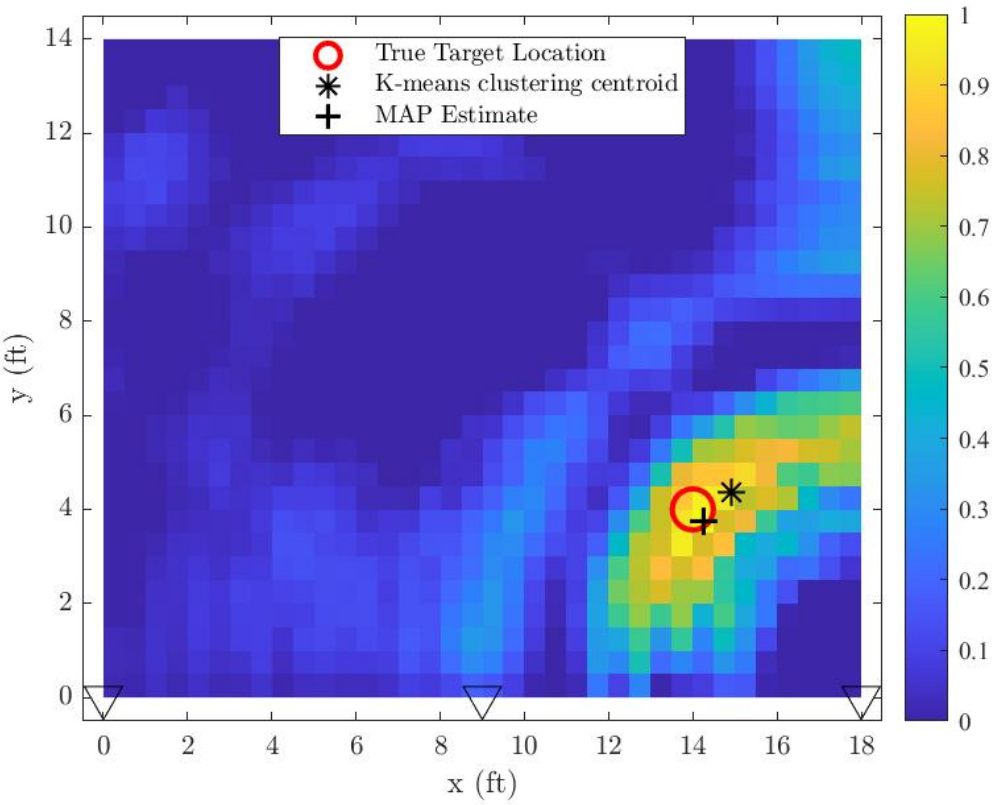

Figure 4.9: Method 2 attenuation image for target location (14,4).

decreased noise overall, allowing for a more accurate estimated target location. This is a result of the proximity of the true target to the noise radars located on the $y = 0$ ft axis.

Table 4.2 hows the performance metric results for NRN weighting method two. The JWM in all three target scenarios. The second target scenario had the least accurate target localization; however, when compared to NRN weight method 1, there was a significant improvement in localization accuracy. This is to be expected due to the JWM increasing the resolution of the respective range rings while maintaining the same image resolution. Targets which are farther away from the noise radar nodes have larger errors based on the true location; however, the JWM was able to compensate.

Table 4.2: Performance metrics for NRN weight method 2 for targets at (9,7), (4,10), and (14,4).

Target Location	**Performance Metric**	**Description**	**Result**
(9,7)	K-means clustering	Coordinates of the centroid	(10.12,7.31) $\epsilon_{Centroid} = 1.16$ ft
	MAP Estimate	Coordinates of the highest intensity pixel	(9.25,8.25) $\epsilon_{MAP} = 1.2748$ ft
	MSE	mean square error between the true target image and the attenuation image	$MSE = 0.0806$
	RMSE	root mean square error between true target location and centroid location	$RMSE = 0.8228$
	Dispersion Error	Pixel spread about the centroid	$\epsilon_{Dispersion} = 4.055$ ft
(4,10)	K-means clustering	Coordinates of the centroid	(8.49,10.97) $\epsilon_{Centroid} = 4.595$ ft
	MAP Estimate	Coordinates of the highest intensity pixel	(6.25,9.75) $\epsilon_{MAP} = 2.2638$ ft
	MSE	mean square error between the true target image and the attenuation image	$MSE = 0.0467$
	RMSE	root mean square error between true target location and centroid location	$RMSE = 3.249$
	Dispersion Error	Pixel spread about the centroid	$\epsilon_{Dispersion} = 3.6192$ ft
(14,4)	K-means clustering	Coordinates of the centroid	(14.67,4.10) $\epsilon_{Centroid} = 0.68$ ft
	MAP Estimate	Coordinates of the highest intensity pixel	(14.25,3.75) $\epsilon_{MAP} = 0.3536$ ft
	MSE	mean square error between the true target image and the attenuation image	$MSE = 0.0211$
	RMSE	root mean square error between true target location and centroid location	$RMSE = 0.4784$
	Dispersion Error	Pixel spread about the centroid	$\epsilon_{Dispersion} = 0.6231$ ft

4.1.3 NRN Method 3: Jans Weighting Method with Linear Distance Weighting

NRN weighting method three utilizes the JWM and applies a linear distance weighting to each respective range ring based on its distance from the noise radar node. The farther in the test environment that a range ring is, the lower its overall weighting is. This creates a weighting method which favors targets which are close to the noise radar nodes. The attenuation images are shown with the true target location, the K-means clustering centroid, and the MAP estimate. These metrics provide the ability to visually inspect the performance of the weighting method, as well as calculate the difference in true target location versus estimated target location.

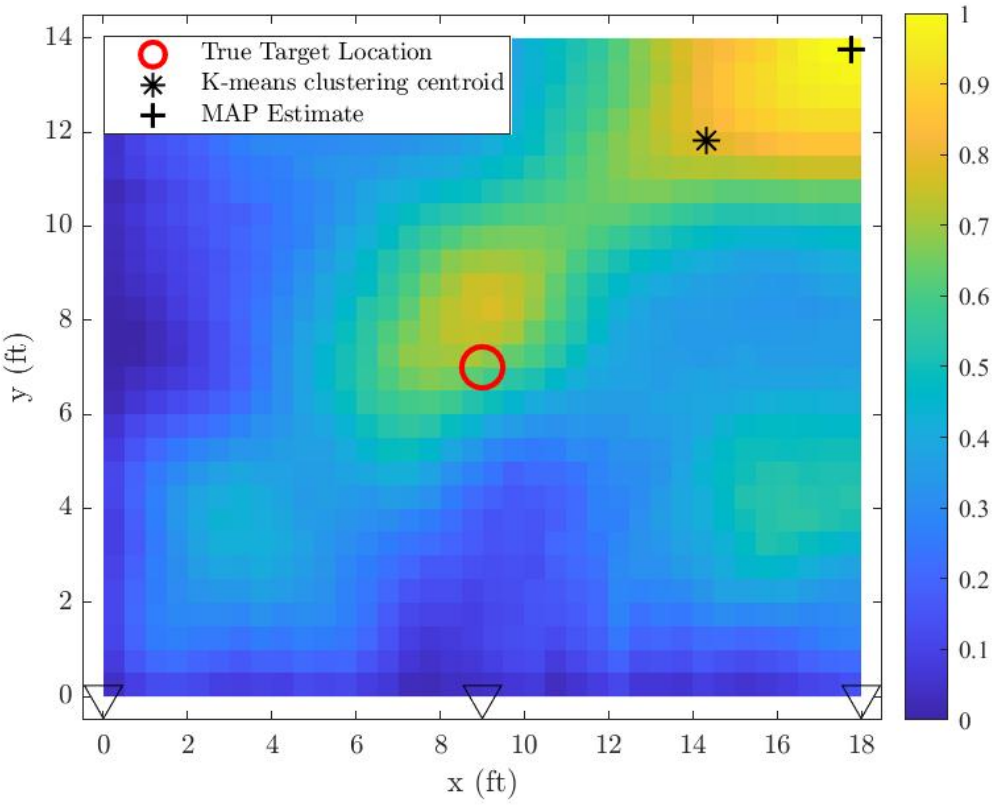

Figure 4.10: Method 3 attenuation image for target location (9,7).

Figure 4.10 displays the first target scenario where the target is located at (9,7). Overall noise within the image is low; however, the target localization suffers greatly due to global intensity peaks caused by interference in the top right corner of the attenuation image. This inaccuracy leads to significant errors within the localization of targets. Additionally, due to the weighting method, this image has a smoother appearance, similar to when the α_{NRN} term is not optimally set. This could be a result of the linear distance weighting not allowing for a significant portion of the data being weighted where the true target is located.

Figure 4.11 displays the second target scenario where the target is located at (4,10). The target is inaccurately localized; however, this weighting method greatly improves localization when compared to weighting method one. The overall image

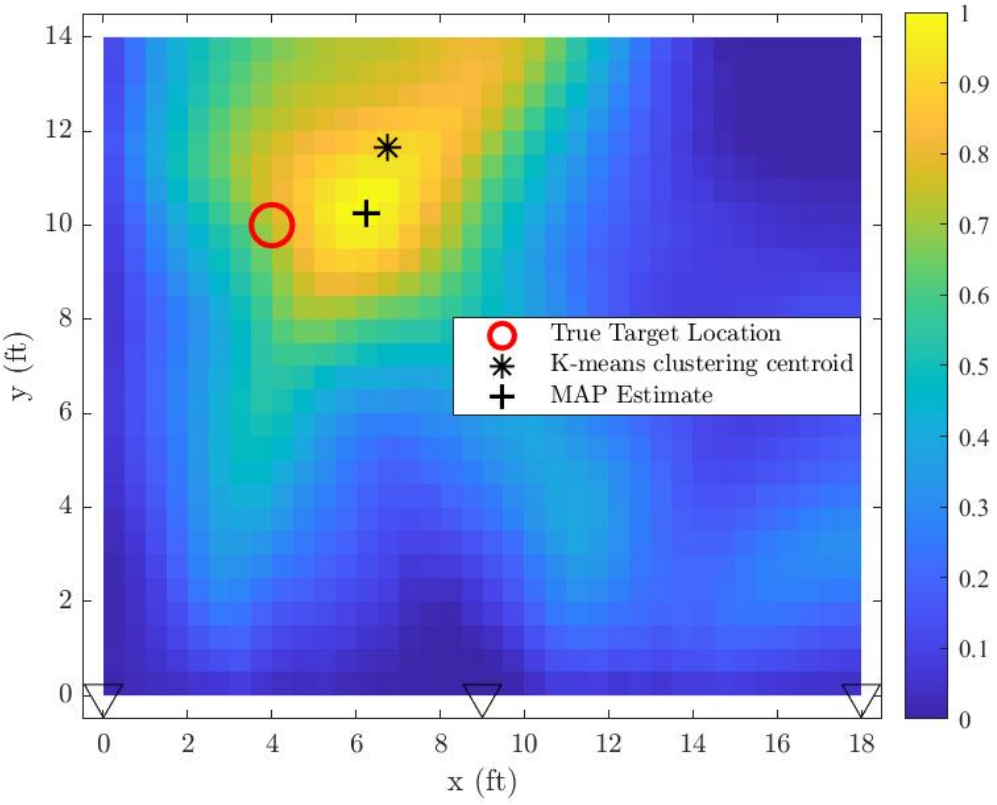

Figure 4.11: Method 3 attenuation image for target location (4,10).

appears to have a smoother appearance, similar to Figure 4.10. This target scenario contains the target which is farthest away from the noise radar nodes; however, target localization does not suffer significantly due to this.

Figure 4.12 displays the third target scenario where the target is located at (4,10). The target is localized as expected for this scenario. The linear distance weighting which this method provides is strongly emphasized for targets which are close to the noise radar nodes. The overall image appears to have a smoother appearance, similar to Figure 4.10 and Figure 4.11.

Table 4.3 shows the performance metric results for NRN weighting method three. The linear distance weighting performed well in two of the three target scenarios. A key observation from this weighting method is that it provides additional smoothing

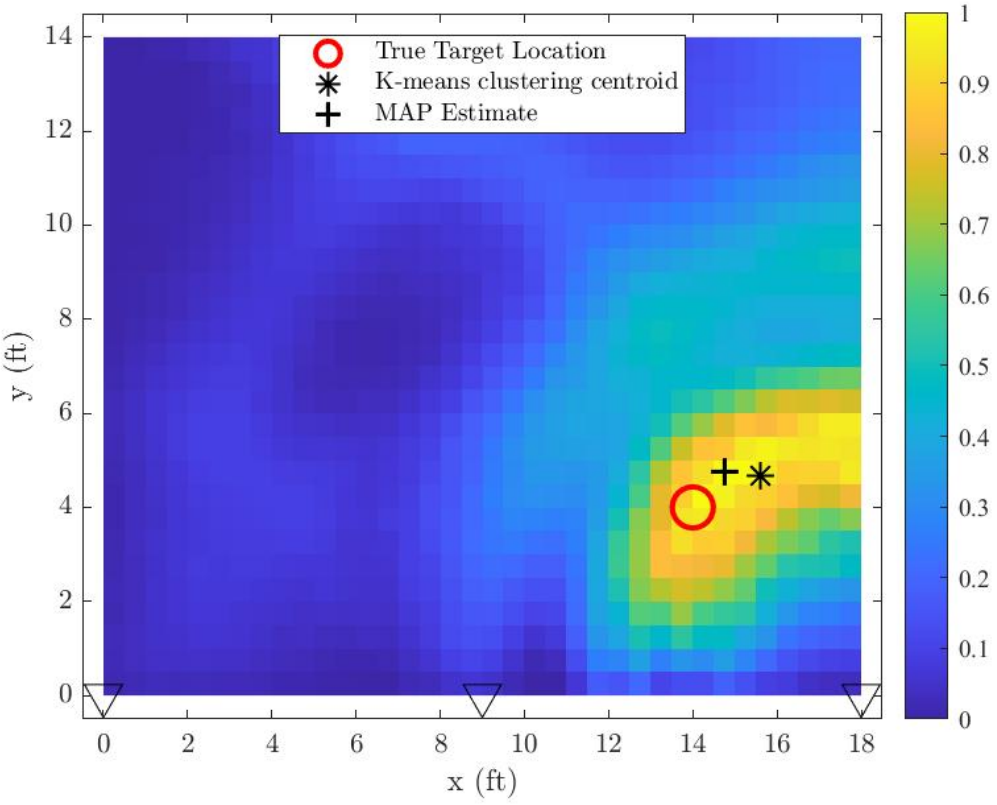

Figure 4.12: Method 3 attenuation image for target location (14,4).

Table 4.3: Performance metrics for NRN weight method 3 for targets at (9,7), (4,10), and (14,4).

Target Location	**Performance Metric**	**Description**	**Result**
(9,7)	K-means clustering	Coordinates of the centroid	(14.06,11.57) $\epsilon_{Centroid} = 6.82$ ft
	MAP Estimate	Coordinates of the highest intensity pixel	(17.75,13.75) $\epsilon_{MAP} = 11.05$ ft
	MSE	mean square error between the true target image and the attenuation image	$MSE = 0.1459$
	RMSE	root mean square error between true target location and centroid location	$RMSE = 4.8236$
	Dispersion Error	Pixel spread about the centroid	$\epsilon_{Dispersion} = 2.48$ ft
(4,10)	K-means clustering	Coordinates of the centroid	(6.49,11.40) $\epsilon_{Centroid} = 2.862$ ft
	MAP Estimate	Coordinates of the highest intensity pixel	(6.25,10.25) $\epsilon_{MAP} = 2.26$ ft
	MSE	mean square error between the true target image and the attenuation image	$MSE = 0.1197$
	RMSE	root mean square error between true target location and centroid location	$RMSE = 2.0196$
	Dispersion Error	Pixel spread about the centroid	$\epsilon_{Dispersion} = 1.2358$ ft
(14,4)	K-means clustering	Coordinates of the centroid	(15.35,4.44) $\epsilon_{Centroid} = 1.42$ ft
	MAP Estimate	Coordinates of the highest intensity pixel	(14.75,4.75) $\epsilon_{MAP} = 1.06$ ft
	MSE	mean square error between the true target image and the attenuation image	$MSE = 0.0679$
	RMSE	root mean square error between true target location and centroid location	$RMSE = 1.0063$
	Dispersion Error	Pixel spread about the centroid	$\epsilon_{Dispersion} = 0.7667$ ft

of the attenuation image. Due to this smoothing, it might be necessary to decrease the α_{NRN} term to increase target localization accuracy.

4.1.4 NRN Method 4: Jans Weighting Method with Exponential Distance Weighting

NRN weighting method four utilizes the JWM and applies an exponential distance weighting to each respective range ring based on its distance from the noise radar node. The farther in the test environment that a range ring is, the lower its overall weighting is. This weighting method strongly favors targets which are in close proximity to the noise radar nodes. The attenuation images are shown with the true target location, the K-means clustering centroid, and the MAP estimate. These metrics provide the ability to visually inspect the performance of the weighting method, as well as calculate the difference in true target location versus estimated target location.

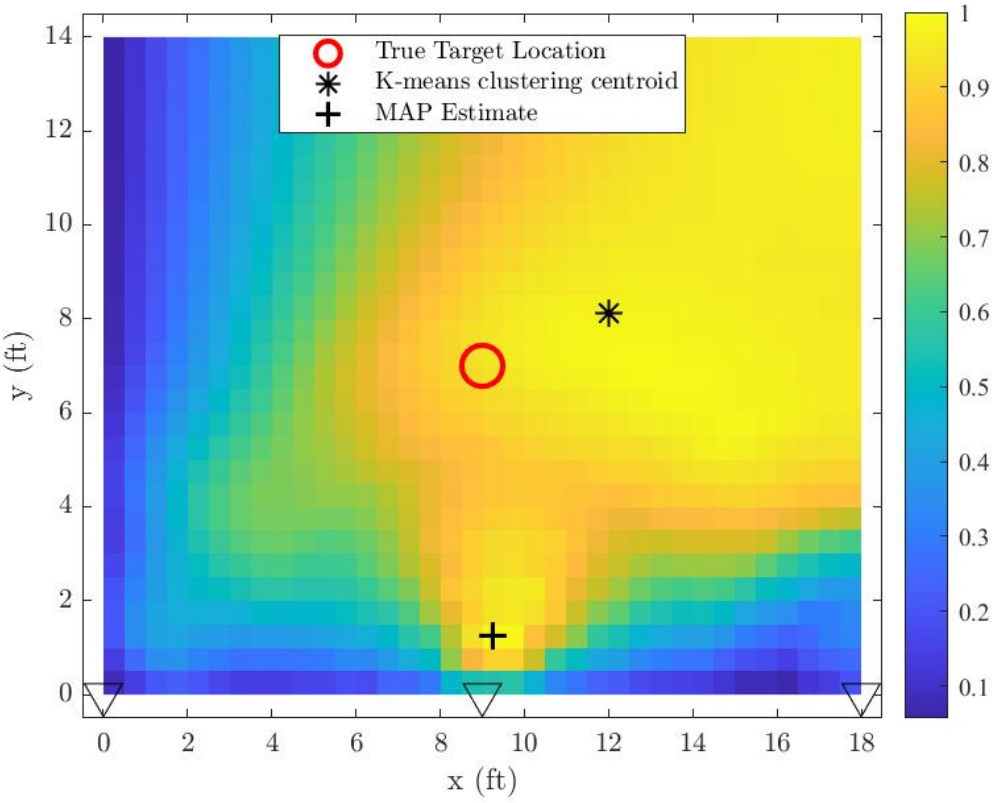

Figure 4.13: Method 4 attenuation image for target location (9,7).

Figure 4.13 displays the first target scenario where the target is located at (9,7). Noise and artifacts are present within the image, causing significant inaccuracies in target localization. The weighting method for this target scenario struggles due to an overemphasis on distances which are closer to the noise radar. This is evident due to the estimated target location based on the MAP estimate. Additionally, there are significant smoothing effects which have detrimentally affected the attenuation image.

Figure 4.14 displays the second target scenario where the target is located at (4,10). The weighting method provides a strong distance attenuation weighting as intended, which is detrimental due to this target scenario being the farthest way from the noise radar nodes. The overall attenuation in the image appears to have been

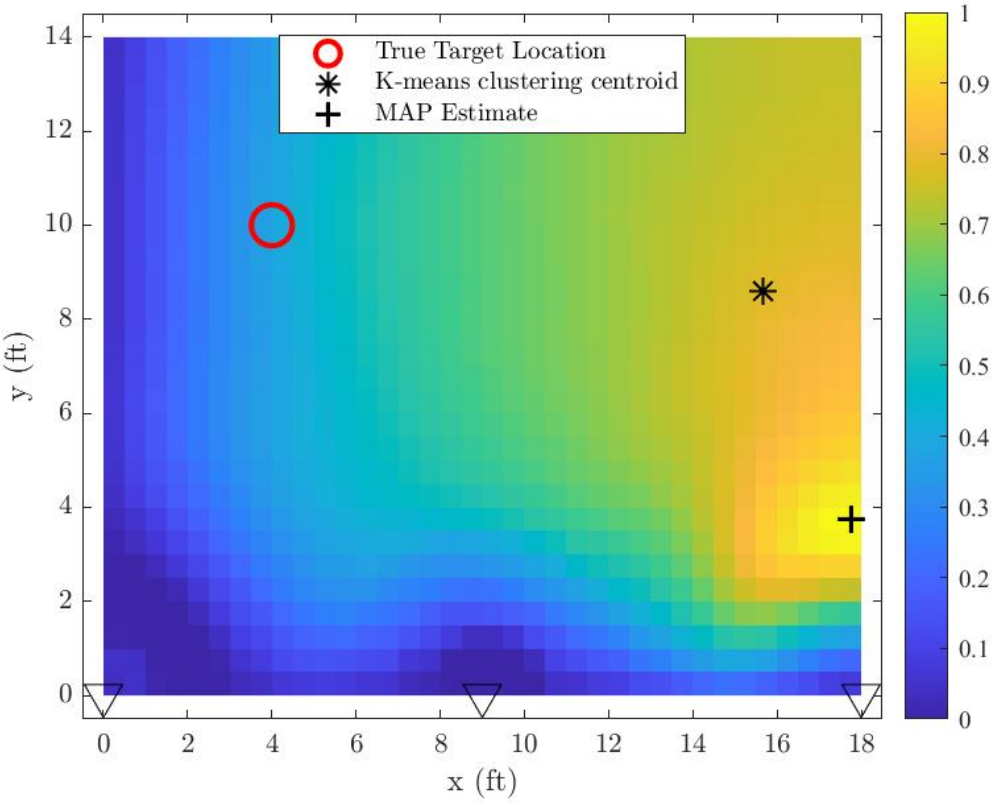

Figure 4.14: Method 4 attenuation image for target location (4,10).

smoothed in the image, reducing peaks but at the cost of target localization.

Figure 4.15 displays the third target scenario where the target is located at (14,4). This target scenario benefited from the weighting method, which is to be expected due to its proximity. The expectation was that this target scenario would be able to resolve an accurate target location estimate, however, this did not happen. The overall attenuation in the image appears to have been smoothed in the image, reducing peaks but at the cost of target localization.

Table 4.4 shows the performance metric results for NRN weighting method four. The exponential distance weighting did not perform as intended. There was not a significant performance increase from the weighting method one. Overall performance compared to other weighting methods is worse overall, with the best target scenario of

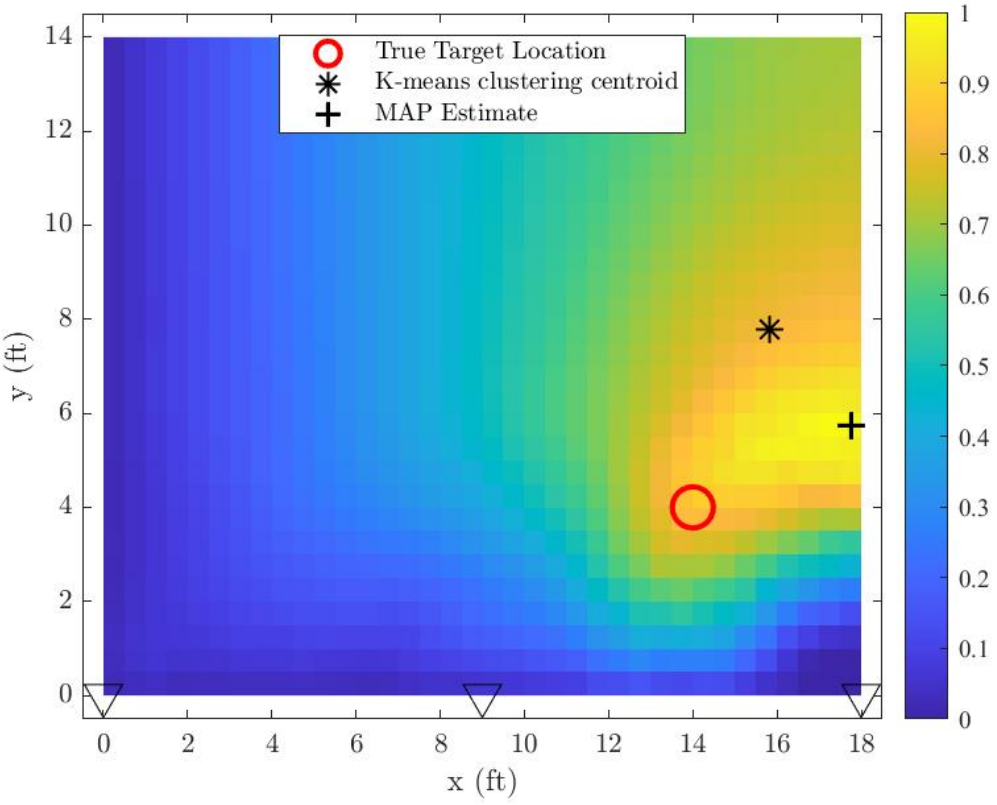

Figure 4.15: Method 4 attenuation image for target location (14,4).

Table 4.4: Performance metrics for NRN weight method 4 for targets at (9,7), (4,10), and (14,4).

Target Location	**Performance Metric**	**Description**	**Result**
(9,7)	K-means clustering	Coordinates of the centroid	(11.76,7.88) $\epsilon_{Centroid} = 2.90$ ft
	MAP Estimate	Coordinates of the highest intensity pixel	(9.25,1.25) $\epsilon_{MAP} = 5.76$ ft
	MSE	mean square error between the true target image and the attenuation image	$MSE = 0.4994$
	RMSE	root mean square error between true target location and centroid location	$RMSE = 2.0478$
	Dispersion Error	Pixel spread about the centroid	$\epsilon_{Dispersion} = 3.834$ ft
(4,10)	K-means clustering	Coordinates of the centroid	(15.40,8.36) $\epsilon_{Centroid} = 11.52$ ft
	MAP Estimate	Coordinates of the highest intensity pixel	(17.75,3.75) $\epsilon_{MAP} = 15.10$ ft
	MSE	mean square error between the true target image and the attenuation image	$MSE = 0.2790$
	RMSE	root mean square error between true target location and centroid location	$RMSE = 8.15$
	Dispersion Error	Pixel spread about the centroid	$\epsilon_{Dispersion} = 2.69$ ft
(14,4)	K-means clustering	Coordinates of the centroid	(15.56,7.55) $\epsilon_{Centroid} = 3.88$ ft
	MAP Estimate	Coordinates of the highest intensity pixel	(17.75,5.75) $\epsilon_{MAP} = 4.14$ ft
	MSE	mean square error between the true target image and the attenuation image	$MSE = 0.2060$
	RMSE	root mean square error between true target location and centroid location	$RMSE = 2.74$
	Dispersion Error	Pixel spread about the centroid	$\epsilon_{Dispersion} = 2.195$ ft

this weight method being the third one. Image smoothing caused by the exponential weighting contributed to a significant decrease in overall performance.

4.1.5 NRN Method 5: Jans Weighting Method with Focused Weighting

The JWM with focused weighting is utilized for NRN weighting method five. The JWM utilizes an artificial pixel grid at a finer resolution than the image to apply a more accurate weighting to the respective range rings of each noise radar. Utilizing this, the inner portion of each respective range ring has an increased weight which creates less range ring overlap in an attempt to increase target localization accuracy. The attenuation images are shown with the true target location, the K-means clustering centroid, and the MAP estimate. These metrics provide the ability to visually inspect the performance of the weighting method, as well as calculate the difference in true target location versus estimated target location.

Figure 4.16 displays the first target scenario where the target is located at (9,7). Noise and artifacts are present within the image, however, the target estimates are localized around the true target. This target scenario is expected to produce images with noise and artifacts while accurately localizing the target due to the central location of the target.

Figure 4.17 displays the second target scenario where the target is located at (4,10). Noise and artifacts are present within the image, and target localization suffers however to a lesser degree than weight method two. The visual localization is significantly improved from weight method one. The MAP estimate has a significant performance increase from weight method one. Performance relative to weight method appears to slightly improve, which was expected.

Figure 4.18 displays the third target scenario where the target is located at (14,4).

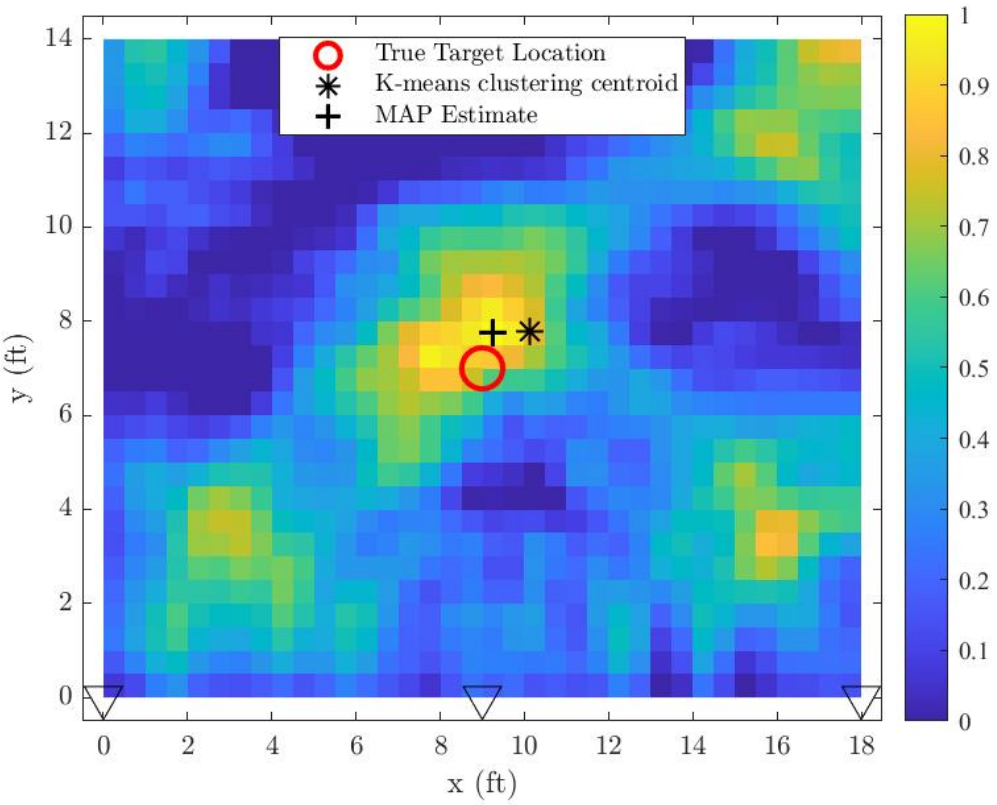

Figure 4.16: Method 5 attenuation image for target location (9,7).

Noise and artifacts are present within the image, however, targets are localized to the true target location. The intensity of the image pixels are focused around the true target locations, providing the target localization methods an optimal image for accurate target localization.

Table 4.5 shows the performance metric results for NRN weighting method five. The modification of the JWM provided focused weighting which led to an increased performance relative to weighting methods one and two. The expectation was that the focused weighting of each respective range ring would increase performance when compared to the original binary selection matrix and the default JWM. This method's focused weighting increased performance and target localization accuracy overall.

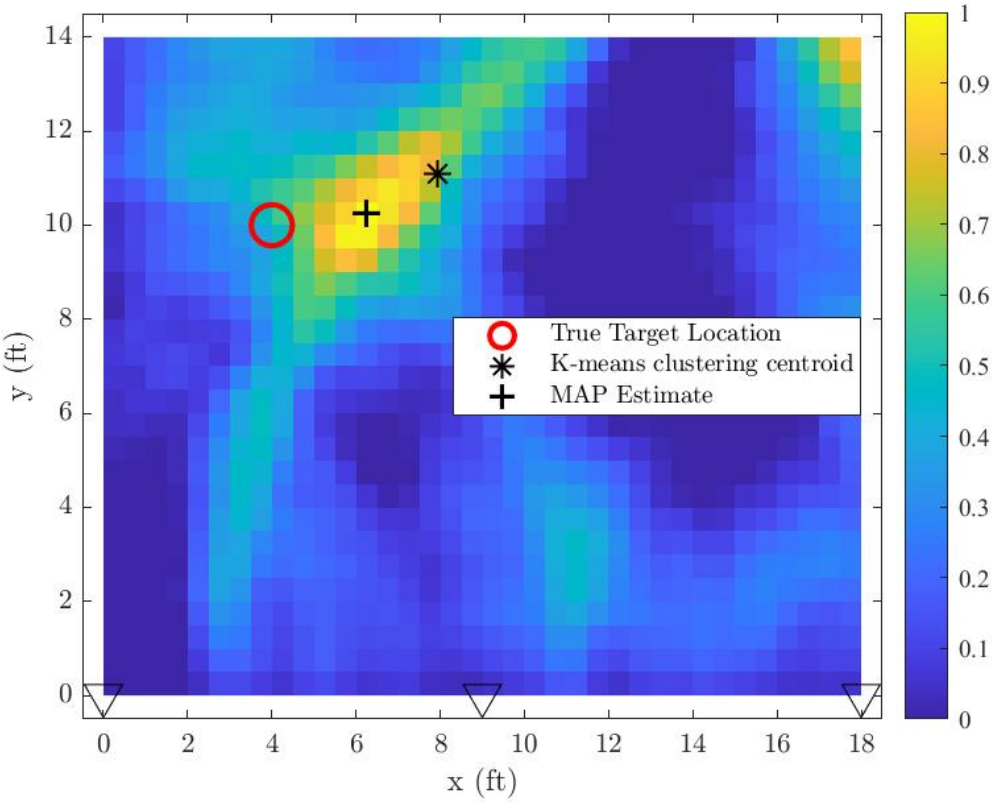

Figure 4.17: Method 5 attenuation image for target location (4,10).

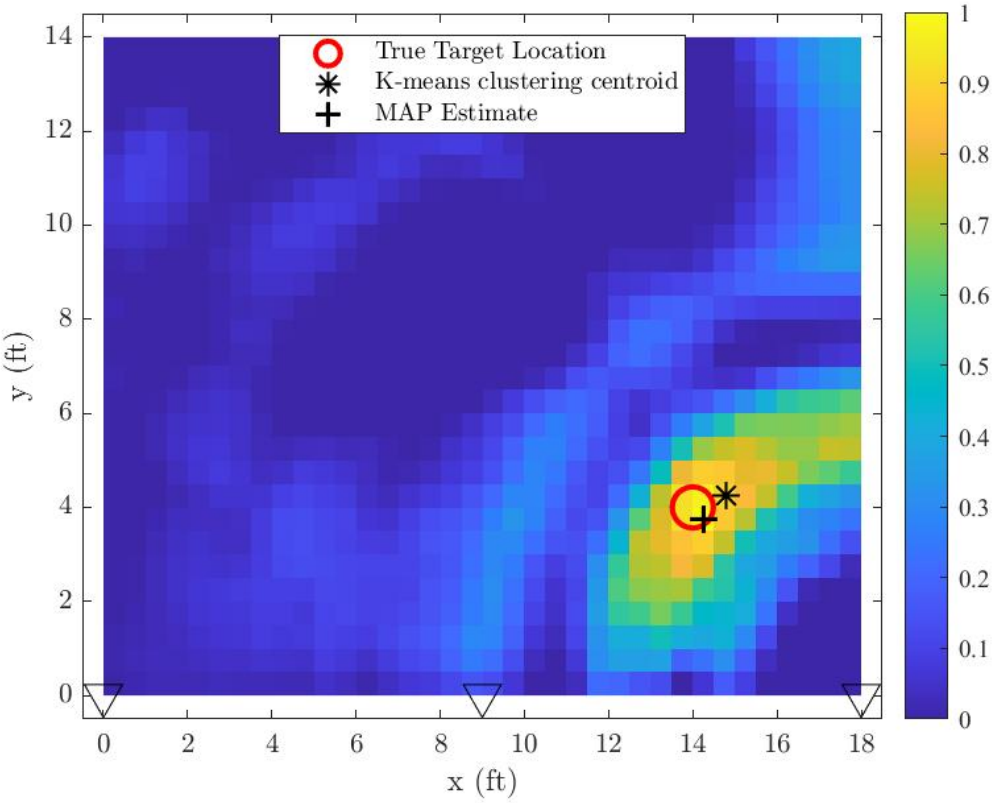

Figure 4.18: Method 5 attenuation image for target location (14,4).

Table 4.5: Performance metrics for NRN weight method 5 for targets at (9,7), (4,10), and (14,4).

Target Location	**Performance Metric**	**Description**	**Result**
(9,7)	K-means clustering	Coordinates of the centroid	(9.88,7.53) $\epsilon_{Centroid} = 1.03$ ft
	MAP Estimate	Coordinates of the highest intensity pixel	(9.25,7.75) $\epsilon_{MAP} = 0.7906$ ft
	MSE	mean square error between the true target image and the attenuation image	$MSE = 0.0825$
	RMSE	root mean square error between true target location and centroid location	$RMSE = 0.7288$
	Dispersion Error	Pixel spread about the centroid	$\epsilon_{Dispersion} = 3.76$ ft
(4,10)	K-means clustering	Coordinates of the centroid	(7.70,10.84) $\epsilon_{Centroid} = 3.79$ ft
	MAP Estimate	Coordinates of the highest intensity pixel	(6.25,10.25) $\epsilon_{MAP} = 2.26$ ft
	MSE	mean square error between the true target image and the attenuation image	$MSE = 0.0482$
	RMSE	root mean square error between true target location and centroid location	$RMSE = 2.68$
	Dispersion Error	Pixel spread about the centroid	$\epsilon_{Dispersion} = 2.65$ ft
(14,4)	K-means clustering	Coordinates of the centroid	(14.55,4.02) $\epsilon_{Centroid} = 0.5471$ ft
	MAP Estimate	Coordinates of the highest intensity pixel	(14.25,3.75) $\epsilon_{MAP} = 0.3536$ ft
	MSE	mean square error between the true target image and the attenuation image	$MSE = 0.0205$
	RMSE	root mean square error between true target location and centroid location	$RMSE = 0.3869$
	Dispersion Error	Pixel spread about the centroid	$\epsilon_{Dispersion} = 0.4395$ ft

4.2 Testbed Operation

The testbed provides the capability to analyze RTI, NRN, and fusion images. Image resolutions must match in order to allow for a fair comparison between each image. The testbed allows for data collection and analysis with ease. To provide a baseline of the testbed's capabilities, two experimental configurations are tested which demonstrate the ease of use of the testbed.

Figure 4.19 demonstrates the first experimental mode at target scenario (9,7). The weighting models used for RTI and NRN are generic methods which do not provide the best results when compared to newer weighting schemes available. The discrepancies between target localization of each method within the fusion image can be seen. This method utilizes an averaging of separate images; however, the MAP estimate proves to be an effective localization for this scenario. The NRN image contains less noise when compared to the RTI image. The fusion image target localization suffers to to the constructive noise which is created in the fusion image.

Figure 4.20 demonstrates an improvement in the separate images which leads to an improved fusion image. This improvement is a result of switching the weighting methods for both RTI and NRN to more optimal weighting methods. The weighting-g model and the JWM provided an enhanced level of weighting for their respective images. The ability to utilize a different weight model for both RTI and NRN demonstrates the flexibility and importance of the testbed when conducting research. The target localization of the fusion image is improved when compared to Figure 4.19.

Figure 4.21 provides the fusion data attenuation image performance for the two experimental cases of the testbed. The MAP estimate is the only performance metric where the first experimental case performs better than the second experimental case. Overall, the usage of improved weighting methods for RTI and NRN provide increased performance. For the centroid error, the second experimental case performs almost

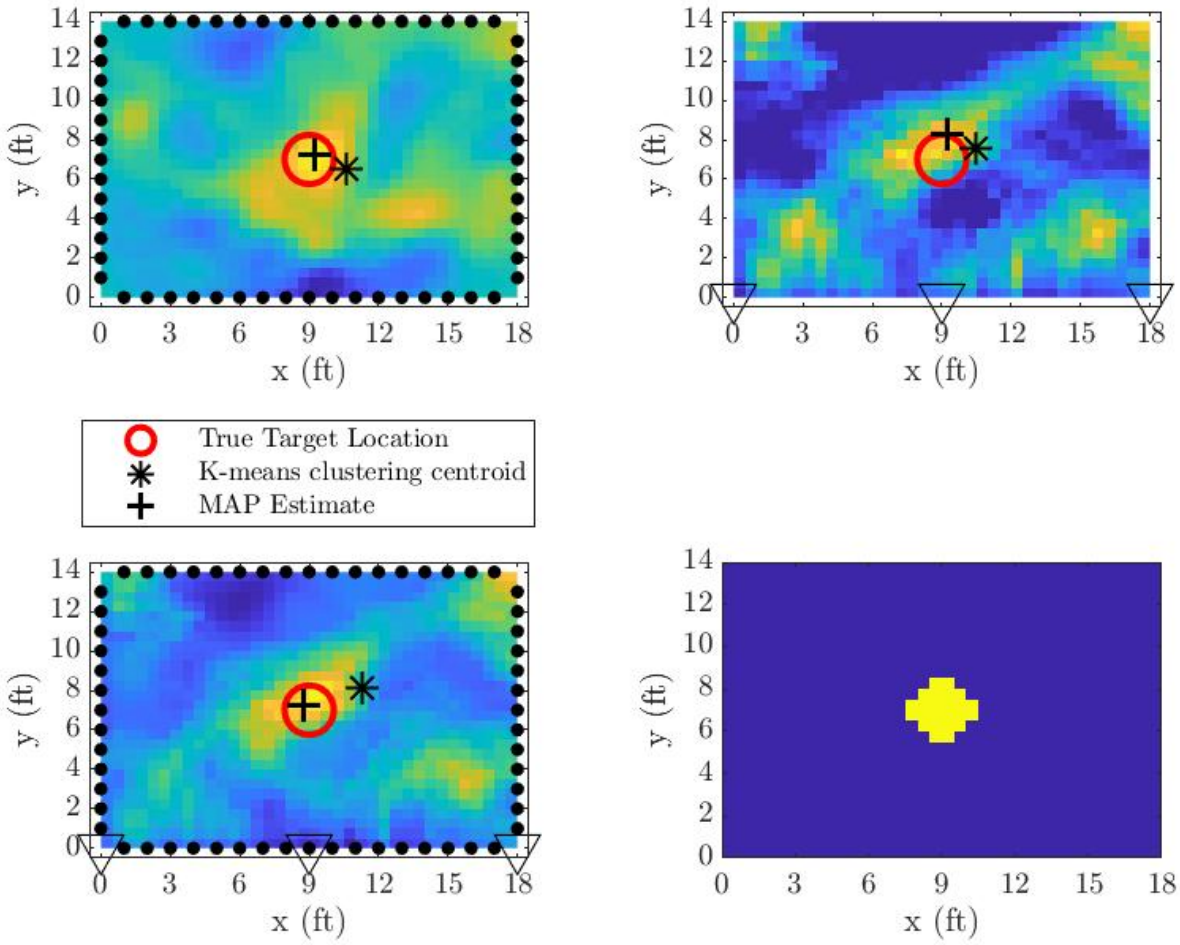

Figure 4.19: Testbed experimental mode 1 with (top left) the RTI image using NeSh weighting, (top right) NRN image using the binary selection matrix for weighting, (bottom left) the fused image which was formed by averaging the RTI and NRN images together, and (bottom right) the true target attenuation model for target scenario (9,7).

three times better when compared to the first experimental case.

Another capability provided by the testbed is the ability to input various data sets to be tested and analyzed. The testbed can easily be configured to match the experimental data's testing setup. Based on the setup, the experimental data can be utilized in combination with data gathered at different times and with different target scenarios.

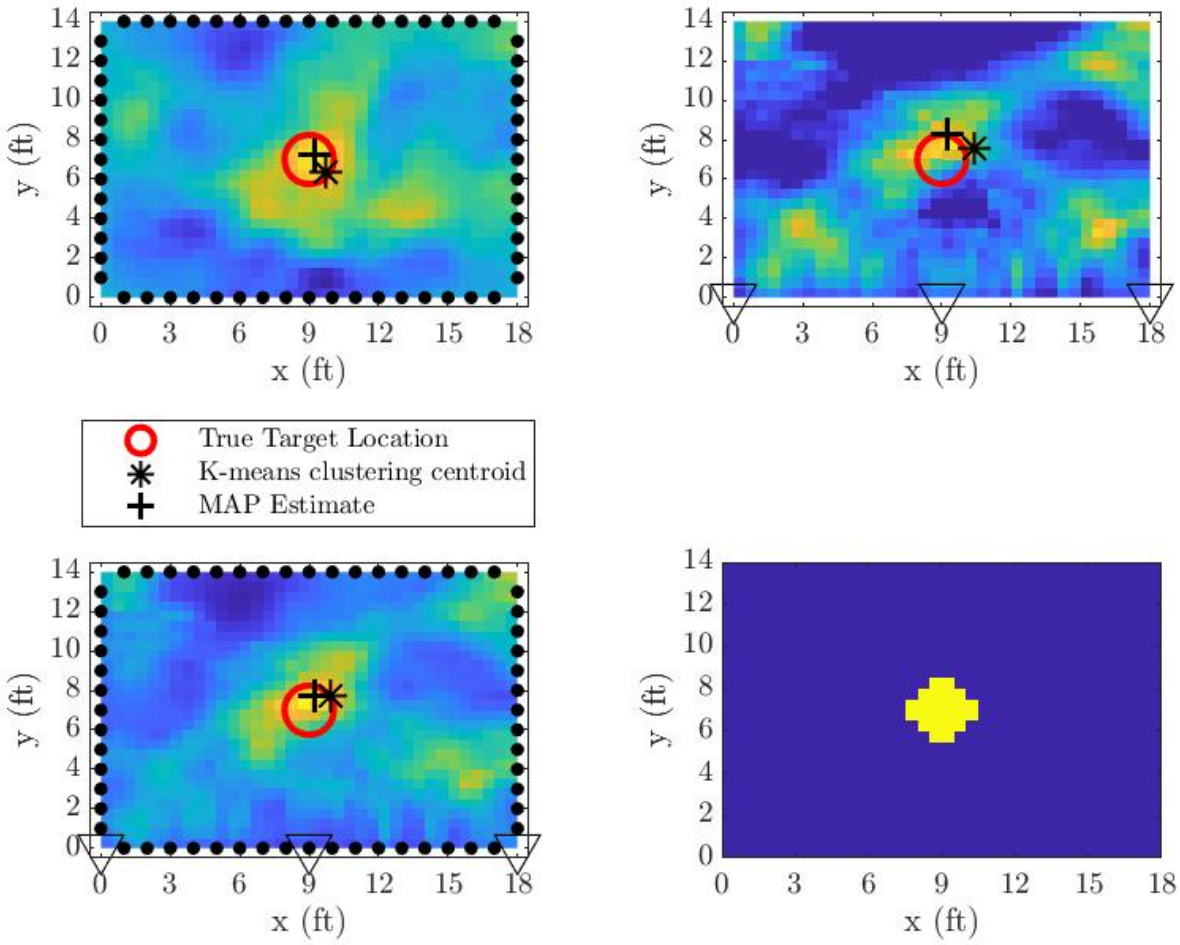

Figure 4.20: Testbed experimental mode 2 with (top left) the RTI image using the weighting-g model, (top right) NRN image using JWM, (bottom left) the fused image which was formed by averaging the RTI and NRN images together, and (bottom right) the true target attenuation model for target scenario (9,7).

Figure 4.22 demonstrates the flexibility of the testbed, utilizing data provided by Battle [2] for RTI research, and simulated NRN data. Both data sets do not contain significant noise and attenuation, which allows for accurate target localization. NRN data was not available for this target scenario; however, the testbed's ability to simulate NRN data can fill the gap. Battle's [2] contained a slightly different experimental target environment which was easily adjusted within the testbed.

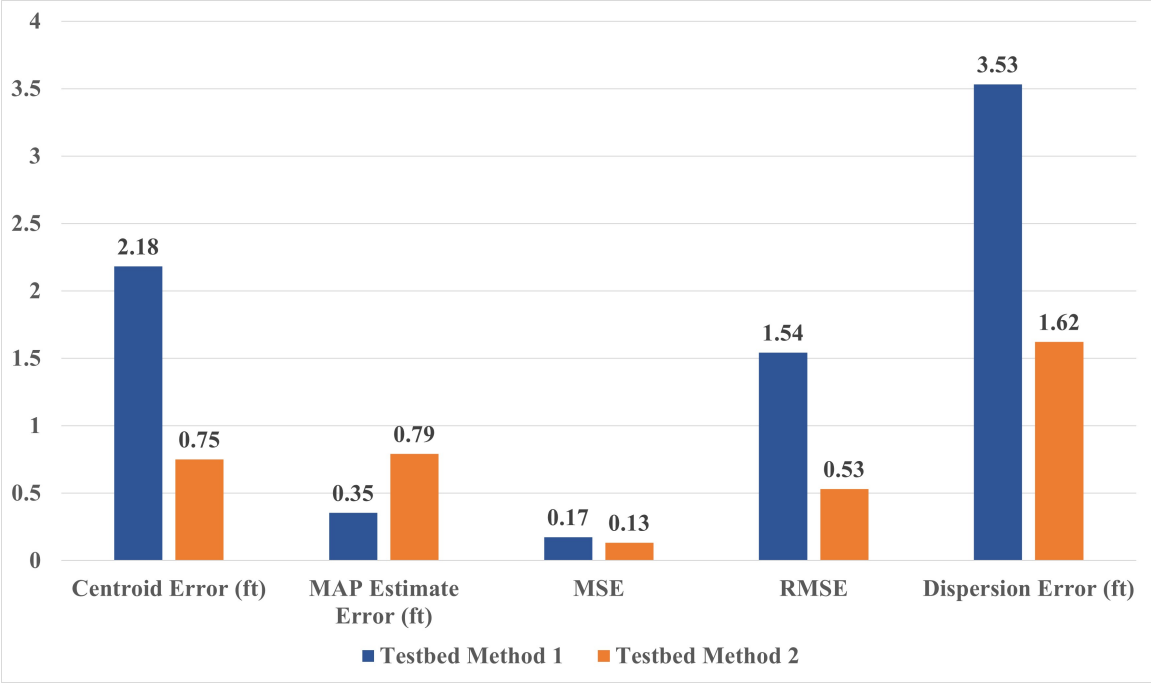

Figure 4.21: Performance metrics for the respective fusion attenuation images for each testbed method.

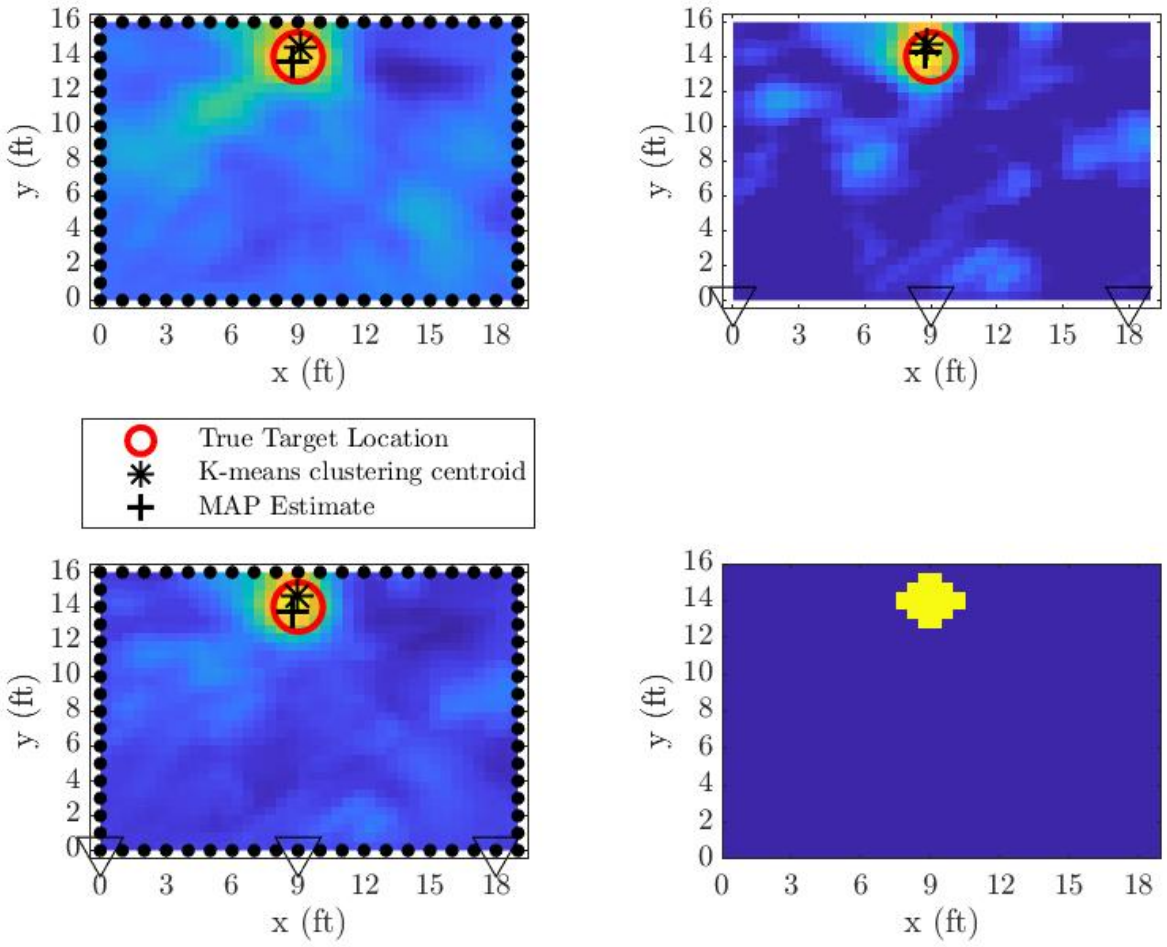

Figure 4.22: Testbed demonstrating an additional data set with (top left) the RTI image using NeSh weighting, (top right) NRN simulated data image using JWM weighting, the human cylindrical model, and a zero mean Gaussian noise, (bottom left) the fused image which was formed by averaging the RTI and NRN images together, and (bottom right) the true target attenuation model for target scenario (9,14).

4.3 Separate Image Data Fusion

There are five separate image fusion methods which will be analyzed to determine their viability. Separate image fusion provides a simple method of data fusion which can provide accurate localization results when compared to the separate respective images. The following fusion images were created utilizing RTI weighting-g model with Tikhonov reconstruction, and NRN utilizing the JWM with enhanced weighting. These weighting models and reconstruction method provide the optimal separate images required to accurately compare the fusion methods. The five separate image fusion methods which were utilized are shown below:

- Fusion Method 1: Averaging Images
- Fusion Method 2: Average Images and Favor RTI Data
- Fusion Method 3: Average Images and Favor NRN Data
- Fusion Method 4: Focus Box on NRN Data
- Fusion Method 5: Focus Box on RTI Data

Each of the three target scenarios were utilized to provide a baseline of performance as opposed to utilizing a single target scenario. A single target scenario may favor RTI or NRN resulting in inaccurate conclusion being drawn from the fusion methods.

4.3.1 Fusion Method 1: Averaging Images

The first fusion method averages the respective RTI and NRN images together to formed the fused image. Three target scenarios are tested to gather a baseline performance for each fusion method. The attenuation images are shown with the true target location, the K-means clustering centroid, and the MAP estimate. These metrics provide the ability to visually inspect the performance of the fusion method,

as well as calculate the difference in true target location versus estimated target location. Figure 4.23 shows the three target scenarios for fusion method one and Table 4.6 provides the performance metrics. The analysis of the average performance of the fusion methods will be conducted in Section 4.4.2.

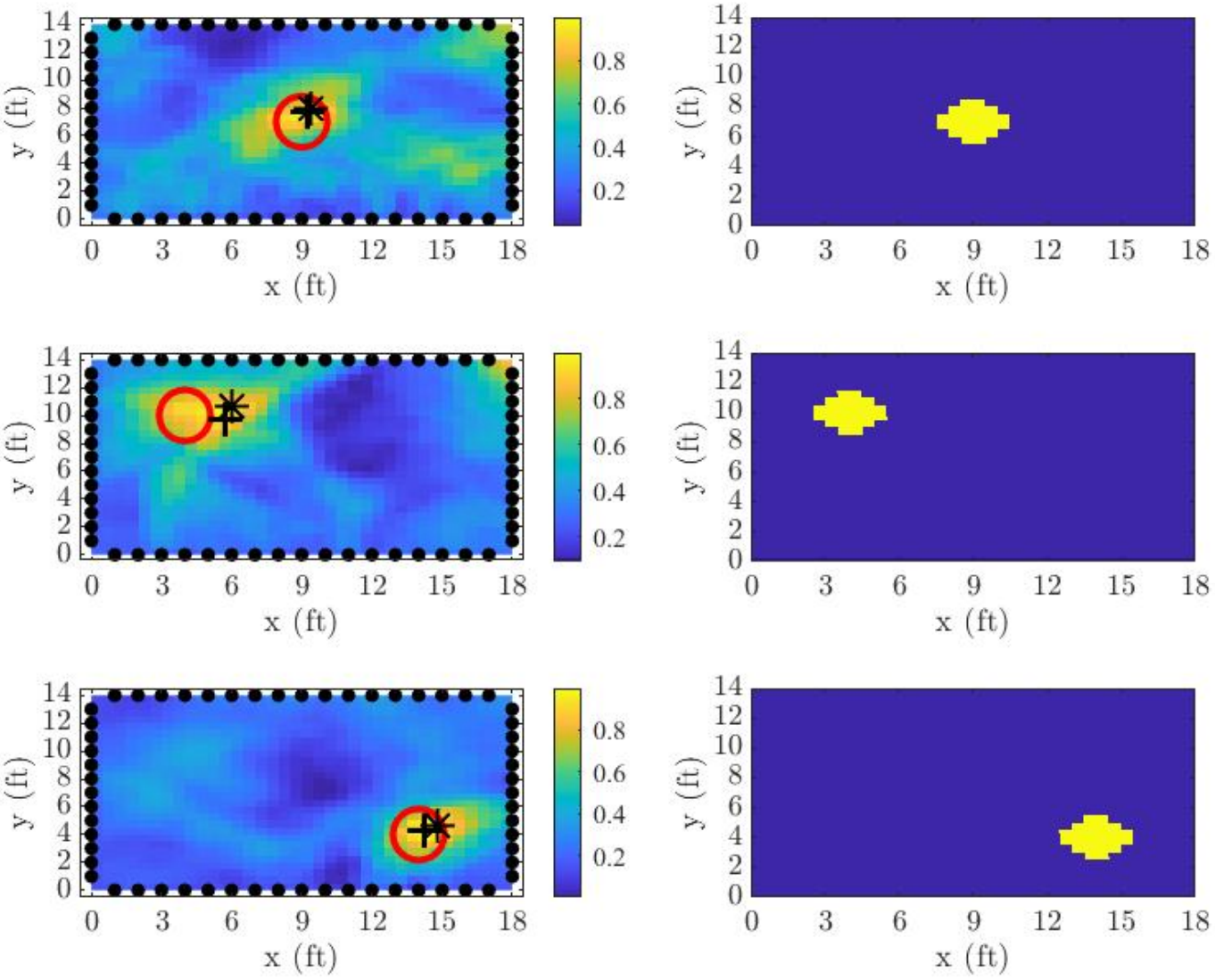

Figure 4.23: Testbed fusion image one: averaging images for (top left) the target scenario (9,7), (middle left) the target scenario (4,10), (bottom left) the target scenario (14,4), and (right) their respective true target attenuation images for fusion method 1.

Target Location	**Performance Metric**	**Description**	**Result**
(9,7)	K-means clustering	Centroid localization error	$\epsilon_{Centroid} = 0.7506$ ft
	MAP Estimate	MAP localization error	$\epsilon_{MAP} = 0.7906$ ft
	MSE	mean square error between the true target image and the attenuation image	$MSE = 0.1328$
	RMSE	root mean square error between true target location and centroid location	$RMSE = 0.5307$
	Dispersion Error	Pixel spread about the centroid	$\epsilon_{Dispersion} = 1.6214$ ft
(4,10)	K-means clustering	Centroid localization error	$\epsilon_{Centroid} = 1.792$ ft
	MAP Estimate	MAP localization error	$\epsilon_{MAP} = 1.77$ ft
	MSE	mean square error between the true target image and the attenuation image	$MSE = 0.1437$
	RMSE	root mean square error between true target location and centroid location	$RMSE = 1.267$
	Dispersion Error	Pixel spread about the centroid	$\epsilon_{Dispersion} = 2.614$ ft
(14,4)	K-means clustering	Centroid localization error	$\epsilon_{Centroid} = 0.6414$ ft
	MAP Estimate	MAP localization error	$\epsilon_{MAP} = 0.3536$ ft
	MSE	mean square error between the true target image and the attenuation image	$MSE = 0.0658$
	RMSE	root mean square error between true target location and centroid location	$RMSE = 0.4535$
	Dispersion Error	Pixel spread about the centroid	$\epsilon_{Dispersion} = 0.1761$ ft

Table 4.6: Performance metrics for fusion method 1 for targets at (9,7), (4,10), and (14,4).

4.3.2 Fusion Method 2: Average Images and Favor RTI Data

The second fusion method favors the RTI data and averages the respective RTI and NRN images together to formed the fused image. Three target scenarios are tested to gather a baseline performance for each fusion method. The attenuation images are shown with the true target location, the K-means clustering centroid, and the MAP estimate. These metrics provide the ability to visually inspect the performance of the fusion method, as well as calculate the difference in true target location versus estimated target location. Figure 4.24 shows the three target scenarios for fusion method two and Table 4.7 provides the performance metrics. The analysis of the average performance of the fusion methods will be conducted in Section 4.4.2.

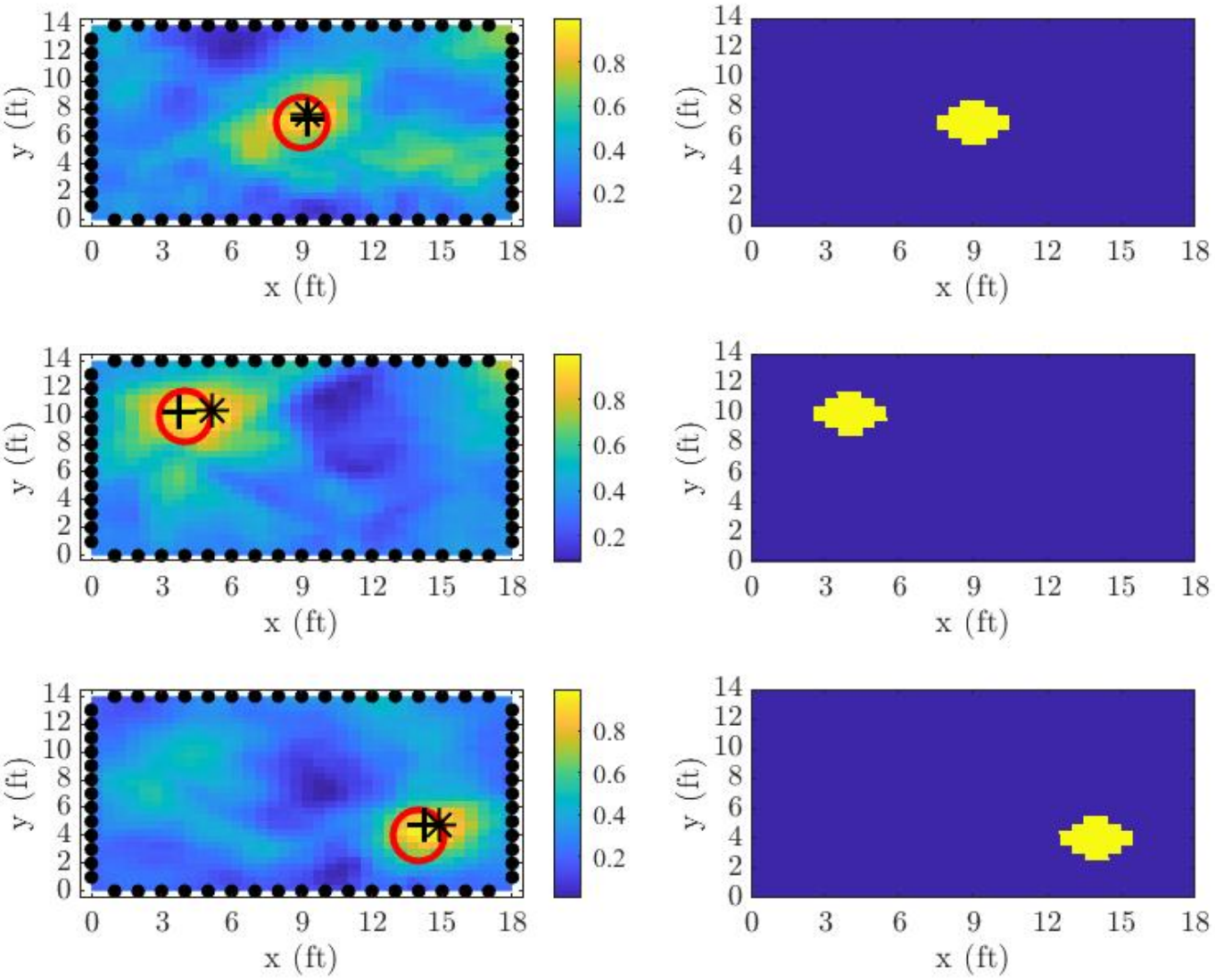

Figure 4.24: Testbed fusion image two: average images and favor RTI data for (top left) the target scenario (9,7), (middle left) the target scenario (4,10), (bottom left) the target scenario (14,4), and (right) their respective true target attenuation images for fusion method 2.

Target Location	**Performance Metric**	**Description**	**Result**
(9,7)	K-means clustering	Centroid localization error	$\epsilon_{Centroid} = 0.32$ ft
	MAP Estimate	MAP localization error	$\epsilon_{MAP} = 0.354$ ft
	MSE	mean square error between the true target image and the attenuation image	$MSE = 0.1546$
	RMSE	root mean square error between true target location and centroid location	$RMSE = 0.2263$
	Dispersion Error	Pixel spread about the centroid	$\epsilon_{Dispersion} = 1.266$ ft
(4,10)	K-means clustering	Centroid localization error	$\epsilon_{Centroid} = 0.9674$ ft
	MAP Estimate	MAP localization error	$\epsilon_{MAP} = .354$ ft
	MSE	mean square error between the true target image and the attenuation image	$MSE = 0.1701$
	RMSE	root mean square error between true target location and centroid location	$RMSE = 0.6841$
	Dispersion Error	Pixel spread about the centroid	$\epsilon_{Dispersion} = 2.044$ ft
(14,4)	K-means clustering	Centroid localization error	$\epsilon_{Centroid} = 0.756$ ft
	MAP Estimate	MAP localization error	$\epsilon_{MAP} = 0.791$ ft
	MSE	mean square error between the true target image and the attenuation image	$MSE = 0.093$
	RMSE	root mean square error between true target location and centroid location	$RMSE = 0.535$
	Dispersion Error	Pixel spread about the centroid	$\epsilon_{Dispersion} = 0.164$ ft

Table 4.7: Performance metrics for fusion method 2 for targets at (9,7), (4,10), and (14,4).

4.3.3 Fusion Method 3: Average Images and Favor NRN Data

The third fusion method favors the NRN data and averages the respective RTI and NRN images together to formed the fused image. Three target scenarios are tested to gather a baseline performance for each fusion method. The attenuation images are shown with the true target location, the K-means clustering centroid, and the MAP estimate. These metrics provide the ability to visually inspect the performance of the fusion method, as well as calculate the difference in true target location versus estimated target location. Figure 4.25 shows the three target scenarios for fusion method three and Table 4.8 provides the performance metrics. The analysis of the average performance of the fusion methods will be conducted in Section 4.4.2.

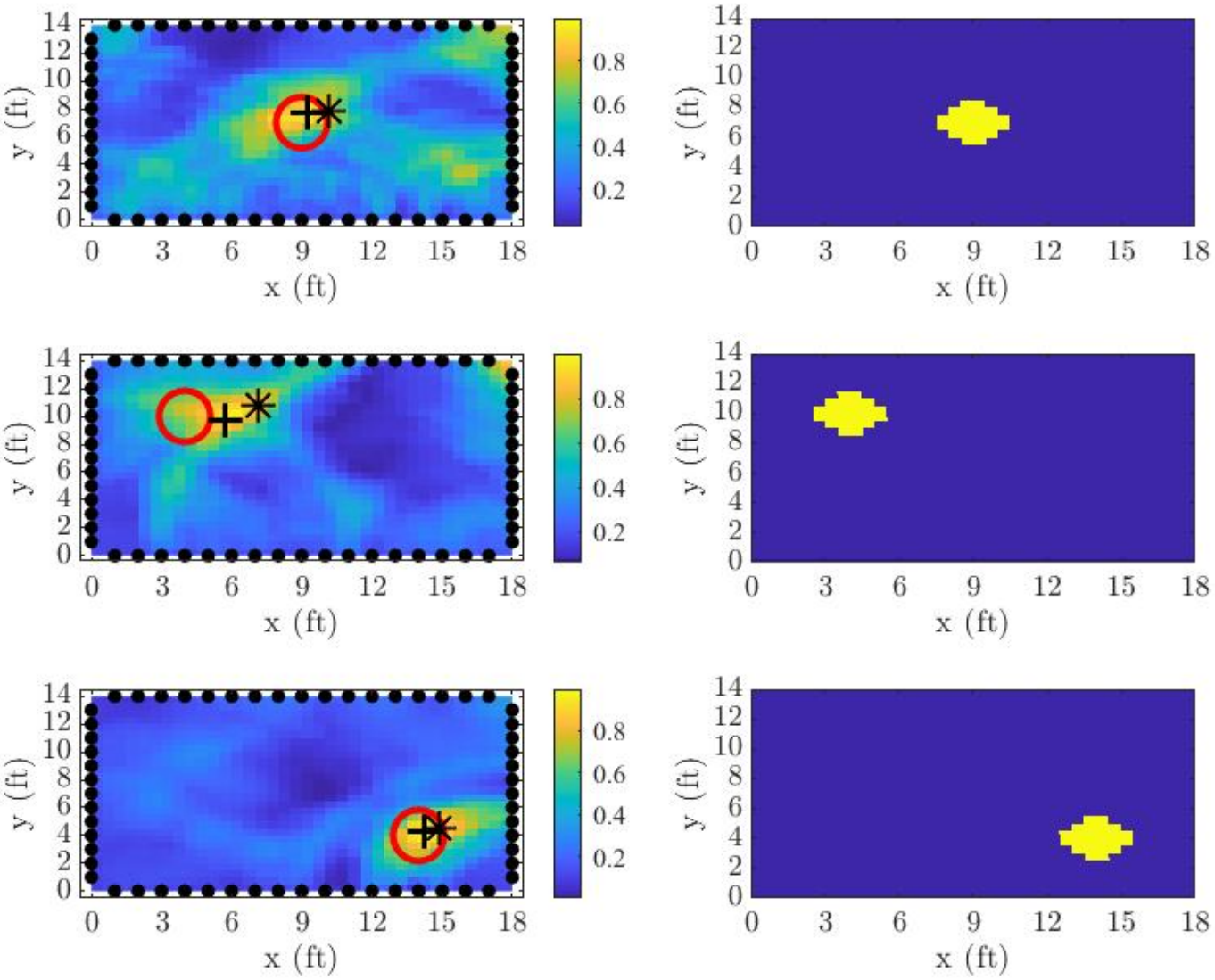

Figure 4.25: Testbed fusion image three: average images and favor NRN data for (top left) the target scenario (9,7), (middle left) the target scenario (4,10), (bottom left) the target scenario (14,4), and (right) their respective true target attenuation images for fusion method 3.

Target Location	**Performance Metric**	**Description**	**Result**
(9,7)	K-means clustering	Centroid localization error	$\epsilon_{Centroid} = 1.0995$ ft
	MAP Estimate	MAP localization error	$\epsilon_{MAP} = 0.7906$ ft
	MSE	mean square error between the true target image and the attenuation image	$MSE = 0.1125$
	RMSE	root mean square error between true target location and centroid location	$RMSE = 0.778$
	Dispersion Error	Pixel spread about the centroid	$\epsilon_{Dispersion} = 2.6134$ ft
(4,10)	K-means clustering	Centroid localization error	$\epsilon_{Centroid} = 2.94$ ft
	MAP Estimate	MAP localization error	$\epsilon_{MAP} = 1.77$ ft
	MSE	mean square error between the true target image and the attenuation image	$MSE = 0.10$
	RMSE	root mean square error between true target location and centroid location	$RMSE = 2.08$
	Dispersion Error	Pixel spread about the centroid	$\epsilon_{Dispersion} = 2.95$ ft
(14,4)	K-means clustering	Centroid localization error	$\epsilon_{Centroid} = 0.716$ ft
	MAP Estimate	MAP localization error	$\epsilon_{MAP} = 0.3536$ ft
	MSE	mean square error between the true target image and the attenuation image	$MSE = 0.045$
	RMSE	root mean square error between true target location and centroid location	$RMSE = 0.5061$
	Dispersion Error	Pixel spread about the centroid	$\epsilon_{Dispersion} = 0.1883$ ft

Table 4.8: Performance metrics for fusion method 3 for targets at (9,7), (4,10), and (14,4).

4.3.4 Fusion Method 4: Focus Box on NRN Data

The fourth fusion method creates a focus box which favors the NRN data in the center of the image and the RTI data outside of the center of the image. Three target scenarios are tested to gather a baseline performance for each fusion method. The three target scenarios for this fusion method provide three different scenarios for the focus box: a target outside of the box, a target in the box, and a target on the edge of the box. The attenuation images are shown with the true target location, the K-means clustering centroid, and the MAP estimate. These metrics provide the ability to visually inspect the performance of the fusion method, as well as calculate the difference in true target location versus estimated target location. Figure 4.26 shows the three target scenarios for fusion method four and Table 4.9 provides the performance metrics. The analysis of the average performance of the fusion methods will be conducted in Section 4.4.2.

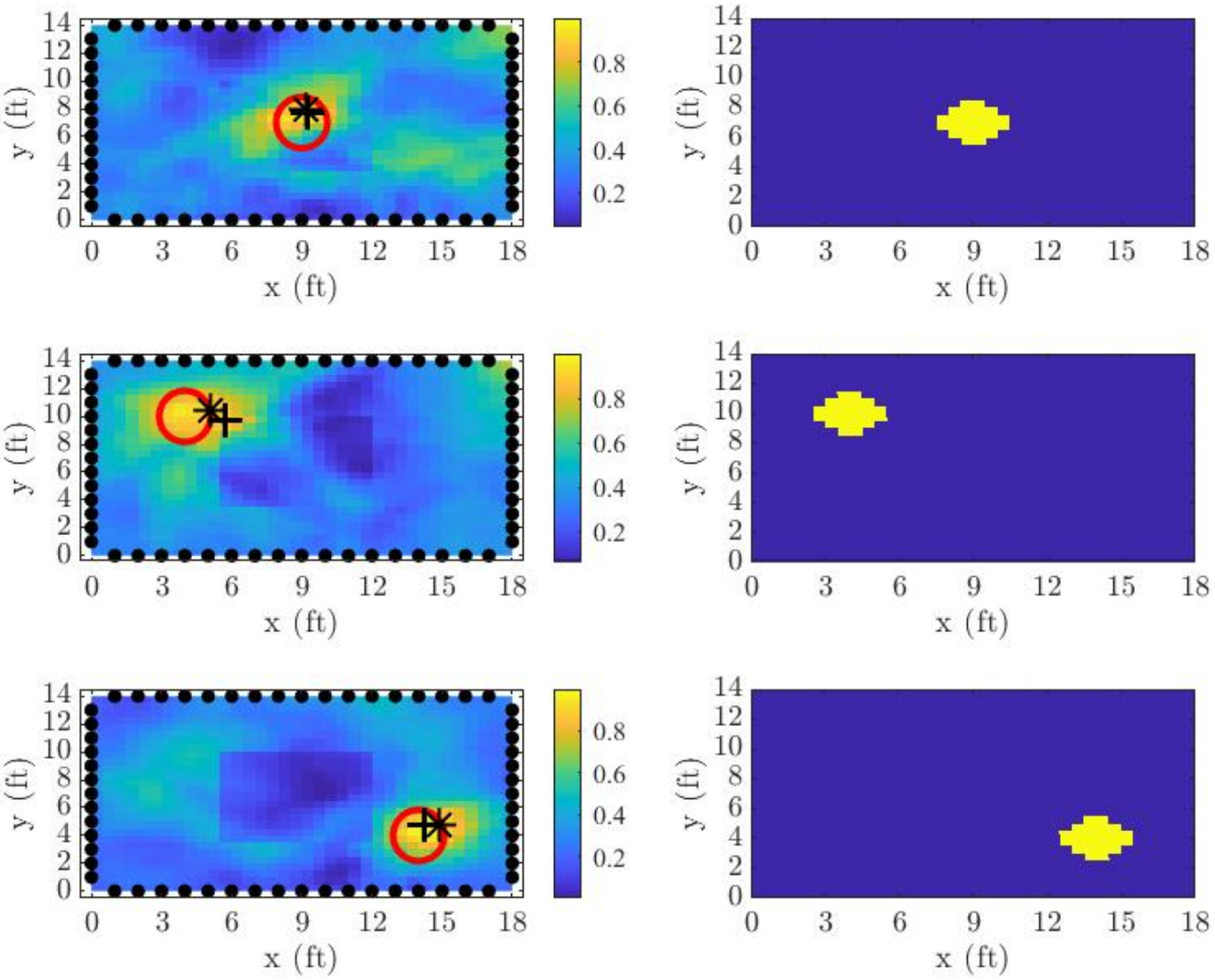

Figure 4.26: Testbed fusion image four: focus box on NRN data for (top left) the target scenario (9,7), (middle left) the target scenario (4,10), (bottom left) the target scenario (14,4), and (right) their respective true target attenuation images for fusion method 4.

Target Location	**Performance Metric**	**Description**	**Result**
(9,7)	K-means clustering	Centroid localization error	$\epsilon_{Centroid} = 0.675$ ft
	MAP Estimate	MAP localization error	$\epsilon_{MAP} = 0.7906$ ft
	MSE	mean square error between the true target image and the attenuation image	$MSE = 0.1394$
	RMSE	root mean square error between true target location and centroid location	$RMSE = 0.477$
	Dispersion Error	Pixel spread about the centroid	$\epsilon_{Dispersion} = 1.145$ ft
(4,10)	K-means clustering	Centroid localization error	$\epsilon_{Centroid} = 0.842$ ft
	MAP Estimate	MAP localization error	$\epsilon_{MAP} = 1.768$ ft
	MSE	mean square error between the true target image and the attenuation image	$MSE = 0.146$
	RMSE	root mean square error between true target location and centroid location	$RMSE = 0.5955$
	Dispersion Error	Pixel spread about the centroid	$\epsilon_{Dispersion} = 1.725$ ft
(14,4)	K-means clustering	Centroid localization error	$\epsilon_{Centroid} = 0.756$ ft
	MAP Estimate	MAP localization error	$\epsilon_{MAP} = 0.7906$ ft
	MSE	mean square error between the true target image and the attenuation image	$MSE = 0.087$
	RMSE	root mean square error between true target location and centroid location	$RMSE = 0.535$
	Dispersion Error	Pixel spread about the centroid	$\epsilon_{Dispersion} = 0.164$ ft

Table 4.9: Performance metrics for fusion method 4 for targets at (9,7), (4,10), and (14,4).

4.3.5 Fusion Method 5: Focus Box on RTI Data

The fourth fusion method creates a focus box which favors the RTI data in the center of the image and the NRN data outside of the center of the image. Three target scenarios are tested to gather a baseline performance for each fusion method. The three target scenarios for this fusion method provide three different scenarios for the focus box: a target outside of the box, a target in the box, and a target on the edge of the box. The attenuation images are shown with the true target location, the K-means clustering centroid, and the MAP estimate. These metrics provide the ability to visually inspect the performance of the fusion method, as well as calculate the difference in true target location versus estimated target location. Figure 4.27 shows the three target scenarios for fusion method four and Table 4.10 provides the performance metrics. The analysis of the average performance of the fusion methods will be conducted in Section 4.4.2.

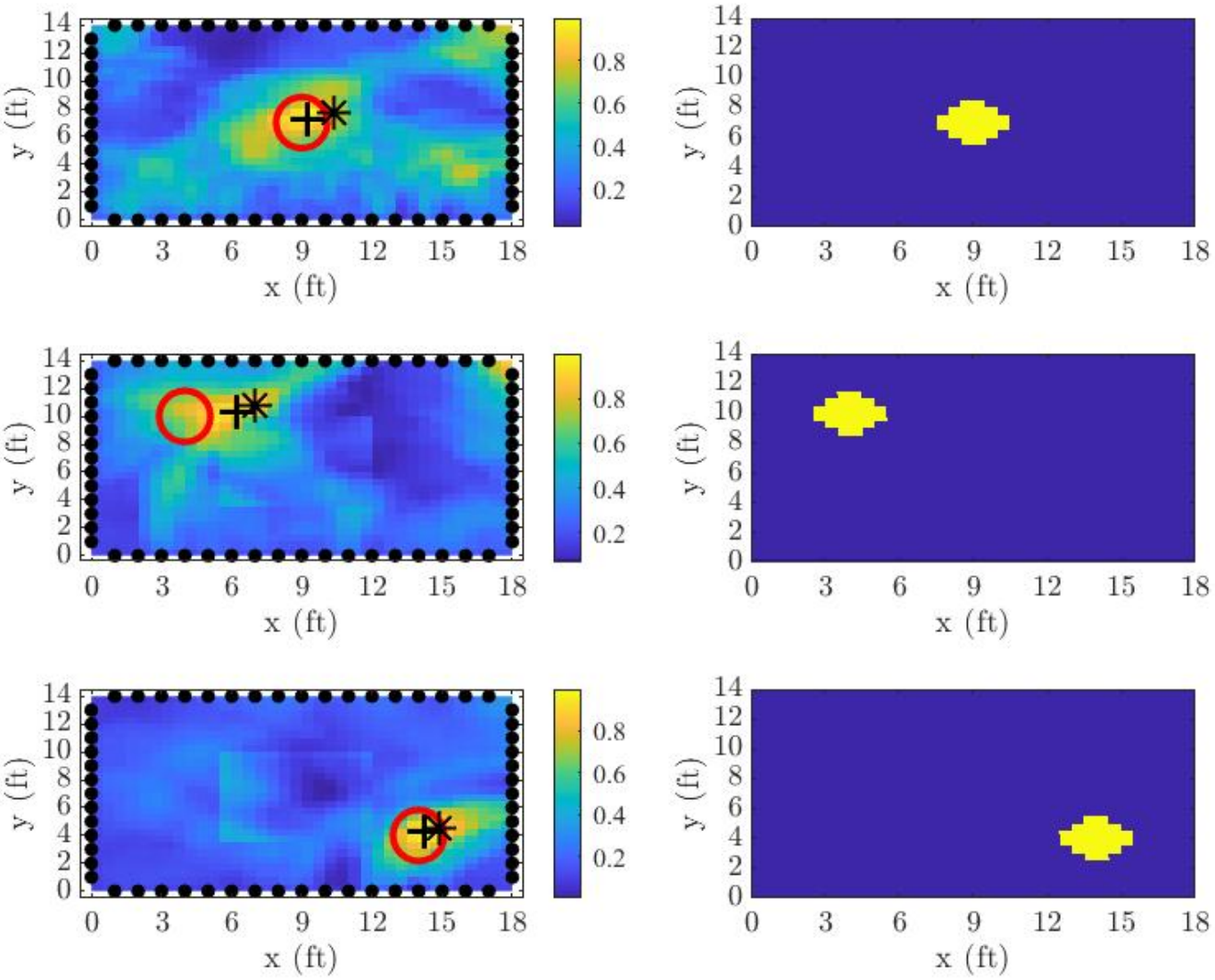

Figure 4.27: Testbed fusion image five: focus box on RTI data for (top left) the target scenario (9,7), (middle left) the target scenario (4,10), (bottom left) the target scenario (14,4), and (right) their respective true target attenuation images for fusion method 5.

Target Location	**Performance Metric**	**Description**	**Result**
(9,7)	K-means clustering	Centroid localization error	$\epsilon_{Centroid} = 1.221$ ft
	MAP Estimate	MAP localization error	$\epsilon_{MAP} = 0.3536$ ft
	MSE	mean square error between the true target image and the attenuation image	$MSE = 0.1261$
	RMSE	root mean square error between true target location and centroid location	$RMSE = 0.863$
	Dispersion Error	Pixel spread about the centroid	$\epsilon_{Dispersion} = 2.855$ ft
(4,10)	K-means clustering	Centroid localization error	$\epsilon_{Centroid} = 2.81$ ft
	MAP Estimate	MAP localization error	$\epsilon_{MAP} = 2.264$ ft
	MSE	mean square error between the true target image and the attenuation image	$MSE = 0.114$
	RMSE	root mean square error between true target location and centroid location	$RMSE = 1.99$
	Dispersion Error	Pixel spread about the centroid	$\epsilon_{Dispersion} = 2.99$ ft
(14,4)	K-means clustering	Centroid localization error	$\epsilon_{Centroid} = 0.716$ ft
	MAP Estimate	MAP localization error	$\epsilon_{MAP} = 0.3536$ ft
	MSE	mean square error between the true target image and the attenuation image	$MSE = 0.045$
	RMSE	root mean square error between true target location and centroid location	$RMSE = 0.5062$
	Dispersion Error	Pixel spread about the centroid	$\epsilon_{Dispersion} = 0.1883$ ft

Table 4.10: Performance metrics for fusion method 5 for targets at (9,7), (4,10), and (14,4).

4.4 Overall Performance Results

Performance results were complied to provide an overview for each area explored within this thesis. These performance results contain the averaged results from the three target scenarios utilized.

4.4.1 NRN Weighting Method Average Results

In order to provide a direct comparison of the performance metrics for the five NRN weighting methods, each weighting method was averaged across the three target scenarios. The average values for each weight method can be compared to analyze which weighting methods provided the most accurate target localization capabilities and produced the lowest errors.

Figure 4.28 and Figure 4.29 illustrate the performance metric data for the five NRN weighting methods. Overall, weighting method five provided the most accurate

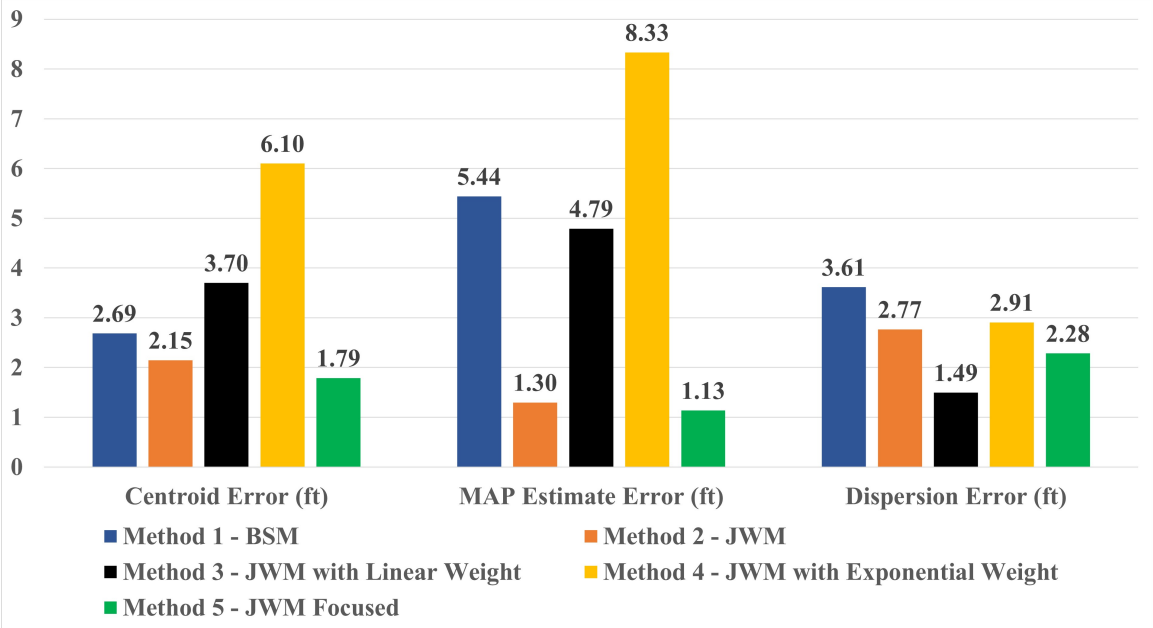

Figure 4.28: Graph of average position error and dispersion performance metrics for NRN weighting methods.

Figure 4.29: Graph of average MSE and RMSE performance metrics for NRN weighting methods.

target localization. This weighting method utilized the JWM with focused weighting on the interior of each respective range ring. It successfully mitigated unwanted range ring overlap to provide a more accurate method of localization. Performance increased with respect to method one and method two. The reduction in localization error is due to an improved attenuation image. The improved attenuation image is a result of the JWM's ability to more accurately weight the range rings of the NRN. The second best weighting method was the default JWM. This demonstrates that the analogous application of a WSN and RTI weighting concepts to NRN weighting can be successfully conducted and studied within the testbed. The performance increase of the JWM is strongly highlighted when compared to binary selection matrix weighting, the previous method of NRN weighting.

The application of distance based weighting within the NRN was not as successful as the traditional weighting applications conducted on the range rings. Weighting method three successfully lowered the dispersion error and only suffered high errors

on one of three target scenarios. Without the (9,7) target scenario, the JWM linear weighting performance increases. The increased performance is comparable to the performance of the default JWM. The exponential distance weighting was the worst overall weighting method across all five performance metrics as well as visual inspection of the attenuation images. This occurs due to the significant weighting fall off within the test environment. The exponential decay would have to be modified to produce more optimal results.

4.4.2 Separate Image Fusion Average Results

Separate image fusion is a simple and viable method of data fusion for RTI and NRN. Previously, averaging the respective images together was conducted. To further the separate image fusion, four new methods were proposed. The separate image fusion results yielded two main observations.

Figure 4.30 show the results from the five fusion methods analyzed. The first observation is that target localization accuracy performance can be increased easily with minor adjustments to the manner in which separate images are fused. By weighting the separate images before averaging them, localization accuracy increases. The second observation is that the analysis of the separate image fusion allows for additional insight into performance of the respective RTI and NRN images. For example, Fusion

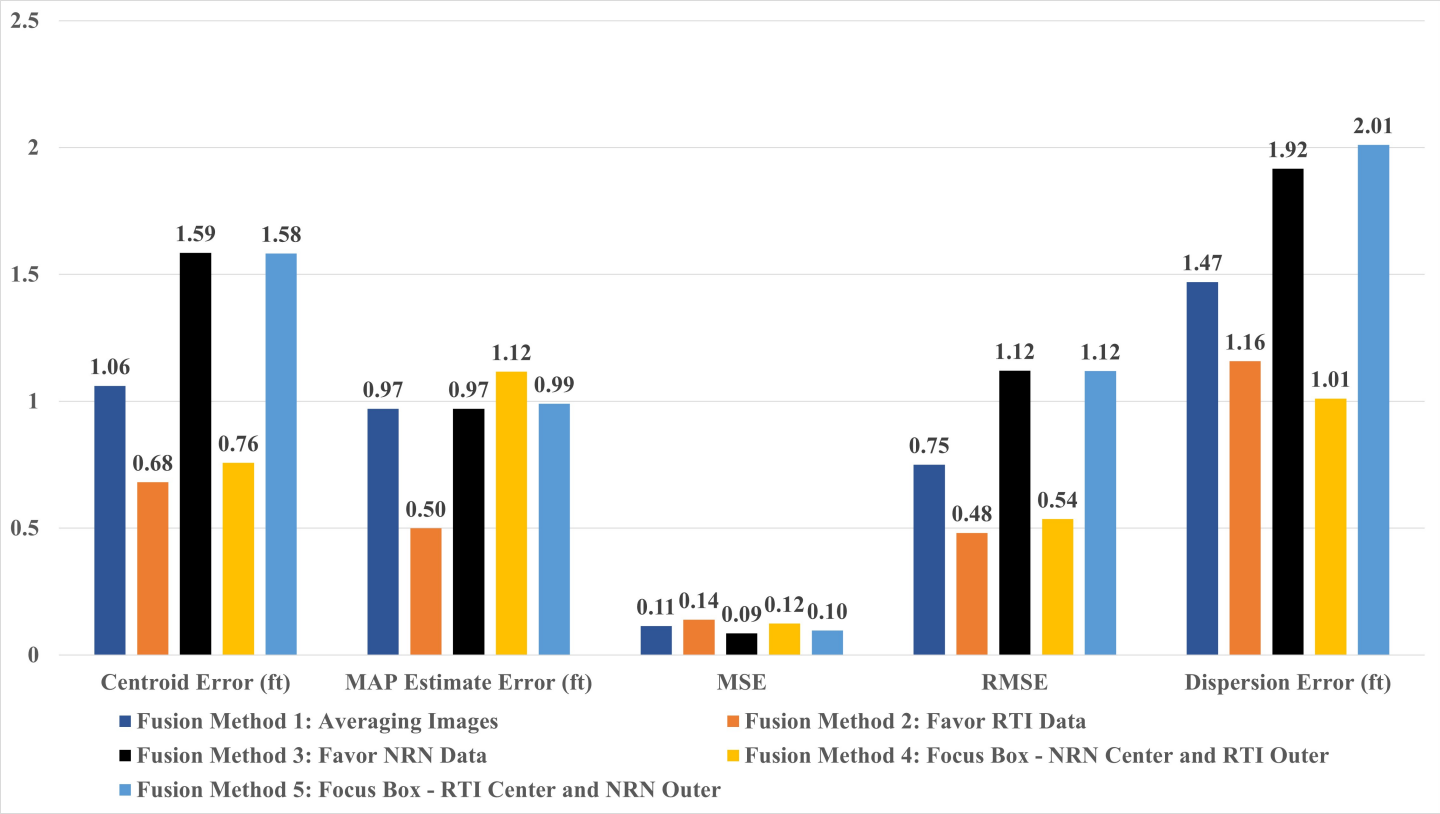

Figure 4.30: Graph of average performance values for the three target scenarios for each separate image fusion method.

methods two and four performed better than fusion methods three and five. This is directly due to the increased target localization accuracy of the RTI image. While each target scenario varies, for the three tested target scenarios RTI performed better. This observation can be concluded from studying the averaged performance metrics for RTI and NRN; however, additional adjustments could be made based on observing this result with the images fused. This would allow for a more flexible weighting of each of the separate images. For example, if the RTI image is more accurate, the user could test a performance range of weighting for that image which would utilize the positive characteristics from both the RTI and NRN image. This would provide a better separate image data fusion scheme, as opposed to a generic average image weighting.

V. Conclusions

This thesis resulted in the construction of a simulation testbed which was utilized to study and propose new NRN weighting methods. The testbed allows for weighting models, reconstruction methods, and data fusion techniques to be seamlessly applied to RTI and NRN data.

The creation of the JWM allowed for a new method for NRN weighting to be created and leveraged into additional weighting methods for NRN. The JWM has the ability to mimic WSN links by increasing the resolution of the range rings used for trilateration. When compared to the binary selection matrix which was previously used in NRN weighting, the JWM showed a 20% increase in target localization accuracy for the centroid target estimate. The JWM with focused weighting showed a 33% increase in target localization accuracy for the centroid target estimate when compared to the binary selection matrix. For the MAP target estimate, the JWM showed a 76% target localization accuracy improvement, and the JWM with focused weighting showed a 79% localization accuracy improvement. The performance increases are a direct result of the reduction in image noise and artifacts that is provided by the JWM. The MAP estimate is more reliable when the target being localized is located around the global intensity peak in the attenuation image. The significant increase in MAP estimate performance demonstrate this has been achieved by the JWM and the JWM with focused weighting.

Separate image fusion was also successfully in increasing target localization accuracy and providing a new ability to analyze the effectiveness of the RTI and NRN data contributions to the fusion image. For the three target scenarios tested, the RTI data achieved a higher target localization accuracy when compared to the NRN data. This conclusion is relative to the average of the three target scenarios utilized for this thesis. Parameters such as the smoothing term, ellipse width, and weighting

method used are scenario dependent. Each target scenario could be further improved; however, this is only possible when the true target location is known. For analyzing experimental data and deploying this testbed in situations where the target is unknown, certain parameter settings would have to be generalized based on previous experimental data.

5.1 Future Work

The main contribution from this thesis for future research is the creation of the simulation testbed for RTI and NRN. This testbed allowed for the creation of the JWM to further NRN research. The work conducted in this thesis could be further explored in the following ways:

- Study disparate data fusion methods to expand the ability to fuse raw data as opposed to separate images.
- Determine additional methods of NRN weighting models to increase localization accuracy, specifically looking into how distance based attenuation can be incorporated in the JWM.
- Create new target scenario data sets for RTI and NRN to explore multi-target scenarios.
- Explore bistatic configurations of NRN to determine expanded methods of target localization outside of trilateration.
- Explore optimizing the testbed to allow for a feedback loop in order to apply machine learning concepts to RTI and NRN research.
- Utilize research conducted by Nafziger [11] to apply the concept of node transmission sequence and performance tracking to both RTI and NRN to the testbed.

- Setup the testbed to allow for near real time target tracking.

Bibliography

1. Christopher Vergara, Richard K. Martin, Peter J. Collins, and James R. Lievsay. Multi-sensor data fusion between radio tomographic imaging and noise radar. *IET Radar, Sonar and Navigation*, 14(2):187–193, 2020.

2. Destinee Battle. Mitigating the Multipath Effects on Radio Tomographic Imaging. Master's thesis, Air Force Institute of Technology, 2021.

3. Richard K. Martin, Alexander Folkerts, and Tyler Heinl. Accuracy vs. resolution in radio tomography. *IEEE Transactions on Signal Processing*, 62(10):2480–2491, 2014.

4. Jiaju Tan, Qili Zhao, Xuemei Guo, Xin Zhao, and Guoli Wang. Radio Tomographic Imaging Based on Low-Rank and Sparse Decomposition. *IEEE Access*, 7:50223–50231, 2019.

5. A. R. Jiménez and F. Seco. Combining RSS-based trilateration methods with radio-tomographic imaging: Exploring the capabilities of long-range RFID systems. *2015 International Conference on Indoor Positioning and Indoor Navigation, IPIN 2015*, (October):13–16, 2015.

6. Sanaz Kianoush, Stefano Savazzi, Federico Vicentini, Vittorio Rampa, and Matteo Giussani. Device-Free RF Human Body Fall Detection and Localization in Industrial Workplaces. *IEEE Internet of Things Journal*, 4(2):351–362, 2017.

7. Joey Wilson and Neal Patwari. Radio tomographic imaging with wireless networks. *IEEE Transactions on Mobile Computing*, 9(5):621–632, 2010.

8. Christopher R. Anderson, Richard K. Martin, T. Owens Walker, and Ryan W. Thomas. Radio tomography for roadside surveillance. *arXiv*, 8(1):66–79, 2016.

9. Huseyin Yigitler, Riku Jantti, Ossi Kaltiokallio, and Neal Patwari. Detector Based Radio Tomographic Imaging. *IEEE Transactions on Mobile Computing*, 17(1):58–71, 2017.

10. Maurizio Bocca, Ossi Kaltiokallio, and Neal Patwari. Demo abstract: A radio tomographic system for real-time multiple people tracking. *IPSN 2013 - Proceedings of the 12th International Conference on Information Processing in Sensor Networks, Part of CPSWeek 2013*, pages 305–306, 2013.

11. Grant Nafziger. Wireless Sensor Network Optimization for Radio Tomographic Imaging. Master's thesis, Air Force Institute of Technology, 2020.

12. Neal Patwari and Joey Wilson. RF sensor networks for device-free localization: Measurements, models, and algorithms. *Proceedings of the IEEE*, 98(11):1961–1973, 2010.

13. Ossi Kaltiokallio, Riku Jäntti, and Neal Patwari. ARTI: An Adaptive Radio Tomographic Imaging System. *IEEE Transactions on Vehicular Technology*, 66(8):7302–7316, 2017.

14. Joey Wilson and Neal Patwari. A Fade-level skew-laplace signal strength model for device-free localization with wireless networks. *IEEE Transactions on Mobile Computing*, 11(6):947–958, 2012.

15. Chunhua Zhu and Yue Chen. Distance attenuation-based elliptical weighting-g model in radio tomography imaging. *IEEE Access*, 6:34691–34695, 2018.

16. Zhen Wang, Hang Su, Xuemei Guo, and Guoli Wang. Radio tomographic imaging with feedback-based sparse Bayesian learning. *8th International Conference on Information Science and Technology, ICIST 2018*, (61375080):50–56, 2018.

17. Yao Guo, Kaide Huang, Nanyong Jiang, Xuemei Guo, Youfu Li, and Guoli Wang. An Exponential-Rayleigh Model for RSS-Based. *IEEE Transactions on Mobile Computing*, 14(3):484–494, 2015.

18. Benjamin R. Hamilton, Xiaoli Ma, Robert J. Baxley, and Stephen M. Matechik. Propagation modeling for radio frequency tomography in wireless networks. *IEEE Journal on Selected Topics in Signal Processing*, 8(1):55–65, 2014.

19. Neal Patwari and Piyush Agrawal. NeSh: A Joint Shadowing Model for Links in a Multi-Hop Network. In *2008 IEEE International Conference on Acoustics, Speech and Signal Processing*, pages 2873–2876, 3 2008.

20. Wei Ke, Haoran Zuo, Mengling Chen, and Yanli Wang. Enhanced radio tomographic imaging method for device-free localization using a gradual-changing weight model. *Progress In Electromagnetics Research M*, 82(April):39–48, 2019.

21. Jiyong Wang and Fei Gao. Speed up imaging construction in radio tomographic imaging based on principal component analysis and compressed sensing. *Proceedings - 2019 4th International Conference on Computational Intelligence and Applications, ICCIA 2019*, pages 11–15, 2019.

22. Andrea Edelstein and Michael Rabbat. Background subtraction for online calibration of baseline RSS in RF sensing networks. *IEEE Transactions on Mobile Computing*, 12(12):2386–2398, 2013.

23. Amir Beck and Marc Teboulle. A fast iterative shrinkage-thresholding algorithm with application to wavelet-based image deblurring. In *2009 IEEE International Conference on Acoustics, Speech and Signal Processing*, pages 693–696, 2009.

24. Christopher Vergara. Multi-Sensor Data Fusion between Radio Tomographic Imaging and Noise Radar. Master's thesis, Air Force Institute of Technology, 2019.

25. Sonia Tomei, Alberto Lupidi, Daniele Stagliano, Stefano Lischi, Dario Petri, Riccardo Massini, and Marco Martorella. NORMA - A noise radar network for covert border surveillance. *Proceedings International Radar Symposium*, 2020-Octob:197–201, 2020.

26. Matthew E. Nelms. Development and Evaluation of a Multistatic Ultrawideband Random Noise Radar Network. Master's thesis, Air Force Institute of Technology, 2010.

27. Ashley L. Schmitt. Radar Imaging with A Network of Digital Noise Radar Systems. Master's thesis, Air Force Insitute of Technology, 2019.

28. Lingbao Kong, Xing Peng, Yao Chen, Ping Wang, and Min Xu. Multi-sensor measurement and data fusion technology for manufacturing process monitoring: A literature review. *International Journal of Extreme Manufacturing*, 2(2), 2020.

29. S. M. Kay. *Fundamentals of Statistical Signal Processing: Estimation Theory*. Prentice Hall, Upper Saddle River, NJ, USA, 1993.

30. David Arthur and Sergei Vassilvitskii. Worst-case and smoothed analysis of the ICP algorithm, with an application to the k-means method. *Proceedings - Annual IEEE Symposium on Foundations of Computer Science, FOCS*, pages 153–164, 2006.

31. Chen Zhang and Shixiong Xia. K-means clustering algorithm with improved initial center. *Proceedings - 2009 2nd International Workshop on Knowledge Discovery and Data Mining, WKKD 2009*, pages 790–792, 2009.

32. Jiang Dong, Dafang Zhuang, Yaohuan Huang, and Jingying Fu. Advances in multi-sensor data fusion: Algorithms and applications. *Sensors*, 9(10):7771–7784, 2009.

REPORT DOCUMENTATION PAGE

Form Approved
OMB No. 0704–0188

1. REPORT DATE *(DD–MM–YYYY)*	2. REPORT TYPE	3. DATES COVERED *(From — To)*
24–03–2022	Master's Thesis	Sept 2020 — Mar 2022

4. TITLE AND SUBTITLE

Testbed Creation to Study Noise Radar Network Weighting Models and Data Fusion with Radio Tomographic Imaging

5a. CONTRACT NUMBER

5b. GRANT NUMBER

5c. PROGRAM ELEMENT NUMBER

6. AUTHOR(S)

Ryan M. Jans, 2d Lt, USAF

5d. PROJECT NUMBER

5e. TASK NUMBER

5f. WORK UNIT NUMBER

7. PERFORMING ORGANIZATION NAME(S) AND ADDRESS(ES)

Air Force Institute of Technology
Graduate School of Engineering and Management (AFIT/EN)
2950 Hobson Way
WPAFB OH 45433-7765

8. PERFORMING ORGANIZATION REPORT NUMBER

AFIT-ENG-MS-22-M-035

9. SPONSORING / MONITORING AGENCY NAME(S) AND ADDRESS(ES)

Intentionally Left Blank

10. SPONSOR/MONITOR'S ACRONYM(S)

11. SPONSOR/MONITOR'S REPORT NUMBER(S)

12. DISTRIBUTION / AVAILABILITY STATEMENT

DISTRIBUTION STATEMENT A:
APPROVED FOR PUBLIC RELEASE; DISTRIBUTION UNLIMITED.

13. SUPPLEMENTARY NOTES

14. ABSTRACT

Significant research has been conducted on RTI weighting models; however, very little comparative research has been conducted for NRN weighting methods. In order to create comparative weighting methods for NRN, it is necessary to create a testbed which allows for RTI and NRN research to be conducted simultaneously and allow for data fusion methods to also be researched. After creating the testbed and analyzing results, the newly proposed weighting method provides an up to 33% performance increase in target localization accuracy when compared to the previous weighting model used for NRN. The attenuation image resolution improvements resulted in a 79% performance increase in target localization accuracy for the MAP estimate. In addition to the performance increase, the newly proposed weighting method has the capability to provide a foundation for future research into NRN weighting methods. The testbed created allows for seamless interchanging of data sets, weighting models, and experimental conditions.

15. SUBJECT TERMS

Radio Tomographic Imaging (RTI), Noise Radar Network (NRN)

16. SECURITY CLASSIFICATION OF:			17. LIMITATION OF ABSTRACT	18. NUMBER OF PAGES	19a. NAME OF RESPONSIBLE PERSON
a. REPORT	b. ABSTRACT	c. THIS PAGE			Dr. Richard K. Martin, AFIT/ENG
U	U	U	UU	141	19b. TELEPHONE NUMBER *(include area code)* (937) 255-3636, x4625; richard.martin@afit.edu